

# APPLIED PHYSICS REVIEWS

## Chip-scale atomic devices

John Kitching

*Time and Frequency Division, National Institute of Standards and Technology, Boulder, Colorado 80305, USA*

(Received 16 February 2018; accepted 1 May 2018; published online 14 August 2018)

Chip-scale atomic devices combine elements of precision atomic spectroscopy, silicon micromachining, and advanced diode laser technology to create compact, low-power, and manufacturable instruments with high precision and stability. Microfabricated alkali vapor cells are at the heart of most of these technologies, and the fabrication of these cells is discussed in detail. We review the design, fabrication, and performance of chip-scale atomic clocks, magnetometers, and gyroscopes and discuss many applications in which these novel instruments are being used. Finally, we present prospects for future generations of miniaturized devices, such as photonically integrated systems and manufacturable devices, which may enable embedded absolute measurement of a broad range of physical quantities. © 2018 Author(s). All article content, except where otherwise noted, is licensed under a Creative Commons Attribution (CC BY) license (<http://creativecommons.org/licenses/by/4.0/>). <https://doi.org/10.1063/1.5026238>

### TABLE OF CONTENTS

I. INTRODUCTION	1	VI. OTHER INSTRUMENTS AND TECHNOLOGIES	34
A. Atomic instrumentation: Clocks, sensors, and fundamental constants	1	A. Integration of atoms and photonics	34
B. Alkali vapor cells	3	B. Field imaging	34
C. Vapor cell atomic clocks	5	C. Other optical/atomic devices	35
D. Vapor cell atomic magnetometers	7	VII. OUTLOOK	35
E. Vapor cell NMR gyroscopes	8		
F. Laser technology	9		
II. MICROMACHINED ALKALI VAPOR CELLS	10		
A. Alkali metals	10	I. INTRODUCTION	
B. Cell fabrication	11	A. Atomic instrumentation: Clocks, sensors, and fundamental constants	
C. Introduction of alkali atoms	12	For the last half-century, atoms in the vapor phase or confined in traps, where they interact only weakly with their environment, have been a valuable tool for precision measurement. Since measurements on these systems have been so successful, in 1967, the second was redefined in terms of atomic energy level structure to be the duration of 9 192 631 770 periods of the radiation corresponding to the transition between the two hyperfine-split levels of the ground state of the cesium atom. Time remains the most accurately measured physical quantity and frequency measurements usually result in the best measurements of other physical quantities. For example, when the speed of light was defined to be a fixed quantity in 1983, the realization of the meter became fundamentally a measurement of the frequency of optical radiation with respect to the SI second.	
D. Alternative cell geometries	16	There are several fundamental reasons why isolated atomic systems are so useful in metrology. The first is that isolated atoms are simple, well-defined quantum systems. Every isolated atom of cesium or rubidium has identical dynamics that depend only on fundamental (and presumably invariant) constants of nature, a proposition articulated <sup>1</sup> by Sir William Thomson (later Lord Kelvin) in 1879. For	
E. Alternatives to anodic bonding	17		
III. MEMS-BASED ATOMIC CLOCKS	18		
A. Introduction	18		
B. Design considerations	19		
C. Physics packages	20		
D. Compact, low-power local oscillators	22		
E. Control electronics	23		
F. CSAC prototypes	25		
G. Performance and impact	26		
H. Applications	28		
IV. CHIP-SCALE ATOMIC MAGNETOMETERS	29		
A. Device design, fabrication, and performance	29		
B. Chip-scale nuclear magnetic resonance	31		
C. Biomagnetics with chip-scale atomic magnetometers	31		
D. Chip-scale atomic magnetometers for space	32		
V. CHIP-SCALE ATOMIC GYROSCOPES	33		
A. Nuclear magnetic resonance gyroscopes	33		
B. Device design, fabrication, and performance	33		

example, the hyperfine Hamiltonian for the hydrogen atom is given by

$$H = \frac{4m_e c^2 \alpha^2 g_I}{3n^3} \left(1 + \frac{m_e}{m_p}\right)^{-3} \vec{I} \cdot \vec{J}, \quad (1)$$

where  $\vec{I}$  and  $\vec{J}$  are the (quantum mechanical) angular momentum operators associated with the nucleus and electron, respectively;  $m_e$  and  $m_p$  are the rest mass of the electron and proton, respectively;  $c$  is the speed of light;  $\alpha$  is the fine structure constant;  $g_I$  is the Lande g-factor of the proton; and  $n$  is the energy quantum number. Under the assumption that the atomic constants in Eq. (1) are not changing (and no variation has ever been observed), the energy level structure of the hydrogen atom is also invariant in space and time and is the same for every hydrogen atom. Transitions between other energy levels in atoms (for example, Zeeman transitions or optical transitions) have similar properties. It is such considerations that have led to instruments based on atomic transitions being referred to as “quantum technologies.”

Alkali atoms, with a single valence electron, are used in almost all microwave atomic clocks for the following reasons. First, they have a high vapor pressure at a given temperature resulting in large spectroscopic signals. Second, the non-zero nuclear spin leads to a ground state hyperfine splitting in the GHz range, which is a convenient frequency band for standard RF electronics. Third, the simple electronic structure allows for efficient optical pumping and the optical absorption cross sections are large enough for efficient detection of the atomic state through interaction with an optical field.

The energy spectrum of the  $^{87}\text{Rb}$  atom is shown in Fig. 1. The  $S_{1/2}$  ground state is coupled to the two lowest energy excited states,  $P_{1/2}$  and  $P_{3/2}$ , by optical fields at 795 and 780 nm, respectively. These transitions, usually excited by a lamp or a laser, allow efficient energy or spin optical pumping<sup>2,3</sup> by appropriately tuned and polarized optical fields. They also provide a convenient, SI-traceable reference for optical frequency and, ultimately, wavelength. Each of these states has hyperfine structure with the energy splitting in the MHz-GHz range. It is the ground state hyperfine splitting (6.8 GHz for  $^{87}\text{Rb}$ ) that is used in most microwave atomic clocks. Finally, each hyperfine level is split again in the presence of a magnetic field. This Zeeman splitting or Larmor frequency, which is on the order of 10 GHz/T, is used in atomic magnetometers.

Because any interaction with the environment causes environment-dependent deviations from this fundamental dynamics, much of the work in the area of atomic clocks, for example, is focused on this one goal: isolating atoms from their environment. Under this condition, the dynamics of atomic systems can have very long relaxation times and corresponding high quality factors (Q). Optical coherences in trapped ions, for example, have reached Q's well above  $10^{15}$ . This remarkable property of atomic systems has resulted in optical atomic clocks that now reach frequency uncertainties in the low  $10^{-18}$  range.<sup>5</sup> In the microwave domain, hyperfine coherences in alkali atoms can have relaxation times near 100 ms in alkali cells containing buffer

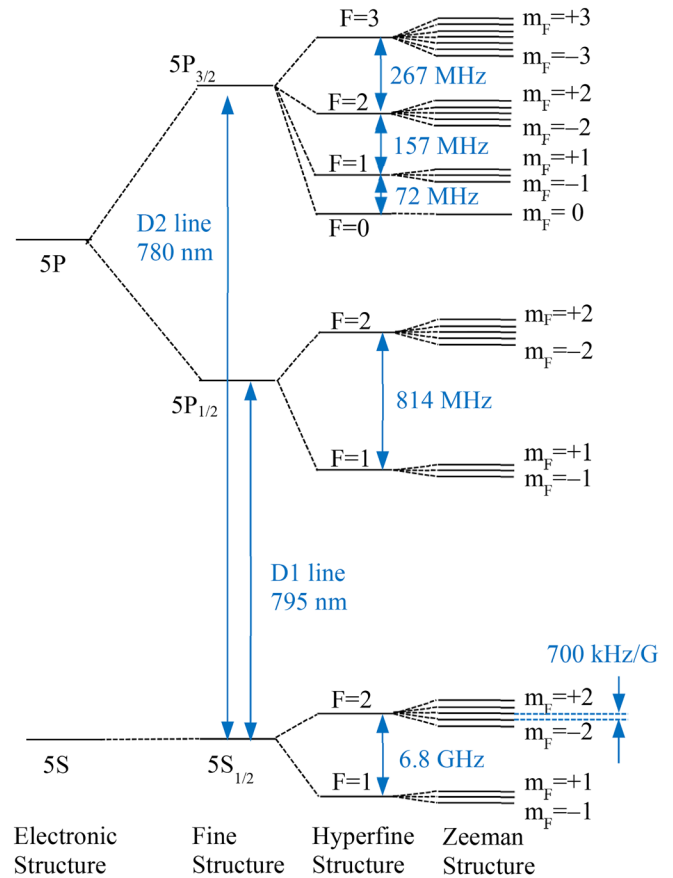


FIG. 1. Energy level spectrum of  $^{87}\text{Rb}$ .

gases<sup>6,7</sup> and near 1 s in atomic fountains based on laser-cooled atoms.<sup>8,9</sup> Spin coherence times in atoms confined in buffer gases are typically near 1 s for cells on the size scale of 10 cm, and even longer spin coherence times have been reported in wall-coated cells.<sup>10</sup> Finally, nuclear spin coherence times of atoms in the vapor phase can be as high as several days.<sup>11,12</sup>

The commercial atomic clock market today is dominated by two clock designs: vapor cell atomic clocks, discussed in detail below and usually based on Rb, and beam clocks based on Cs. Vapor cell clocks rely on an atomic vapor coexisting with a solid or liquid phase, all confined in a cell. They are smaller and less expensive than beam clocks and are typically used where timing over hours to days is important. The largest application space for vapor cell clocks at present is base stations for cellular telephone systems. Beam clocks, based on a collimated beam of atoms moving at thermal velocities along a single axis, are larger and more expensive and tend to be used in applications where accuracy or stability over periods longer than one month are important. Beam clocks are used as master clocks for high-speed telecommunications systems and for basic time and frequency metrology.

More advanced atomic clocks are under development in laboratories around the world, but significant use as commercial products is not yet found. Fountain clocks use laser-cooled atoms to lengthen the time in which the atoms can oscillate without perturbation and currently serve as the best realizations of the SI second<sup>13,14</sup> at a level of about  $10^{-16}$ .

Optical clocks<sup>5</sup> are based on laser-interrogation of optical transitions in atoms. They have emerged over the last two decades as the highest-performing timing instruments due to the development of optical frequency combs, which can efficiently divide the high optical frequency down to the microwave domain where the signal can be counted and used for timing. Currently, clocks based on single trapped ions and those based on neutral atoms trapped in an optical lattice both achieve frequency uncertainties below  $10^{-17}$ .

Chip-scale atomic clocks (CSACs) grew out of a convergence of atomic spectroscopy, silicon micromachining, and semiconductor laser technology in the early 2000s. These atomic clocks combine small size and low power with moderate frequency stability in the 1 h to 1 week time frame. A significant research effort was undertaken in the United States by multiple teams throughout the 2000s, culminating in the release of a commercial product in 2011. The work on chip-scale atomic clocks and related instruments continues to this day at a rapid pace, with active programs in countries throughout the world including France, Switzerland, Germany, The United Kingdom, Japan, and China.

In this section, we introduce the basic physics and instrumentation concepts that underlie chip-scale atomic devices. In most cases, this physics is several decades old and is reviewed here to enable a clearer understanding of subsequent sections of the paper. In Sec. II the fabrication of micromachined alkali vapor cells, first developed in the early 2000s, is discussed. The use of these microfabricated cells in clocks, magnetometers, and gyros is discussed in Secs. III–V, and the emerging applications in which these unique instruments are being used are identified in Sec. VI. Section VII concludes with a discussion of more recent, forward-looking work that may hint at what the future holds for chip-scale atomic devices.

## B. Alkali vapor cells

Evacuated glass cells containing alkali atoms have been used in atomic spectroscopy as far back as the 1950s. The cells are typically made using glassblowing techniques, in which a sealed glass container is fitted with a filling tube through which the cell is evacuated before a small quantity of solid or liquid alkali metal is distilled into the cell body. The filling tube is then sealed by heating. Without any additional gas added to the cell, the alkali atoms undergo ballistic transport across the vapor cell, at velocities of a few hundred m/s and with a typical transit time on the order of  $1 \mu\text{s}$  for a cell of 1 cm in size. Since collisions with untreated glass cell walls completely depolarize the spin of the atoms, the Fourier limited “transit time” width of any atomic coherence is near 1 MHz and the resulting quality factor for a hyperfine resonance is about  $10^4$ . Doppler broadening of the transition is also present and limits the Q to about  $10^6$ .

The addition of inert “buffer” gases to the cell can substantially narrow the transition linewidths. Gases such as Ne, N<sub>2</sub>, Ar, and He interact only very weakly with the spin of the alkali atoms and hence the atoms can undergo many collisions (typically hundreds of thousands) with the buffer gas before the spin depolarizes. The result is that for typical

buffer gas pressures of  $\sim 10$  Torr, the mean free path of the alkali atoms is on the order of  $1 \mu\text{m}$  and the atoms undergo diffusive motion through the cell rather than ballistic motion. The time between depolarizing wall collisions is therefore considerably longer, typically  $\sim 10$  ms for a 1 cm cell with 10 Torr of buffer gas. In addition, the short mean-free-path leads to “Dicke narrowing,”<sup>15</sup> in which Doppler broadening from the atoms’ thermal motion is suppressed.

The buffer gas is not completely benign, however. Some small relaxation of the hyperfine or Zeeman transitions does occur due to collisions and for hyperfine transitions, the transition line is significantly shifted<sup>16</sup> and broadened. Typically, the buffer gas pressure is adjusted to balance relaxation from the walls, which is inversely proportional to the buffer gas pressure  $P$ , and relaxation from buffer gas collisions, which is proportional to  $P$ . The relaxation rate for a diffusion mode  $\nu$  is then given by<sup>3</sup>

$$\Gamma_\nu = \gamma_0 \left( \frac{P}{760 \text{ Torr}} \right) + \frac{D_0}{\Lambda_\nu^2} \left( \frac{760 \text{ Torr}}{P} \right), \quad (2)$$

where  $\gamma_0$  and  $D_0$  are the relaxation rate and diffusion constant of the alkali atoms at 760 Torr, and  $\Lambda_\nu$  is the diffusion length for the mode  $\nu$ . Usually only the lowest-order diffusion mode is considered (the others decay more rapidly), for which  $\Lambda_0 \approx L$ , where  $L$  is the length of the cell. For example, for a cylindrical cell of radius  $a$  and length  $L$ , the diffusion length of the lowest-order mode is given by<sup>17</sup>

$$\frac{1}{\Lambda_0^2} = \left[ \frac{(2.405)^2}{a^2} + \frac{\pi^2}{L^2} \right]. \quad (3)$$

The coefficients  $\gamma_0$  and  $D_0$  have been measured for many combinations of buffer gases and alkali atoms and are tabulated in various places.<sup>3,17</sup> From Eq. (2), the relaxation rate of the lowest-order diffusion mode as a function of buffer gas pressure exhibits a broad minimum near a pressure of

$$P_{opt} = \sqrt{\frac{D_0}{\gamma_0}} \frac{1}{\Lambda_0} (760 \text{ Torr}), \quad (4)$$

for which the relaxation rate is  $\Gamma_0 = 2 \frac{\sqrt{\gamma_0 D_0}}{\Lambda_0}$  and the broadening of the transition linewidth is therefore

$$\Delta\nu_{bg} = \frac{2}{\pi} \frac{\sqrt{\gamma_0 D_0}}{\Lambda_0}. \quad (5)$$

Spin-exchange collisions between alkali atoms can also cause broadening proportional to the alkali atom density. For Rb, for example, spin-exchange collisions result in a broadening of the hyperfine transition linewidth of about 700 Hz at a cell temperature of  $85^\circ\text{C}$ . Spin exchange broadening becomes increasingly important for small cell sizes where higher alkali densities are needed to give optimal signals. Spin-exchange relaxation is also important for atomic magnetometers, which typically operate at higher cell temperatures than atomic clocks.

For optimal buffer gas pressure, the relaxation rate is therefore inversely proportional to the cell size. Typical

relaxation rates (and optimal buffer gas pressures) for hyperfine transitions are a few hundred  $s^{-1}$  (a few tens of Torr) for cm-scale cells and a few thousand  $s^{-1}$  (a few hundreds of Torr) for mm-scale cells. Since the collisions between alkali atoms and the buffer gas are electronic in nature, the presence of the buffer gas results in significant homogeneous broadening of the optical transitions, typically by  $\sim 20$  MHz/Torr.<sup>17</sup> At 500 Torr, this broadening is  $\sim 10$  GHz, implying that both the ground state and excited state hyperfine structures are unresolved. This imposes some limitations on the types of spectroscopy that can be carried out. For example, optically excited higher-order coherences usually require resolved excited state hyperfine structure.

Molecular nitrogen has a unique role in vapor cells because of its very large excited state quenching cross-section for alkali atoms. In the presence of  $N_2$ , alkali atoms decay non-radiatively from their excited states via transfer of energy to ro-vibrational modes of the molecule, and the issues related to radiation trapping can be avoided.

Collisions of the alkali atoms with the buffer gas also result in a net shift of the hyperfine frequency. During such a collision, the alkali atoms spend a short time in the potential of a buffer gas atom, during which the energy levels of the alkali atom are shifted from their unperturbed values. Averaged over many collisions, this results in a net shift that depends on the buffer gas density and the cell temperature.<sup>16,18</sup> This shift can be written (to second order in temperature) as<sup>17</sup>

$$\nu_{bg} = P_0 \left( \beta_0 + \gamma_0(T - T_0) + \delta_0(T - T_0)^2 \right), \quad (6)$$

where  $P_0$  is the buffer gas pressure;  $T$  is the cell temperature; and  $\beta_0$ ,  $\gamma_0$ ,  $\delta_0$ , and  $T_0$  are phenomenological constants specific to a given buffer gas and alkali atom species.<sup>19</sup> The values of  $\beta_0$  and  $\gamma_0$  depend on the alkali species and buffer gas but are (fractionally) on the order of<sup>17</sup>  $10^{-7}$ /Torr and  $10^{-11}$ /Torr/K, respectively, which can lead to significant clock instabilities if the temperature of the vapor cell fluctuates. Lighter buffer gases result in temperature coefficients  $\gamma_0$  of opposite sign from those of heavier buffer gases. It is therefore possible to use combinations of buffer gases to bring the first-order dependence of the buffer gas shift to zero at some specific temperature, resulting in a residual second-order shift.<sup>6</sup> When the vapor cell is stabilized at this temperature, the sensitivity of the hyperfine frequency to temperature variations is reduced dramatically and the stability of a clock is improved correspondingly.

An alternative approach to reduce the effects of wall collisions is to apply a coating such as paraffin on the interior walls of the vapor cell.<sup>20,21</sup> While similar (and sometimes even narrower) linewidths can be obtained, wall coatings have not generally been adopted for vapor cell atomic clocks, in part due to the instability of the coating materials at elevated temperatures. However, wall coatings offer some significant advantages for chip-scale atomic clocks and magnetometers, since the excited state hyperfine structure can be well resolved while still achieving narrow Zeeman and hyperfine transitions.

When an alkali atom collides with, for example, a paraffin-coated wall, the energies of the hyperfine-split ground states of

the atom are shifted relative to each other by the Van der Waals interaction. This energy splitting, averaged over the time the atom spends on the wall (the adsorption time), results in a phase shift,  $\phi$ , of the atom's hyperfine coherence. Under the assumption that  $\phi \ll 1$ , the cumulative effect of many such collisions is an overall shift in the hyperfine frequency by

$$\nu_w = \frac{\bar{\phi}}{2\pi t_c}, \quad (7)$$

where  $\bar{\phi}$  is the average phase shift per collision and  $t_c$  is the average time between collisions. The parameter  $\bar{\phi}$ , therefore, represents a property of the coating, which is independent of size and shape of the vapor cell, and is the primary way in which a particular wall coating is characterized.

Wall collisions also result in line broadening, primarily because of the dispersion in adsorption time, which causes a dispersion in  $\phi$ . Under some conditions,<sup>21</sup> it can be shown that after  $N$  collisions, the dispersion in the accumulated phase shift is  $\delta\phi(t) = \sqrt{N} \bar{\phi} = \sqrt{\frac{t}{t_c}} \bar{\phi}$ , and the resonance width is<sup>22</sup>

$$\Delta\nu_w = \frac{\bar{\phi}^2}{\pi t_c}. \quad (8)$$

For example, the average phase shift for the hyperfine transition of  $^{87}\text{Rb}$  on Paraffint<sup>TM</sup> is<sup>23</sup>  $\sim 0.08$  rad, from which the wall shift and relaxation linewidth can be calculated from the above equations.

The interaction of an atom with a wall coating can also be characterized by the average number of wall bounces,  $N_b$ , which an alkali atom can undergo before it relaxes. This is given by the condition<sup>21</sup>

$$\frac{1}{2} N_b \bar{\phi}^2 = 1, \quad (9)$$

which leads to an alternate formulation of the linewidth as

$$\Delta\nu_w = \frac{2}{\pi N_b t_c}. \quad (10)$$

The linewidths for a cell with diameter equal to length are shown as a function of buffer gas pressure and cell diameter in Fig. 2. As a function of buffer gas pressure, the linewidth exhibits a broad minimum at the pressure for which the relaxation due to wall collisions is equal to the relaxation due to buffer gas collisions, as shown in Fig. 2(a). An optimal buffer gas pressure and corresponding linewidth exist for each cell diameter, as predicted by Eqs. (4) and (5). For a wall-coated cell, the linewidth decreases inversely with the cell diameter, as indicated by Eq. (7). For buffer gas cells at a fixed buffer gas pressure, the linewidth is a constant at large cell diameter, where the linewidth is dominated by buffer gas collisions, and increases at smaller cell sizes where the effects of wall relaxation dominate, as shown in Fig. 2(b). The ‘‘knee’’ in these curves represents the optimal linewidth and corresponding minimum cell diameter for the given buffer gas pressure. These optimal linewidths decrease inversely with the cell diameter as indicated by Eq. (5).

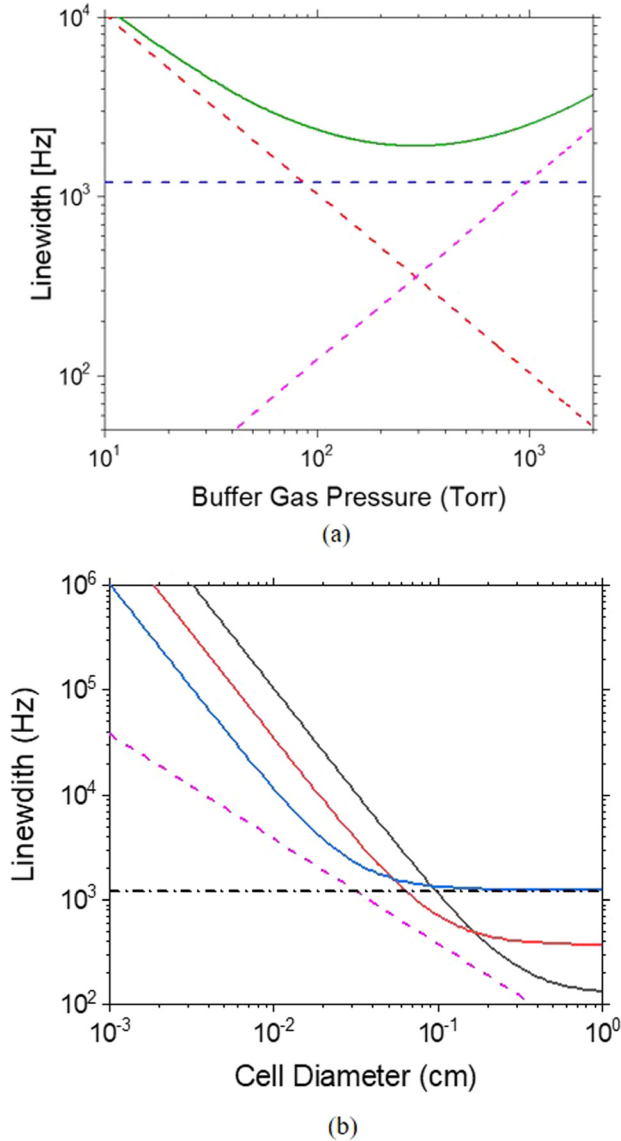


FIG. 2. (a) Hyperfine linewidth for a cylindrical cell with its diameter equal to its length,  $L$ , as a function of buffer gas pressure for  $^{85}\text{Rb}$  in  $\text{N}_2$  at  $85^\circ\text{C}$  and  $L = 1$  mm. The dashed lines show the contributions due to wall relaxation (red), Rb-Rb spin-exchange collisions (blue), and Rb-buffer gas collisions (magenta). The green solid line shows the total linewidth, with a broad minimum near 300 Torr as a function of cell diameter. (b) Hyperfine linewidth as a function of cell diameter. The solid lines assume a  $\text{N}_2$  buffer gas pressure of 100 Torr (black), 300 Torr (red), and 1000 Torr (blue). The magenta dashed line indicates the linewidth of a cell with no buffer gas and a wall coating with  $N_B = 1000$ . The black dotted-dashed line indicates the spin-exchange relaxation linewidth at  $T = 85^\circ\text{C}$ . Note: calculated linewidths are approximate as relaxation cross-sections are not known exactly.

The light used for optically pumping and probing the atoms also results in a shift of the atomic energy levels. For a near-resonant optical field interacting with a two-level atom, the scalar AC Stark shift is

$$\nu_{LS} = \frac{1}{4} \frac{\Omega^2 \Delta}{\Delta^2 + (\Gamma/2\pi)^2}, \quad (11)$$

where  $\Omega$  is the Rabi frequency,  $\Delta$  is the detuning from optical resonance, and  $\Gamma$  is the relaxation rate of the excited state. Since the intensity  $I \sim \Omega^2$ , this shift is proportional to

the intensity of the interrogating light. For a two-level system, this light shift is zero when the optical field is exactly on resonance with the atomic transitions. In real atoms, however, the optical field interacts with transitions to many other atomic energy levels, resulting in an overall light shift even in perfect resonance with a single transition.

For polarized atoms interacting with a polarized optical field, a second-order AC Stark effect can shift the Zeeman-split levels. For circularly polarized light and a homogeneously broadened transition, this shift can be viewed as a fictitious magnetic field proportional to the light intensity and directed along the  $\mathbf{k}$ -vector of the optical field<sup>24,25</sup>

$$B_{LS} = -\frac{r_e c f \Phi}{\gamma} \frac{\Delta}{\Delta^2 + (\Gamma/2\pi)^2}, \quad (12)$$

where  $r_e$  is the classical electron radius,  $c$  is the speed of light,  $f$  is the transition strength,  $\Phi$  is the photon flux, and  $\gamma$  is the gyromagnetic ratio of the electron.

Microwave atomic clocks typically use the first-order magnetically insensitive transition between the  $m_F = 0$  levels of the hyperfine ground states. This transition has a second-order magnetic field shift

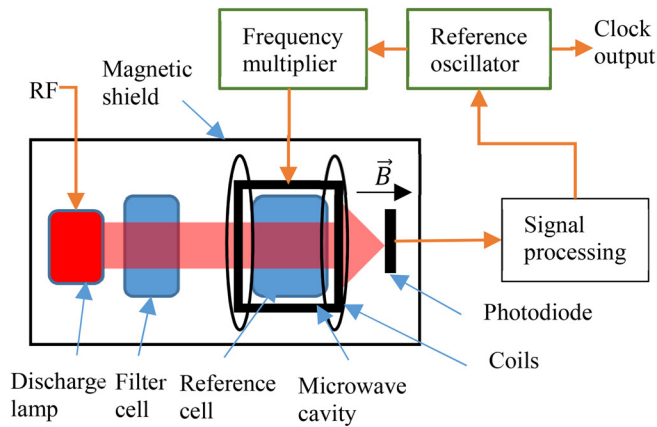
$$\nu_{Z,2} = \frac{[(g_J + g_I) \mu_B / \hbar]^2}{\nu_{\text{hfs}}} B_0^2, \quad (13)$$

which can be important for very high performance or accurate atomic clocks.

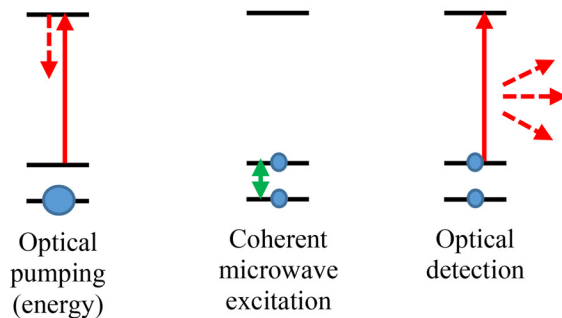
### C. Vapor cell atomic clocks

Vapor cell atomic clocks<sup>6,26–28</sup> are based on the excitation of hyperfine transitions in alkali atoms (usually  $^{87}\text{Rb}$ ) confined in a vapor cell; a typical configuration is shown in Fig. 3. In this implementation, an RF  $^{87}\text{Rb}$  discharge lamp produces pump light resonant with optical transitions in  $^{87}\text{Rb}$ .  $^{85}\text{Rb}$  has an absorption resonance nearly overlapping one, but not both, of the spectral lines emitted by the lamp; a cell containing  $^{85}\text{Rb}$  positioned between the lamp and the reference cell filters the light and creates an intensity imbalance between the spectral lines emitted by the lamp. This imbalanced spectrum optically pumps  $^{87}\text{Rb}$  atoms in the reference cell into the  $F = 2$  hyperfine ground state, which results in an increased transmission of the pump light through the cell.

The reference cell, also containing a suitable buffer gas to reduce the hyperfine transition linewidth, is situated inside a microwave cavity tuned to the hyperfine resonance frequency. Microwaves applied to the cavity induce transitions between the hyperfine states in the  $^{87}\text{Rb}$  atoms only when the microwave frequency corresponds to the atomic hyperfine transition frequency. Under this resonance condition, the population difference between the two hyperfine states is driven toward zero and the pump absorption increases toward its equilibrium value. By monitoring the transmitted pump power on a photodiode, the reference oscillator that serves as the microwave source can be locked electronically onto the atomic transition and stabilized. The entire device is placed inside a magnetic shield to prevent magnetic-field



(a)



(b)

FIG. 3. (a) Vapor cell atomic clock. (b) The clock operation can be thought of as occurring in three steps: optical pumping to prepare the atomic state; coherent, resonant microwave excitation; and optical detection of the final state. Feedback of the detected signal to the drive oscillator stabilizes its frequency to the atomic transition. In practice, all steps occur simultaneously.

induced changes in the atomic energy spectrum and hence the frequency of the clock.

With the advent of semiconductor lasers able to be tuned to the relevant transitions in alkali atoms, new approaches to vapor cell atomic clocks have been possible. In one such approach, optically induced hyperfine coherences based on the phenomenon of coherent population trapping (CPT)<sup>29,30</sup> are used, as shown in Fig. 4. Instead of applying the microwave field directly to the atoms, the injection current of a diode laser is instead modulated, which creates sidebands on the optical carrier spaced by the hyperfine frequency (or a sub-harmonic). When the modulation frequency is equal to the ground state hyperfine splitting, the resulting optical spectrum optically pumps the atoms into a coherent dark state: a superposition state of the two hyperfine ground states that does not absorb the pump light. The power transmitted through the reference cell therefore increases, leading to a detectable CPT resonance, which is used to stabilize the reference oscillator as above. In a longitudinal magnetic field, linearly polarized light does not excite CPT resonances between magnetically insensitive levels for symmetry reasons, and a quarter-wave plate is needed in the beam path to convert the light from the linearly polarized output of the laser to circular polarization.

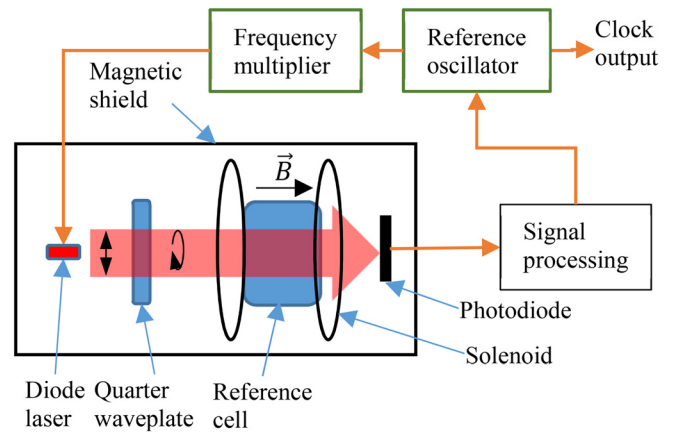


FIG. 4. Vapor cell atomic clock based on coherent population trapping. A modulated laser excites hyperfine coherences without any direct application of microwaves to the atomic ensemble.

CPT excitation has the advantage over conventional microwave excitation that a microwave cavity is not required around the atoms. This leads to a reduced experimental complexity and the possibility of smaller size, since the conventional microwave cavities used in most vapor cell atomic clocks must be larger than one-half the wavelength of the microwave radiation (2.2 cm for  $^{87}\text{Rb}$ ) to be resonant. Coherent population trapping was investigated<sup>31–35</sup> in the context of atomic beam clocks throughout the 1980s. More recently, CPT has been used in vapor cell clocks,<sup>36,37</sup> including CPT masers.<sup>38–41</sup> Most chip-scale atomic clocks rely on coherent population trapping, although new miniature microwave cavities<sup>42</sup> remain a viable alternative for miniaturized atomic clocks. A review of the application of CPT to atomic clocks can be found in Ref. 43.

The use of a laser also relaxes the need to use Rb as the reference atom. Traditionally, Cs has not been used in vapor cell atomic clocks because there is no good way of spectrally filtering the light generated by the lamp to achieve hyperfine optical pumping. Because a single-mode laser lases at one wavelength only, hyperfine optical pumping can also be achieved in Cs (or even K).

A modulation of the current of a diode laser produces a combination of AM and FM modulation on the optical field because of the linewidth enhancement factor<sup>44</sup> present in the semiconductor gain media. When the buffer gas pressure in the cell is small enough that optical transitions from the hyperfine ground states to the excited state are well resolved, both AM and FM modulation produce the same CPT signal. For higher buffer-gas pressures, however, when the transitions overlap, it has been demonstrated<sup>45</sup> that AM modulation produces a strong CPT signal, while the destructive interference that occurs for FM modulation results in a strongly suppressed CPT signal.

Discharge lamps typically operate on 1 W of power or more, and the use of a laser can considerably reduce the power needed to produce the light. As discussed below, vertical-cavity surface emitting lasers are a suitable light source for CPT atomic clocks and can operate on only a few mW of power. Microfabricated<sup>46,47</sup> discharge lamps with potentially lower power than their larger counterparts are

currently under development and may provide an alternative to low-power lasers for future chip-scale atomic devices.

Current commercial compact vapor cell atomic clocks have volumes of about 0.1 l, consume about 10 W of electrical power, and achieve short-term fractional frequency stabilities of around  $10^{-11}$  at 1 s of integration. The long-term drift is about  $10^{-11}$ /month. The main commercial application for this type of clock is in synchronization of telecommunications systems such as cell phone networks.<sup>48</sup> Research instruments being developed for next-generation satellite navigation systems achieve about two orders of magnitude better short- and long-term stability in the laboratory.<sup>49</sup>

#### D. Vapor cell atomic magnetometers

Atomic (or optical) magnetometers<sup>50</sup> have an overall design, shown in Fig. 5, very similar to that of a vapor cell atomic clock. Once again, there is a discharge lamp (or laser) as the light source and a reference cell containing the alkali atoms. Magnetometers, however, rely on the Zeeman splitting of the atomic energy levels rather than the hyperfine splitting (see Fig. 1). The optical pumping is with respect to the spin degree of freedom rather than the energy degree of freedom. The pump light must therefore be polarized, but does not need to be spectrally filtered. In a spin precession magnetometer, a precession of the atomic spins about the ambient magnetic field can be driven by a pair of Helmholtz coils and defines a Larmor frequency from which the field can be determined. Once again, a photodiode detects the response of the atomic system to the applied RF field, and

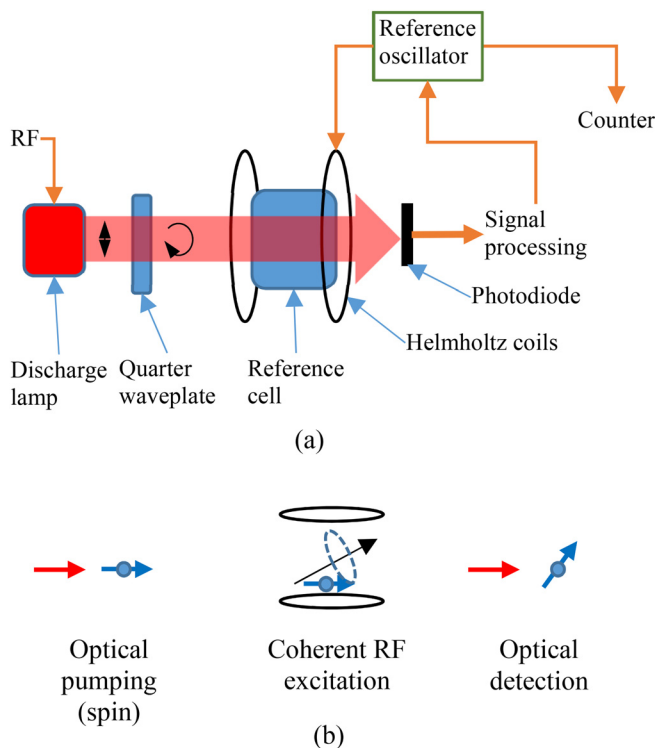


FIG. 5. (a) Atomic (or optical) magnetometer. (b) A circularly polarized light beam spin-polarizes the atomic ensemble; RF coils drive a precession of the spins about the ambient magnetic field; final orientation of spins is detected optically. Measurement of the resulting Larmor frequency is used to determine the ambient magnetic field.

the resulting signal is used to stabilize the drive oscillator onto the Larmor frequency.

Both the AC (Mx mode) and DC (Mz mode) signals from the photodiode can be used.<sup>51</sup> In the Mx mode, the phase of the photodiode signal at the drive frequency is compared with the phase of the drive frequency itself, and a dispersive error signal is generated as this frequency is scanned across the magnetic resonance line. In the Mz mode, the DC photodiode signal is used to measure the magnitude of the projection of the spin precession onto the magnetic field axis. This signal is symmetrical about the magnetic resonance and is converted to a dispersive signal using a modulation of the drive frequency and lock-in detection. The Mx mode has better sensitivity and bandwidth, while the Mz mode is less sensitive to the sensor's orientation in the magnetic field (has lower heading error). Since the spin precession frequency depends only on the magnitude of the ambient magnetic field, these sensors are referred to as scalar sensors and are useful on moving platforms since the changing projection of the ambient magnetic field onto the sensor axis does not change the sensor reading.

At very low magnetic fields (such that the Larmor frequency is much smaller than the relaxation rate of the atoms), an alternative “zero-field” approach<sup>52</sup> can be used. Here, there is no drive field at the Larmor frequency, and instead the presence of a weak magnetic field perpendicular to the atomic polarization induces a quasi-static reorientation of the atomic spin polarization. This reorientation results in increased optical absorption, and hence a zero-field resonance in the transmission spectrum of the light as a function of magnetic field. By applying a low-frequency transverse field and using lock-in detection, this absorptive resonance can be turned into a dispersive resonance with a maximal slope at zero field suitable for detection. Zero field magnetometers operated at high atomic densities (i.e., high cell temperatures) exhibit a remarkable suppression of spin-exchange collisions<sup>53,54</sup> that can lead to strong, narrow zero field resonances. Such resonances have been used in spin-exchange relaxation-free (SERF) magnetometry to achieve exceptionally high field sensitivities, below  $1 \text{ fT}/\sqrt{\text{Hz}}$ .<sup>55,56</sup> It was recognized early on<sup>53</sup> that SERF magnetometry would be particularly important for highly miniaturized sensors where high alkali atom densities are required to offset the shorter optical path length.

Light narrowing<sup>57</sup> can also be used to reduce broadening due to spin-exchange collisions and improve the sensitivity of atomic magnetometers. Light narrowing is the use of strong optical fields to optically pump most of the atoms into the same high-angular momentum state resulting in reduced angular momentum transfer between colliding atoms. This line-narrowing method is not as effective as the full suppression of spin-exchange broadening achieved at high alkali densities and low magnetic fields, but has the advantage that it can operate in high fields.

Current commercial atomic magnetometers have volumes of about 1 l, consume about 10 W of power while operating, and achieve a field sensitivity of 1 pT at 1 s of integration time. The main applications are oil and mineral

exploration, the detection of unexploded ordinance, and magnetic anomaly detection.

### E. Vapor cell NMR gyroscopes

Vapor cell nuclear magnetic resonance (NMR) gyroscopes<sup>58–60</sup> are also based on the precession of atomic spins in a magnetic field. If such a field is kept very stable, a rotation of the apparatus about the field axis results in change in phase of the atomic spins with respect to the apparatus coordinate system. This phase shift can be measured and the rotation rate can be deduced from the apparent shift of the spin precession frequency. Although electron spins in alkali atoms can, in principle, be used, nuclear spins in noble gases have considerably longer spin relaxation times, are less sensitive to magnetic fields, and result in better gyro performance. The basic design of an NMR gyro is shown in Fig. 6. As in an atomic magnetometer, alkali spins in a vapor cell are optically pumped with a circularly polarized pump beam. A noble gas with non-zero nuclear spin is confined inside the cell with the alkali atoms and becomes polarized itself through spin-exchange collisions with the alkali atoms.<sup>61</sup>

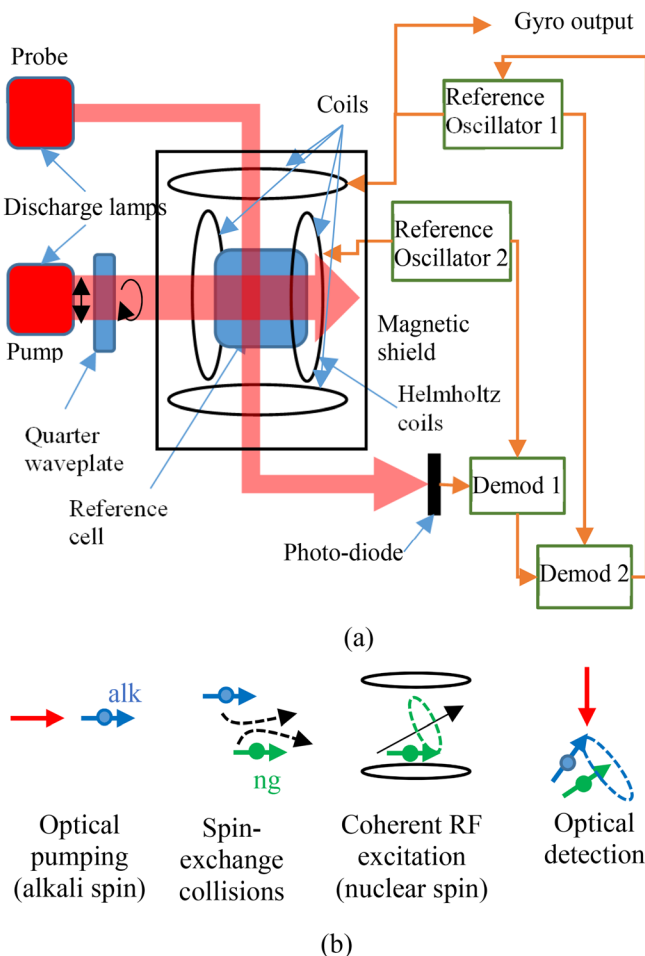


FIG. 6. (a) NMR gyroscope based on spin-exchange optical pumping of noble gas nuclei with a polarized alkali vapor. (b) Alkali atoms are polarized with a circularly polarized optical field; alkali atoms collide with noble gas atoms and transfer spin to noble gas nuclei; noble gas atoms precess in magnetic field; orientation of noble gas is determined using alkali atoms as an *in-situ* magnetometer.

A transverse coil creates an oscillating magnetic field at the approximate Larmor frequency of the noble gas which drives a precession of the nuclear spins about a static applied magnetic field. These precessing spins have a magnetization, which adds transversely to the static magnetic field seen by the alkali atoms. The alkali atoms therefore see a magnetic field precessing at the nuclear Larmor frequency on a cone whose axis is defined by the original static field. A pair of longitudinally oriented coils drives a precession of the alkali spins about the precession total field at  $\sim 100\times$  higher frequency. The phase of this alkali precession is detected with a transverse probe field tuned to the optical resonance in the alkali atoms.

The resulting signal has a double modulation, with signal at the high-frequency alkali Larmor frequency amplitude modulated by the lower-frequency noble gas Larmor frequency. Using two-stage demodulation, the noble gas precession frequency can be determined with high signal-to-noise ratio. Changes in this  $\sim 100$  Hz frequency can be detected with  $\sim$  nHz resolution, leading to a gyro bias drift below  $0.01^\circ/\text{h}$ .<sup>59,62,63</sup> Several reviews of NMR gyroscopes have been published previously.<sup>63–67</sup>

A key ingredient to the successful implementation of an NMR gyro design is the comagnetometer. Because magnetic fields shift the spin resonance frequency of a single atomic species in a manner similar to rotations, fluctuations in magnetic field cause corresponding fluctuations in the apparent rotation rate. It is possible to circumvent this difficulty using a comagnetometer, in which two spin-polarized atomic species with different gyromagnetic ratios are confined in the same volume. In one implementation, two noble gas species are used and ratios of the precession frequencies determine the rotation rate in a field-independent manner ( $^{129}\text{Xe}/^{131}\text{Xe}$ ,  $^{199}\text{Hg}/^{201}\text{Hg}$ ,  $^{83}\text{Kr}/^{129}\text{Xe}$ , and  $^3\text{He}/^{129}\text{Xe}$ ).<sup>60,68,69</sup> One species in effect measures the magnetic field, and this signal can be used to correct the field-induced shifts of the second species.

A second type of comagnetometer<sup>70</sup> is based on a single noble gas species monitored with an *in-situ* atomic magnetometer, but in a configuration where the fields seen by both atomic species are quite low, leading to a resonant interaction between the two atomic species near DC. As shown in Fig. 7, a circularly polarized pump laser optically pumps an alkali species in a longitudinal magnetic field,  $B_c$ . The noble gas species is polarized by spin-exchange collisions, just as in a traditional spin-precession NMR gyro. Because both species of atoms are polarized, each produces a magnetic field seen by the other species. If the longitudinal magnetic field,  $B_c$ , is set such that it largely cancels the magnetic field,  $B$ , of the noble gas seen by the alkali atoms, the precession frequency of the alkali species can be reduced to near zero and roughly equal to the precession frequency of the noble gas. In this regime, the spin-exchange interaction produces a coupling between the noble gas and alkali atoms. Under rotation, the nuclear and alkali spins become misaligned resulting in a quasi-static rotation of the alkali spins into the inertial rotation axis. This spin rotation angle is proportional to the inertial rotation rate and can be detected using a probe light field propagating along the rotation axis.

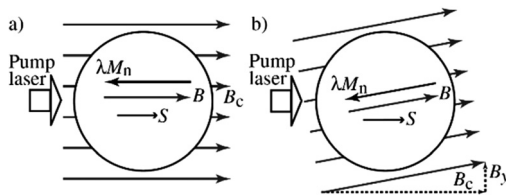


FIG. 7. Operation of a comagnetometer NMR gyroscope. Reprinted with permission from T. W. Kornack, *et al.*, Phys. Rev. Lett. **95**, 230801 (2005). Copyright 2005 American Physical Society.

DC comagnetometers have some advantageous features compared with conventional NMR gyro designs. First, because the alkali species sees a very low magnetic field, suppression of spin-exchange relaxation in the alkali can occur, resulting in much higher magnetometer sensitivities and improved angle-random-walk. Although SERF magnetometry can be used to improve the angle-random walk of spin-precession NMR gyroscopes, current schemes require complex synchronous modulation and probing of the alkali spins.<sup>69</sup> Second, the alkali-noble gas DC comagnetometer can be made largely insensitive to magnetic field gradients, transients, and light shifts while improving the rotation sensitivity bandwidth and dynamical response.

## F. Laser technology

Until recently, all commercial atomic clocks and magnetometers have used an alkali discharge lamp to create the light used for optical pumping and state detection. Discharge lamps produce low-noise optical fields on resonance with the relevant optical transitions in alkali atoms, but require considerable power to initiate and sustain the discharge, typically around 1 W. Since 1980, lower power, more efficient, and higher spectral purity semiconductor lasers have emerged as an attractive alternative for both Cs beam clocks<sup>71–74</sup> and Rb vapor cell clocks.<sup>74</sup> Because light from appropriately designed lasers can be at a single optical frequency, there is no need for spectral filtering in optical pumping experiments to create the initial population imbalance. The light can also be easily and quickly modulated in intensity and frequency, which is difficult to do with discharge lamps. NIST-7, an atomic-beam-based primary frequency standard, used semiconductor lasers for optical pumping and detection of the final atomic state.<sup>75</sup> Commercial Cs beam clocks have also been adapted to incorporate lasers.<sup>76</sup>

To be useful for precision atomic spectroscopy, lasers must satisfy some criteria. First, they must be able to be tuned to a relevant optical transition in an alkali atom species in the 750 nm–900 nm range. The lasers must also operate at a single optical frequency, which usually implies lasing in a single longitudinal and transverse mode. A narrow linewidth is also required: below about 100 MHz for pressure-broadened buffer gas cells and below  $\sim 1$  MHz for evacuated cells. A low relative intensity noise is desirable; discharge lamps usually operate near photon shot noise, and so the use of a laser usually increases the noise in an instrument. And finally, the laser ageing and mode-hop properties should be

sufficient to support long-term locking of the laser wavelength to a fixed optical transition.

Vertical cavity surface-emitting lasers (VCSELs)<sup>77–80</sup> are a unique type of semiconductor laser, in which the light is emitted perpendicular to the plane of the wafer. The laser, shown schematically in Fig. 8(a), is formed by a thin quantum-well gain region grown between two high-reflectivity distributed Bragg reflector (DBR) mirrors. Current flow is confined to a small area in the active region by modifying the material around this region appropriately. Because of the extremely small mode diameter (as low as several microns), the threshold currents of this type of laser can be very low, typically around 1 mA for commercial devices<sup>81</sup> and even lower for research devices.<sup>82</sup> This low threshold current means that, unlike edge-emitting lasers, a VCSEL can produce coherent light with only a few mW of electrical input power. The small cavity size (also only a few microns) implies that the laser can have a very high modulation efficiency, sometimes extending to near 10 GHz. The linewidth of commercial VCSELs is typically around 50 MHz, making them suitable for optical pumping experiments in low-pressure buffer gas cells.

The advantages of VCSELs for atomic spectroscopy and atomic frequency references were identified in the 1990s.<sup>85–87</sup> It was realized at that time that the low threshold currents and corresponding low power consumption could be a great advantage for low-power instruments.

Modulated VCSELs were shown to be suitable for various types of nonlinear spectroscopy, including coherent population trapping.<sup>84</sup> A key requirement for high-contrast CPT is that the two excitation fields be of roughly equal amplitude and have sufficient intensity to optically pump the atoms efficiently into the coherent “dark” state. As shown in Fig. 9, the excitation fields can be either the carrier and one first-order sideband (for modulation at the atomic hyperfine frequency) or the two first-order sidebands (for modulation at the first sub-harmonic). Since at least one modulation sideband is always required, it is usually important to obtain a modulation index near unity at GHz frequencies. Most commercial VCSELs can be modulated with a sufficient modulation amplitude to create large first-order sidebands on the optical carrier with only about 1 mW of RF power. It has also been found that the modulation efficiency can be enhanced by adding an external reflector at a specific distance from the laser.<sup>86</sup> The non-zero linewidth enhancement factor in these lasers implies that high-frequency current modulation produces both AM and FM modulation, leading to somewhat

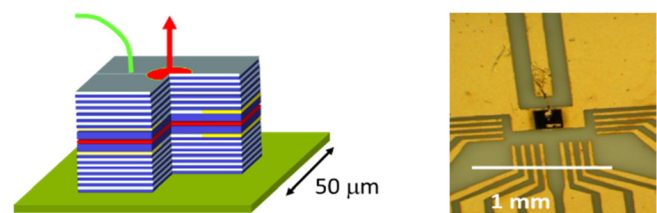


FIG. 8. (a) Schematic of a vertical cavity surface-emitting laser (VCSEL). A quantum well gain region, shown by the horizontal red region, is grown between two DBR mirrors (blue/white), which form the laser cavity. Threshold currents below 1 mA are possible with VCSELs. (b) Photograph of a commercial VCSEL die mounted to a baseplate and wire-bonded.

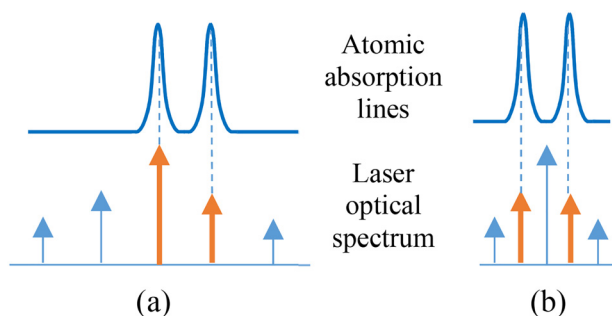


FIG. 9. (a) Excitation of a CPT resonance using a laser modulated at the atomic hyperfine frequency. The optical carrier and first-order sideband form the  $\Lambda$ -system that interacts with the atoms. (b) Excitation of a CPT resonance using a laser modulated at one-half the atomic hyperfine frequency. The two first-order sidebands form the  $\Lambda$ -system that interacts with the atoms.

asymmetrical sidebands in the optical spectrum. Interestingly, VCSELs can be used in compact instruments without the need for optical isolators. This is unusual for semiconductor lasers and is indeed fortunate since most optical isolators are large and expensive. The insensitivity to optical feedback is probably due to the proximity of reflecting surfaces and because the first optical component in the beam path is usually a high-attenuation neutral density filter.

VCSELs now are the basis of most instrumentation being developed with chip-scale atomic technology. They are commercially available at most of the relevant wavelengths for Rb (780 and 795 nm) and Cs (852 and 894 nm) with small enough current apertures to generate light in a single transverse, polarization and longitudinal mode. They have threshold currents below 1 mA (and as low as 200  $\mu$ A), a spectral linewidth of 50–100 MHz, modulation bandwidths of  $\sim$ 5 GHz, and can generate up to 1 mW of optical output power. Their optical frequency tunes with current by about 300 GHz/mA, about 100 times more than edge-emitting lasers, and with temperature by about 30 GHz/K. The low threshold current is critical in enabling low-power atomic instrumentation; edge-emitting lasers typically have threshold current well above 10 mA, and hence require considerably more power to operate. The broad spectral linewidth is problematic for some spectroscopic applications, but for vapor cells containing buffer gases, where the transition linewidth is collisionally broadened to 1 GHz or more, the large FM noise of the laser causes only minimal degradation in the clock performance.<sup>87</sup> When lower buffer gas pressures (below 100 Torr) are used, the FM noise of the laser can contribute significantly to the clock instability, however.<sup>88</sup>

Some VCSELs have been developed specifically for chip-scale atomic devices.<sup>83,89</sup> In one design,<sup>90</sup> the VCSEL was grown with an integrated photodetector to collect the light reflected back toward the VCSEL from a surface. VCSELs lasing at 894 nm with a threshold current of 0.32 mA at an elevated temperature (110 °C) have also been developed for application to chip-scale atomic clocks.<sup>91</sup> These lasers were able to produce over 1 mW of output power with only 3 mA of input current at 90 °C.

In many chip-scale atomic devices, the laser is placed in close thermal contact with the alkali vapor cell. Because the cell must operate at elevated temperature (typically between

80 and 150 °C), the VCSEL must also operate at that temperature in this configuration. If the VCSEL is designed to operate at lower temperature, the threshold current typically increases as the temperature rises because of the mismatch between the cavity resonance and the wavelength of highest gain in the semiconductor. VCSELs at 895 nm have been designed to address this problem by intentionally detuning the optical cavity from the gain peak at room temperature such that the coincidence of the two is better at elevated temperature.<sup>91,92</sup> Extended lifetime testing of commercial 795 nm lasers at elevated temperature and current has been carried out in the context of magnetometers for space missions.<sup>93</sup> This testing suggested that VCSELs from some suppliers can support mission durations as long as 17 years without failure. However, age-related changes in wavelength tuning and mode-hops still may present a problem.

Vertical external cavity surface emitting lasers (VECSELs) are composed of the gain region and lower Bragg mirror of a standard VCSEL, but the upper Bragg mirror is replaced with a conventional mirror in an external cavity configuration. Usually a frequency-selective element such as an etalon is placed in the external cavity to force single-frequency operation. Because of the large amount of coherent optical energy stored in the external cavity, much narrower laser linewidths can be achieved as compared with VCSELs. In addition, higher output power is typically achieved, since the mode area on the chip surface can be expanded with appropriate design of the external cavity.

It is possible to create an external cavity in which the two polarization modes oscillate at different optical frequencies. This can be done through the introduction of a birefringent plate into the external cavity, which causes a difference in the roundtrip phase delays for the two polarizations.<sup>94</sup> With appropriate design, the difference in optical frequencies can be made approximately equal to the ground state hyperfine transition in alkali atoms. With appropriate feedback, the difference frequency of the two optical fields can be locked to an external RF oscillator, creating a highly coherent beatnote at the external oscillator frequency.<sup>95</sup> In this configuration, the laser is well-suited to the generation of coherent population trapping resonances in alkali vapor cells. While the operating power currently remains too high for useful operation in a chip-scale atomic clock, this approach provides an interesting alternative to direct modulation of a VCSEL, with the advantages of higher optical output power and narrower optical linewidth.

VECSELs with microfabricated external mirrors and short (25  $\mu$ m) external cavities have also been developed at 850 nm.<sup>96</sup> These offer the fabrication and size advantages of VCSELs, while simultaneously achieving higher optical output powers and narrower linewidths. Threshold currents near 2 mA were achieved with a differential quantum efficiency of 41% and a maximum output power of 2.1 mW.

## II. MICROMACHINED ALKALI VAPOR CELLS

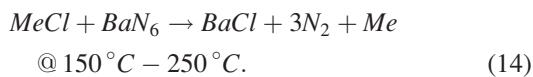
### A. Alkali metals

A key component in many of the chip-scale atomic devices discussed here is the cell that confines the alkali atoms

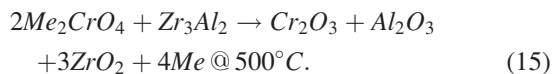
and buffer gas. The cell accomplishes several tasks. First, it confines the atoms to some region of space so they can be excited and probed by the laser fields. Second, it prevents reactive contaminants such as oxygen and water from entering the cell and oxidizing the alkali atoms. Finally, the cell prevents non-reactive contaminants, such as He and N<sub>2</sub>, from entering or leaving the cell and causing shifts in the frequency of the alkali atom transitions.

Because of the strong reactivity of alkali metals, they must be handled in an inert atmosphere and stored in hermetically sealed containers or under an inert liquid. There are several ways in which pure alkali metal can be obtained. First, it is possible to purchase pure alkali metal, usually sealed and shipped in a sealed glass ampoule under an inert atmosphere. If the ampoule is broken in an inert environment (for example, an anaerobic glovebox), the metal can be transferred between vessels using a pipette or by coating the tip of a pin. Because some amount of oxygen and water vapor is usually present even in highly controlled environments, an exposed sample of alkali metal might oxidize over the course of several hours to several days unless resealed in a hermetic container.

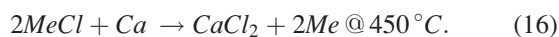
Alkali metals can also be produced by reacting stable alkali-containing compounds with reducing agents or by dissociating them with heat or light. For example, alkali chlorides (salts) can be reacted with barium azide, which decomposes at 150°C–250°C, to produce alkali metal, BaCl, and nitrogen gas<sup>97</sup>



Here, *Me* refers to the alkali metal. Alkali chromates (or molybdates) can be reacted with zirconium, titanium, aluminum, or silicon at a much higher temperature (above 350°C) to produce elemental alkali metal<sup>97–100</sup>



Although higher temperatures are required to drive these reactions, no residual gases are produced allowing a vacuum to be maintained throughout the reaction. This reaction is commonly used to deposit alkali metals as getters inside vacuum tubes. Alkalies can also be produced by reduction of MeCl by Ca<sup>97,101</sup> or Mg



Finally, alkali azides can be decomposed with elevated temperature<sup>97</sup> or ultraviolet illumination,<sup>102</sup> releasing nitrogen gas



It is also worth noting that alkali metals are strongly absorbed by graphite, making this material an excellent getter for Cs and other alkali metals. Gold is also known to react

with alkali metals<sup>103</sup> and should generally be avoided in alkali vapor cells.

Alkali metal can be also extracted from alkali ions infused into a material such as glass<sup>104</sup> or ceramic<sup>105–107</sup> with a mechanism similar to lithium ion batteries. Electrodes placed around the material create an electric field that causes alkali ions to diffuse to the cathode surface where they recombine with electrons to create alkali metal.

## B. Cell fabrication

The cells used in most vapor cell atomic clocks, shown in Fig. 10(a), are made using glass-blowing techniques. This involves melting and shaping glass with high-temperature flames. Often Pyrex or an equivalent borosilicate glass is used because of its low softening temperature. Fused silica can also be used if enhanced transparency in the ultraviolet is required. A typical cell fabrication process begins with a glass chamber such as a glass-blown spherical shell or a hollow cylinder, with windows fused onto either end. A filling tube connects the interior of the glass cell to a vacuum pump and a sealed ancillary chamber containing highly pure alkali metal. The chamber is evacuated and extensively baked and often cleaned further with a plasma discharge. The ancillary chamber is then opened with a glass break-seal, and the alkali metal is distilled into the main chamber. The main chamber is back-filled with an appropriate combination of buffer gases and is removed from the manifold by melting the filling tube closed. With this method, cells can be fabricated with volumes ranging from several cubic meters down to roughly 10 mm<sup>3</sup>. It becomes increasingly difficult to fabricate cells with volumes smaller than a few mm<sup>3</sup> with this method, mainly because handling them becomes difficult.

Early attempts to adapt conventional glass-blowing techniques for the fabrication of millimeter-scale cells involved the use of hollow-core glass fibers sealed with light from a CO<sub>2</sub> laser.<sup>108</sup> The glass fibers allowed for small cell dimensions, while the CO<sub>2</sub> laser allowed for highly localized heating of the glass. Some related techniques for confining alkali atoms into even smaller structures with dimensions on the order of an optical wavelength have been developed.<sup>109–111</sup> While these latter types of cells appear well-suited for certain types of spectroscopy, the very small cell dimension may limit their application in microwave atomic frequency references

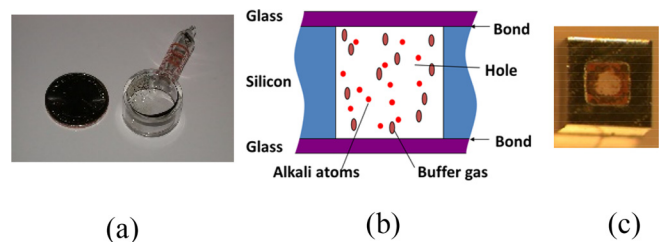


FIG. 10. (a) Photograph of a traditional glass-blown alkali vapor cell. Cells made using glass blowing are used in most atomic clocks and magnetometers. (b) Overall structure for MEMS-based alkali vapor cells. Atoms are confined in a cavity etched in a Si wafer. Glass wafers are bonded to the top and the bottom of the Si to seal the cell allowing optical access. (c) Photograph of a silicon/glass cell.

due to relaxation from rapid collisions of the atoms with the cell walls, as discussed above.

While small cells can be fabricated with the method described above,<sup>63,112</sup> there are several significant detracting features. One is that the cells must be made one by one; fabricating large numbers of cells therefore takes considerable time. Another is that the shape of the cell does not lend itself to easy integration with other optical components. Finally, each cell is slightly different in size, shape, and in the pressure of the buffer gas contained inside it. More sophisticated cell fabrication techniques were therefore developed based on micromachined structures in silicon.<sup>113</sup>

The overall structure for many of these types of cells is shown in Fig. 10(b). The alkali atoms are confined in a cavity etched in a wafer of Si, and glass wafers are bonded to the upper and lower surfaces of the Si forming a hermetic seal. The glass windows allow optical access to the cell from the top and the bottom. This design offers several advantages over glass-blown cells. The first is that cells with sub-millimeter dimensions can be made quite easily by defining the etch pattern appropriately and by choosing the thickness of the Si wafer. The process is also, in principle, easy to scale in size, simply by changing these parameters. Another is that many cells can be made on the same wafer by parallel etching of many cavities. Finally, the flat upper and lower surfaces and well-determined thickness of the cell enable easy integration with other optical components. Disadvantages of this structure are that it allows light to enter only from two opposing sides and that it is therefore difficult to integrate with light beams propagating in the horizontal direction. A photograph of a cell fabricated at NIST in 2003 is shown in Fig. 10(c).

In some cells, a low-outgassing epoxy has been used to seal the layers of the cell to each other<sup>111,114,115</sup> or to seal a glass tube over a hole in the cell window for convenient filling using traditional glass blowing.<sup>114,116</sup> It has been found that, however, the outgassing of the glue can result in gas contamination inside the cell<sup>115</sup> or cell failure after thermal cycling.<sup>116</sup>

For most cells, the glass and Si are bonded using anodic bonding.<sup>117</sup> This technique is widely used in the MEMS community for sealing some types of glasses to conductive materials. To form the bond, the surfaces of the glass and silicon wafers are polished and cleaned and placed in contact with each other. The wafers are then heated to near 300 °C, at which temperature impurity ions in the glass become mobile. A voltage of a few hundred volts is then applied to the exterior surfaces. The voltage causes the alkali and alkaline earth ions in the glass to diffuse toward the cathode and away from the glass-Si interface. Negatively charged oxygen ions drift toward the interface in the resulting space-charge field and react with the silicon at the interface to form SiO<sub>2</sub>, creating a strong bond between the glass and the silicon. This technique is advantageous for alkali vapor cells in that no materials other than Si and glass are used, meaning that the cells can be largely devoid of gaseous impurities. However, the high temperature needed to form the bond does limit the technique in some ways. This requirement necessitates the use of glass materials with a coefficient of

thermal expansion matched to the secondary material. If such materials are not used, the glass tends to crack upon cooling due to the resulting mechanical stress. In addition, alkali atoms can diffuse into the glass at elevated temperature; it is precisely this diffusion (of Na and K) that is responsible for anodic bonding. If the cell is bonded at too high a temperature, alkalis contained within the cell can diffuse into the glass (or through the interface between the glass and the silicon) during bonding and be lost. Finally, it is challenging to incorporate features such as wax wall coatings into the cell fabrication process because of the lower melting temperature of the wax.

The general process for silicon-based cell fabrication is as follows. A polished silicon wafer is lithographically patterned and the cavities of the desired size are then etched through the wafer using either wet chemical etching or deep reactive ion etching. The cavities can also be created using abrasive machining or ultrasonic drilling. After etching, the wafer is cleaned and a piece of glass is anodically bonded onto one surface of the wafer forming a “preform.” Alkali atoms, or their precursors, are then deposited into the preform in some manner and a buffer gas is added to the chamber as desired. Finally, the cell is sealed by anodically bonding a second glass window to the upper surface of the silicon without exposure to air.

The leakage of He through the glass walls of the cell can cause pressure shifts of the clock transition and long-term drifts of the clock frequency. He induces a pressure shift<sup>17</sup> of  $\sim 10^{-7}/\text{Torr}$  for Rb and Cs, implying that if the He pressure in the interior of the cell were at atmospheric concentration ( $\sim 5$  ppm), a shift of  $\sim 4 \times 10^{-10}$  would result. The time constant for changes in He pressure inside a 1 mm<sup>3</sup> microfabricated alkali vapor cell with 0.3 mm borosilicate glass windows is several months, implying a drift rate of  $\sim 3 \times 10^{-12}/\text{day}$  is possible due to this effect. Cells have been fabricated<sup>118</sup> using windows made from aluminosilicate glasses, which have considerably reduced He permeation rates compared to borosilicate glasses.<sup>119</sup> These cells show much lower frequency drift when placed in a He environment.

### C. Introduction of alkali atoms

The most challenging part of the fabrication of cells as described above is the deposition of the alkali metal into the cell and subsequent sealing. It is of course possible to use traditional filling processes used for glass-blown cells described above, in which the filling tube ends not in a glass cell but on the glass window of a silicon/glass cell such as that shown in Fig. 10(c).<sup>90,120</sup> However, these processes typically leave a sealed glass stem protruding from the cell, which makes it difficult to assemble the cell with other optical components. In addition, the cells must be filled and sealed one by one, which is costly and time-consuming. In Secs. II D and II E, we review the various ways in which alkali metal cells have been fabricated using processes that could be adapted for large-scale parallel production of many cells simultaneously. These processes take advantage of a great strength of the use of micromachined silicon and the cell volumes can be etched at the wafer scale in parallel after

lithographic patterning. Cells can therefore be made in large numbers with a single process sequence.

As described above, the typical optimal buffer gas pressures for a cell of volume  $1\text{ mm}^3$  are in the range of 200 Torr to 600 Torr. The use of anodic bonding in cell fabrication can limit the types of buffer gases that are used. For example, the high voltage applied in the final bonding step is applied under the buffer gas atmosphere. The use of neon as the buffer gas can lead to arcing within the bonding chamber if care is not used in the design of the cell holders and electrodes within the cell filling chamber. In some cases, a weak bond is established inside the vacuum chamber at low voltage to prevent arcing, and the cell is then rebonded with a higher voltage under a gas less susceptible to breakdown, such as air.<sup>121</sup>

The simplest method conceptually for transferring alkali metal into the vapor cell is the direct deposition of pure metallic alkali into the cell preform using a pipette or pin,<sup>122–124</sup> as shown in Fig. 11. The cell preform is placed inside an anaerobic chamber filled with a dry, inert atmosphere such as  $\text{N}_2$ . An ampoule containing metallic alkali metal is broken inside the chamber and a small amount of the metal is transferred to the cell preform using a pipette or pin. A glass lid is then placed on the preform and the assembly transferred to a bell jar contained within the anaerobic chamber. The bell jar is evacuated and backfilled with the desired buffer gas, after which the final anodic bonding step, carried out inside the bell jar, seals the cell.

This process requires minimal custom vacuum equipment and can, in principle, be adapted to achieve parallel filling of cells on a wafer using, for example, micromachined arrays of pins or pipettes. However, because of the more rapid oxidation of smaller amounts of alkali metal, this method may be challenging to adapt to cell sizes significantly smaller than 1 mm. Micro-pipetting can also be done under a dodecane liquid environment to prevent oxidation of the alkali metal.<sup>125</sup> Cells of this type have demonstrated lifetimes of many years with no obvious signs of degradation or

significant changes in the atomic resonance frequency due to internal chemical reactions or permeation of gases from outside the cell.<sup>126</sup>

Alkali metal can also be transferred into cells sealed in other ways, for example, by chasing the alkali metal into an array of cells by heating of micromachined capillaries connecting them.<sup>127</sup> The cells are then sealed by flowing wax into the filling channels. Wax can also be used to coat alkali metal droplets into “micropackets,” which can be handled in air.<sup>128</sup> These can then be sealed inside the cell and heated with a laser to release the alkali metal.

The challenges associated with the handling of pure alkali metal can be circumvented by producing the alkali metal as part of the fabrication process itself. As described above, alkali metal can be evolved through the reaction of alkali-containing chemical precursors such as alkali chlorides, azides, and chromates. These precursors can be handled in air, mixed with an appropriate reducing agent, and then activated either in the cell itself after the final bonding step or in a vacuum system containing the cell preform before bonding.

This latter approach, shown in Fig. 12, has been used at NIST for many years.<sup>129</sup> Here, a droplet of a  $\text{BaN}_6$  solution into which  $\text{CsCl}$  or  $\text{RbCl}$  has been dissolved is placed in a small glass ampoule with a  $\sim 0.5\text{ mm}$  opening in one end. The ampoule is positioned above the preform opening inside a chamber evacuated to below  $10^{-5}\text{ Torr}$  and heated. The alkali metal produced in the reaction leaves the opening in the ampoule as an alkali beam and a small quantity of alkali metal is deposited into the bottom of the preform. The nitrogen gas generated during the reaction is pumped away and the residual  $\text{BaCl}$  and  $\text{Ba}$  produced in the reaction remain largely in the ampoule. A buffer gas is then added to the chamber and the final anodic bonding step is carried out within the chamber itself.

The chemical reaction can also be made to occur in the cell during bonding. In early cells made at NIST, a  $\text{CsCl} - \text{BaN}_6$  mixture was deposited directly into the cell and reacted

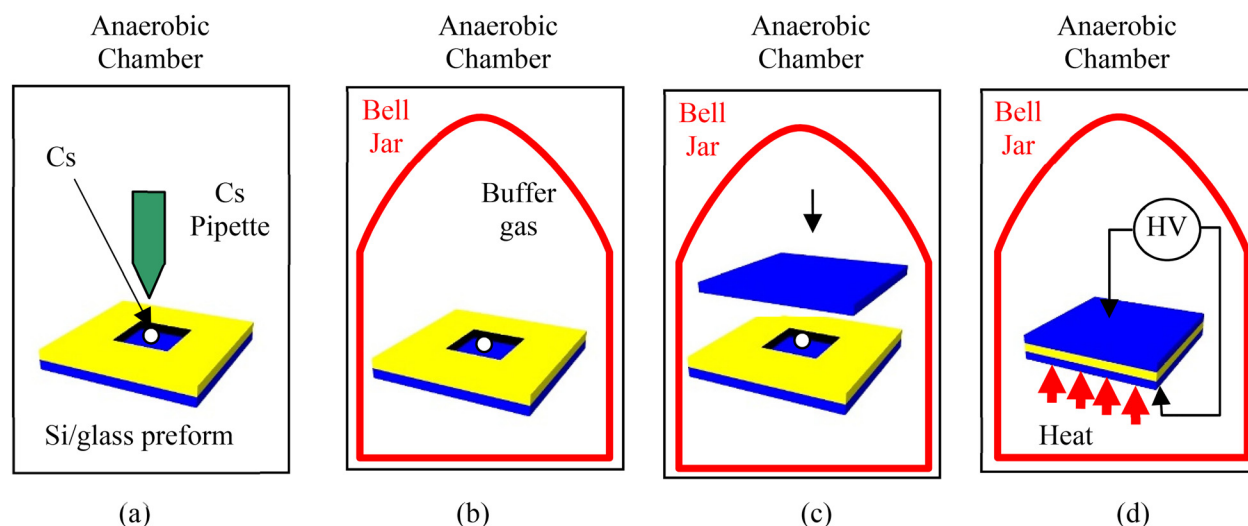


FIG. 11. Cell filling using transfer of metallic alkali. (a) Inside an anaerobic chamber, a small quantity of alkali metal is deposited into the cell preform using a pipette or pin. (b) The assembly is transferred to a bell jar, which is backfilled with the desired buffer gas pressure. (c) A second glass wafer is lowered onto the top of the silicon wafer. (d) The final anodic bonding step is carried out sealing the cell.

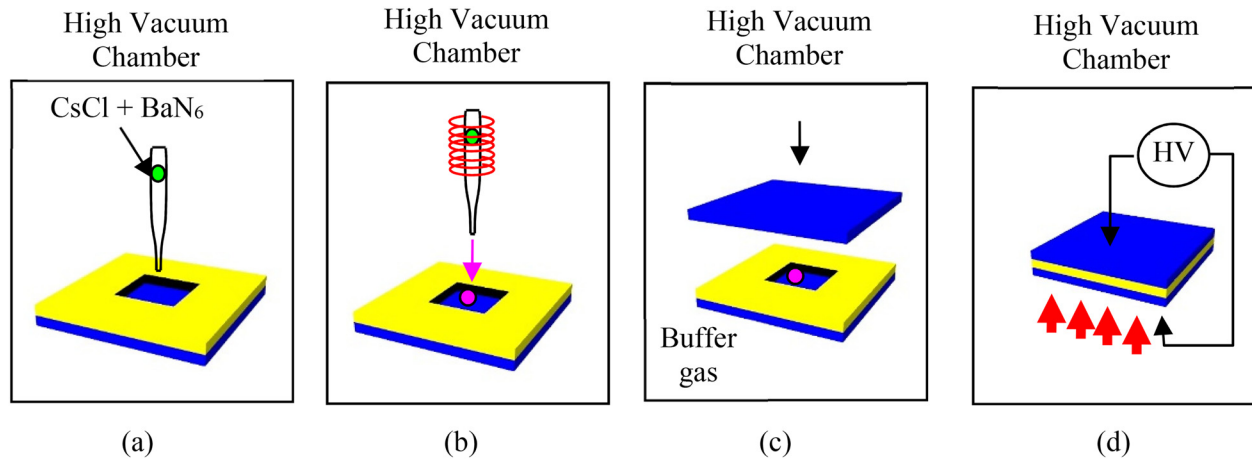


FIG. 12. *Ex-situ* cell fabrication using chemical reaction outside the cell volume. (a) Inside a high vacuum chamber, alkali metal is created through a chemical reaction in an ampoule suspended above the cell. (b) The alkali metal is deposited into the cell preform in an atomic beam. (c) A buffer gas is added and the cell lid is placed on the top surface of the silicon. (d) Anodic bonding is carried out in the vacuum chamber.

as part of the anodic bonding step.<sup>122</sup> Cells made in this manner were found to have an unacceptably high drift of the atomic hyperfine resonance frequency<sup>129</sup> as a result of changing buffer gas pressure, and this method was therefore abandoned in favor of the ampoule method described above.

The  $\text{Cs}_2\text{CrO}_4$  reaction described above produces much less residual gas, and hence is better suited to *in-situ* activation. Cells have been fabricated<sup>100,130</sup> by placing a small pill<sup>131</sup> of  $(\text{Cs}_2\text{MoO}_4)/\text{Zr}/\text{Al}$  (or  $(\text{Cs}_2\text{CrO}_4)/\text{Zr}/\text{Al}$ ) inside the vapor cell preform before bonding, as shown in Fig. 13(a). The cell is then sealed under vacuum or the desired buffer gas mixture. After sealing, the cell is removed from the chamber and the pill is illuminated with light from a high-power laser, which heats the pill to its reaction temperature and releases the alkali metal. A photograph of such a cell is shown in Fig. 13(b).

This cell fabrication method is simple and avoids the somewhat complex deposition inherent to the processes described above. Since the pill is stable in air, it can be

handled conveniently and the vacuum system need only be able to perform anodic bonding. This process has been adapted for wafer-level fabrication in a commercial anodic bonding machine.<sup>121</sup> Upon reaction, the pill gets  $\text{N}_2$ , implying that  $\text{N}_2$  cannot be used as a buffer gas. As mentioned previously,  $\text{N}_2$  is a commonly used buffer gas due to its ability to non-radiatively quench the alkali excited state population and hence reduce the effects of radiation trapping. However, gases other than  $\text{N}_2$ , such as Ne or Ar, can be used and appropriately temperature compensated.

A turning point in the buffer gas collisional shift as a function of temperature has been demonstrated with a Ne buffer gas alone at a temperature of  $80^\circ\text{C}$ , independent of the Ne density.<sup>132</sup> The turning point temperature can be increased<sup>133</sup> above  $80^\circ\text{C}$  through the addition of He. Diffusion of He out of the cell (through the borosilicate glass windows) resulted in a substantial frequency drift,  $\sim 5 \times 10^{-9}/\text{day}$ , which could possibly be alleviated by the use of different glasses as described below.

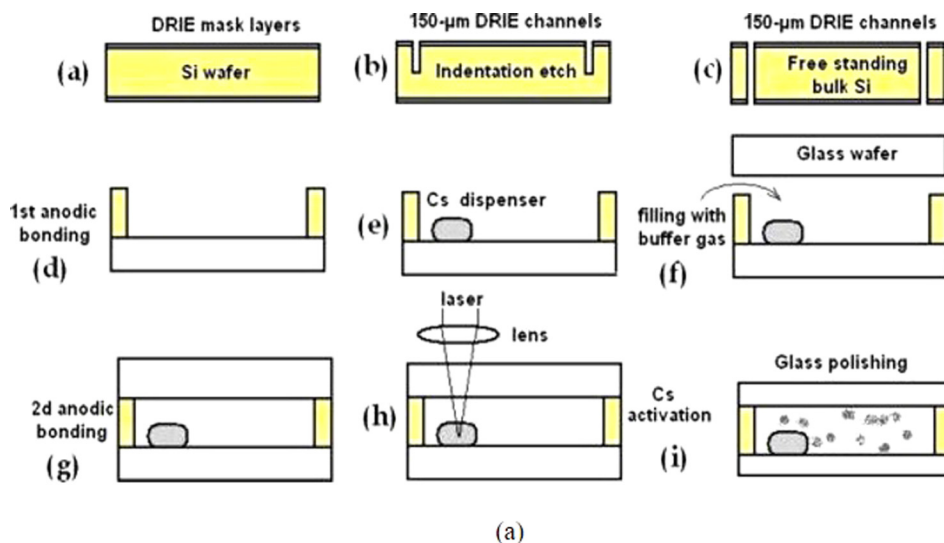


FIG. 13. Fabrication of microfabricated alkali vapor cells using compounds of  $(\text{Cs}_2\text{MoO}_4)/\text{Ti}/\text{Al}$ . (a) Filling method. Reprinted with permission from L. Nieradko *et al.*, *J. Micro/Nanolithogr. MEMS MOEMS* 7, 033013 (2008). Copyright 2008 SPIE. (b) Photograph of finished cell. Reprinted with permission from A. Douahi *et al.*, *Electron. Lett.* 43, 279–280 (2007). Copyright 2007 the Institute of Engineering and Technology.

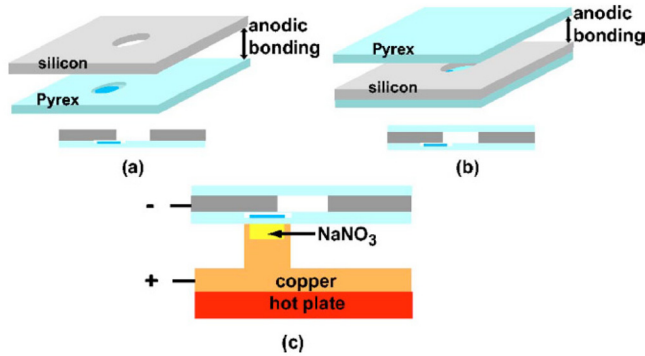


FIG. 14. Electrolytic fabrication of microfabricated alkali vapor cells. Reprinted from Rev. Sci. Instrum. 77, 076101 (2006). Copyright 2006 AIP Publishing LLC.

The  $(\text{Cs}_2\text{MoO}_4)/\text{Zr}/\text{Al}$  mixture can also be mixed with a paste-like binder material and deposited into cells using an automated epoxy dispensing tool, allowing for much faster deposition of the required materials.<sup>134</sup> In cells filled using this method containing a Ne buffer gas alone, a frequency drift below  $5 \times 10^{-12}/\text{day}$  was measured,<sup>134</sup> indicating that there are no significant changes in buffer gas pressure occurring due to the presence of the unreacted precursors. A similar fabrication process was developed that used an alkali dichromate in a titanium tablet.<sup>135</sup>

*Ex-situ* filling of cells has also been demonstrated,<sup>136</sup> in which an alkali metal dispenser containing an alkali chromate/molybdate is situated above the cell preform and the alkalis are deposited as a thermal beam through a shadow mask.

Many types of glass contain alkali atoms, usually originating from an alkali carbonate added to the glass precursors to control the melting point of the glass. These alkali atoms can diffuse in the glass at elevated temperature and in the presence of an electric field; it is this process that enables, for example, anodic bonding. Microfabricated alkali vapor cells have been made<sup>137</sup> by first creating a glass containing a substantial amount of Cs by heating a mixture of cesium carbonate and boron oxide to form a strongly cesiated glass. Pieces of this glass were then placed inside the Si-glass preform and the cell sealed in an argon atmosphere. The cell was heated to melt the cesiated glass onto the inner surface of the borosilicate glass window, and a high voltage was then applied across the glass from a  $\text{NaNO}_3$  electrode. Na ions diffused into the glass, displacing the Cs, which accumulated in solid form on the top window of the cell and formed a vapor. This process is shown in Fig. 14.

The decomposition of alkali azides has been also used to fabricate MEMS vapor cells. In an early demonstration,<sup>138</sup>  $\text{CsN}_3$  was deposited into a silicon/glass preform through a shadow mask, as shown in Fig. 15. The  $\text{CsN}_3$  was thermally evaporated with a very slow heating rate to avoid self-heating and possible explosion during deposition. After anodic bonding of the second wafer, the cell was extracted from the deposition chamber and irradiated with ultra-violet light to dissociate the  $\text{CsN}_3$  and release Cs and  $\text{N}_2$ . The final pressure of the  $\text{N}_2$  gas, which served as a buffer gas, could be controlled through the irradiation time.

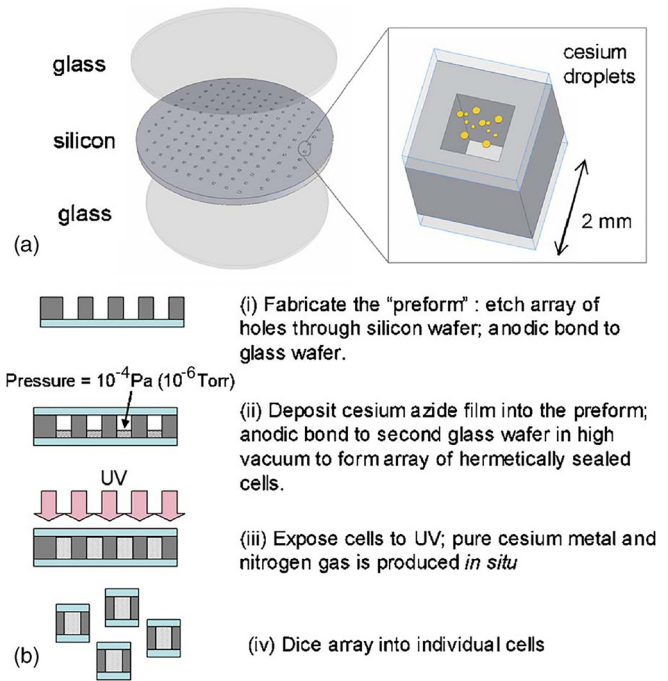


FIG. 15. Microfabricated alkali vapor cells filled using ultra-violet decomposition of  $\text{CsN}_3$ . Reprinted with permission from L.-A. Liew *et al.*, in Proceeding of Eurosensors (2007). Copyright 2007 AIP Publishing LLC.

Further work<sup>139</sup> showed that the  $\text{CsN}_3$  could be easily deposited inside the cells with good uniformity by first dissolving it in water and pipetting it into the cell preforms and that the UV irradiation time could be reduced to a few minutes instead of several hours by using a UV laser rather than a lamp. Finally, the alkali azide solution can be deposited on a microstructured material with large surface area to improve deposition consistency and efficiency and lower the reaction temperature.<sup>140,141</sup>

One challenge with the alkali azide cell filling method is that the final quantity of alkali metal is limited by stoichiometry and the desired buffer gas pressure. For example, if one atmosphere of  $\text{N}_2$  is desired in a 1 mm  $^{87}\text{Rb}$  cell, only  $1 \mu\text{g}$  of Rb is produced, which can subsequently be lost due to reactions inside the cell or diffusion into the cell walls at elevated temperature. It has been found that thin coatings of  $\text{Al}_2\text{O}_3$  applied to the interior window surfaces by atomic layer deposition could improve<sup>142</sup> the lifetime of the alkali metal inside a microfabricated cell at elevated temperatures by a factor of 100. It was also found that anodic bonding could be done without having to remove the  $\text{Al}_2\text{O}_3$  coating from the bonding surface of the glass. A more detailed assessment of the long-term physical stability of cells with  $\text{Al}_2\text{O}_3$  coatings filled using the  $\text{CsN}_3$  method was carried out.<sup>143</sup> By measuring the size of the alkali metal droplets observed on the inside glass surface of a microfabricated vapor cell as a function of time, it was determined that roughly  $1 \mu\text{g}$  of alkali metal would suffice for a cell operated at  $95^\circ\text{C}$  for 10 yr.

An important aspect of vapor cells used in atomic clocks is the stability of the buffer gas pressure over long periods. As described above, small changes in the pressure can lead to drifts of the clock output frequency through the pressure shift. The gas pressure can change if chemical reactions occur in

the vapor cell or if gases such as He leak into or out of the cell through the windows. Measurements of the long-term stability of the buffer gas in cells filled with the pipette method shown in Fig. 11 showed<sup>126</sup> a frequency drift of  $1.7 \times 10^{-13}$ /day in a clock incorporating such a cell after several years of operation. Cells fabricated using the alkali molybdate dissociation method have also been measured in a clock configuration<sup>144</sup> and showed a frequency drift of  $-5 \times 10^{-11}$ /day, consistent with slow permeation of the Ne buffer gas out of the cell through the glass windows.

#### D. Alternative cell geometries

It is sometimes the case that it is useful, particularly in the case of magnetometry, to have optical fields propagating in the cells in orthogonal directions. Cell geometries with two planar glass windows are cumbersome to use in this case, since the orthogonal beams must pass through the cell at an angle with respect to the cell surface. Several approaches have been developed to address this issue. A novel type of spherical cell geometry has been developed,<sup>145,146</sup> in which small glass bubbles were blown from blind cavities etched in silicon and capped with glass, as shown in Fig. 16. The silicon backside was then etched out to allow access to the cell interior and the cells filled with alkali metal using the deposition method shown in Fig. 12. These cells are particularly useful for NMR gyros where the self-field of the polarized noble gas in non-spherical cells can create important systematics.

Cells have also been fabricated with angled interior walls that can reflect light incident normal to the cell window surface into the transverse direction. The natural etch angle of silicon is  $54.7^\circ$  and it is therefore straightforward to fabricate cells with the interior walls at this angle using standard chemical etching. Cells with such angled sidewalls with dielectric anti-reflection coatings have been demonstrated.<sup>147,148</sup> The  $54.7^\circ$  angle of the silicon walls does not allow reflection of a vertical beam into the horizontal plane. However, it is possible to incorporate grating structures on the input windows to diffract the light entering the cell by an angle such that horizontal propagation is achieved after reflection from the silicon sidewall,<sup>149</sup> as shown in Fig. 17.

While anodic bonding has in most cases been used to fabricate small vapor cells with dimensions on the order of 1 mm, the approach has also been adapted for larger vapor cells. It is challenging to etch through thick silicon wafers



FIG. 16. Micro-glassblown alkali vapor cells. Reprinted with permission from E. J. Eklund *et al.*, *Sens. Actuators A* **143**, 275–280 (2008). Copyright 2008 Elsevier.

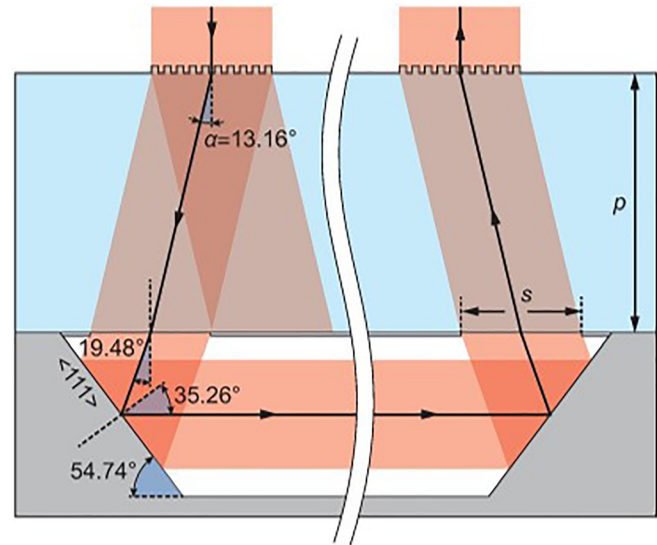


FIG. 17. Generation of horizontally propagating beams in a micromachined vapor cell using diffraction gratings on the input window. Reprinted with permission from R. Chutani *et al.*, *Sci. Rep.* **5**, 14001 (2015). Copyright 2015 Author(s), licensed under CC BY.

without damaging the surface polish and hence reducing the yield of the anodic bonding step. In order to make larger cells, a glass interposer with a hole drilled through it can be bonded to two etched silicon wafers, onto which the glass windows are bonded in turn.<sup>150</sup> GaP can also be used as the wall of the cell preform<sup>151</sup> if high thermal conductivity and low helium permeation are required. Glass can be bonded onto GaP at about  $200^\circ\text{C}$ , making this material useful for low-temperature cell filling also. Finally, anodic bonding between glass and sputtered SiN can enable the integration of metal feedthroughs into microfabricated alkali vapor cells.<sup>152</sup> The application of this approach to a triple-stack anodically bonded cell is shown in Fig. 18. In this process, the layers being bonded are all glass. Cr electrodes are deposited on the upper and lower glass layers and run from inside to outside the cell. A 200 nm SiN layer is deposited over the Cr and onto the glass where the Cr has been etched away to form a rim matching the walls of the middle glass layer to which the SiN is anodically bonded.

Since lithographic patterning and etching is used to define the cell geometry on the surface of a silicon wafer, parallel processing can enable the fabrication of many cells

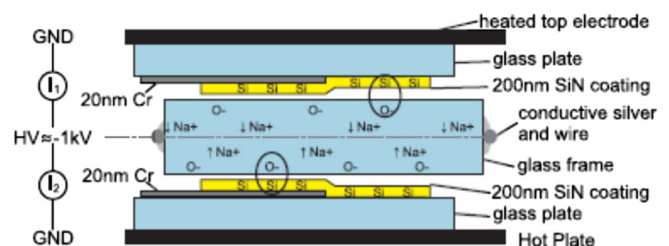


FIG. 18. Triple-stack anodic bonding of glass wafers using a sputtered SiN layer. This approach allows metallic electrical feedthroughs to extend from outside to inside the cell. In this visualization, the view is looking at one of the cell walls from the side, with the Cr electrodes extending out of and into the page. Reprinted with permission from *Appl. Phys. Lett.* **105**, 041107 (2014). Copyright 2014 AIP Publishing LLC.

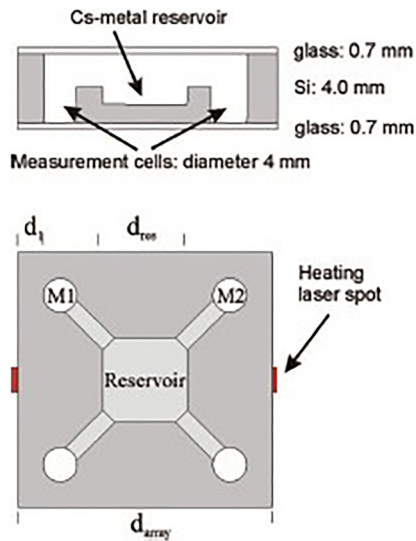


FIG. 19. Many alkali vapor cells can be connected to the same alkali reservoir to form cell arrays useful in, for example, magnetic imaging. Reprinted with permission from Rev. Sci. Instrum. **83**, 113106 (2012). Copyright 2012 AIP Publishing LLC.

on a single wafer using a single process sequence. The fabrication of cells in arrays was demonstrated quite early with the pipetting cell fabrication technique.<sup>124</sup> Processes have also been developed to separate and thermally isolate cells, while maintaining the rigidity of the array spacing by using a common window for all cells in the array.<sup>139</sup> Finally, multiple cells can be connected by channels to the same reservoir to form arrays of cells with the same buffer-gas pressure,<sup>153</sup> as shown in Fig. 19. Magnetometer arrays based on this multi-cell approach have also been demonstrated for magnetic gradiometry and imaging.<sup>153</sup> Glass cells with thicknesses between  $20\ \mu\text{m}$  and  $200\ \mu\text{m}$  have also been fabricated using lithographic glass etching techniques.<sup>154</sup>

### E. Alternatives to anodic bonding

One of the challenges associated with cell fabrication using anodic bonding is that the cell must usually be heated to near  $300^\circ\text{C}$ . This requirement has been a major limitation in, for example, the development of microfabricated cells with a wall coating instead of a buffer gas to suppress wall relaxation. Many wall coatings, such as paraffin, are unable to withstand temperatures substantially above  $100^\circ\text{C}$  and therefore are destroyed during the anodic bonding process.

Microfabricated alkali vapor cells have therefore been recently developed that use a low-temperature solder on silicon<sup>155</sup> or low-temperature cofired ceramic<sup>125</sup> for sealing, rather than anodic bonding, as shown in Fig. 20. In Ref. 155, thermocompression bonding at  $140^\circ\text{C}$  was used to seal a cell, the interior of which was coated with octadecyltrichlorosilane (OTS), which is stable up to  $170^\circ\text{C}$  in the presence of alkali vapor.<sup>156</sup> This cell showed a hyperfine resonance linewidth of under  $10\ \text{kHz}$ , suggesting that the wall coating was acting effectively to prevent depolarization. Low temperature anodic bonding techniques have also been developed, and silicon/glass alkali vapor cells have been fabricated by bonding at temperatures as low as room

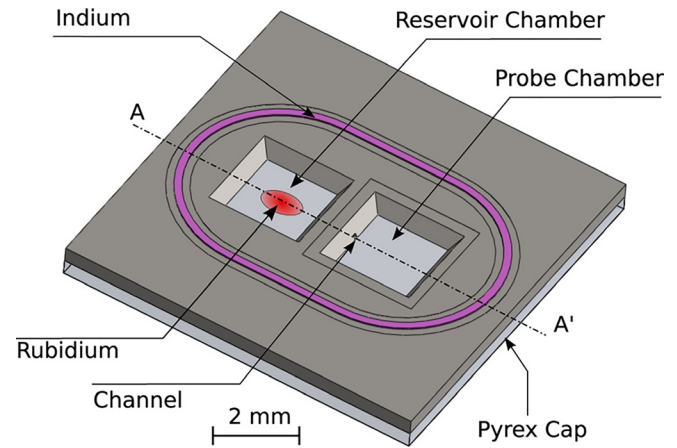


FIG. 20. Schematic of a process for microfabricating silicon/glass alkali vapor cells based on an indium seal. Reprinted with permission from Appl. Phys. Lett. **105**, 043502 (2014). Copyright 2014 AIP Publishing LLC.

temperature.<sup>157</sup> In these cells, the low-temperature bonding was enabled by a  $\sim 1\ \mu\text{m}$  layer of lithium-niobate-phosphate glass, which has a very high ionic conductivity and was deposited onto one surface of the second glass wafer. Cells have also been fabricated<sup>158</sup> using Cu-Cu thermocompression bonding, which may allow the use of different substrate materials.

Glass frits have also been used to seal potassium atoms and buffer gas inside an evacuated enclosure.<sup>101,140</sup> In this process, small channels  $\sim 10\ \mu\text{m}$  in cross-sectional size and  $\sim 1\ \text{mm}$  long are etched in a silicon frame to connect the inside of an etched silicon cavity with the outside. A  $\text{Bi}_2\text{O}_3\text{-B}_2\text{O}_3$  frit with a softening temperature below  $400^\circ\text{C}$  is then deposited in a frame pattern on a glass wafer to be used as the lid. Alkali precursors (in this case, KCl and Ca) are placed inside the cavity and the glass lid placed over the cavity such that the frit is situated over the channels. The alkali source is activated at  $450^\circ\text{C}$  under vacuum, any gas produced in the reaction is pumped away through the channels, and the chamber is then backfilled with the desired buffer gas. Finally, the lid is pressed against the silicon wafer at  $480^\circ\text{C}$  and the frit reflows into the channels creating a hermetic seal. This process was demonstrated in  $\sim 1\ \text{cm}$  glass cells, but should be easily adaptable to microfabricated cells.

There are several factors that traditionally contribute to the long-term frequency drift of vapor cell atomic clocks. The two most important factors are small changes in the buffer gas pressure due to leakage or diffusion through the cell walls and light shifts due to the slowly varying intensity of the interrogation light. The use of non-traditional materials and cell-filling processes raises the possibility that the drift of microfabricated alkali vapor cells could be significantly different from traditional glass-blown cells. In Table I, the measured drift rates for some microfabricated cells fabricated under a variety of conditions are listed. The best drift rate obtained so far is  $-8 \times 10^{-13}/\text{day}$  for a cell packaged in an evacuated enclosure after several months of operation. The long-term ageing of a number of commercial chip-scale atomic clocks deployed on the ocean floor has been monitored over a period of several years.<sup>159</sup>

TABLE I. Drift rates measured in microfabricated vapor cells.

Reference	Alkali filling method	Buffer gas	Drift	Temperature ( $^{\circ}\text{C}$ )	Notes
160	<i>In situ</i> BaN <sub>6</sub> +CsCl	150 Torr N <sub>2</sub> /Ar	$-2 \times 10^{-8}$ /day	85	Attributed to internal cell chemistry
129	<i>Ex situ</i> BaN <sub>6</sub> +RbCl	Not stated	$-5 \times 10^{-11}$ /day	90	Probably limited by cell tempo
161	Pure Cs (glovebox)	Not stated	$-8 \times 10^{-11}$ /day	80	Initial 20 days
161	Pure Cs (glovebox)	Not stated	$-8 \times 10^{-13}$ /day	80	After 100 days of operation
133	<i>In situ</i> 2Me <sub>2</sub> CrMb + Zr <sub>3</sub> Al <sub>2</sub>	He/Ne	$-5 \times 10^{-9}$ /day	94.6	Possibly due to He leakage out of cell
144	<i>In situ</i> 2Me <sub>2</sub> CrMb + Zr <sub>3</sub> Al <sub>2</sub>	100 Torr Ne	$-5 \times 10^{-11}$ /day	81	Consistent with Ne diffusion through glass
118	<i>Ex situ</i> BaN <sub>6</sub> +RbCl	200 Torr Ar/N <sub>2</sub>	$1.8 \times 10^{-7}$ /day	96	In chamber containing 500 Torr He; borosilicate glass
118	<i>Ex situ</i> BaN <sub>6</sub> +RbCl	200 Torr Ar/N <sub>2</sub>	$9 \times 10^{-10}$ /day	91	In chamber containing 500 Torr He; aluminosilicate glass
134	<i>In situ</i> 2Me <sub>2</sub> CrMb + Zr <sub>3</sub> Al <sub>2</sub> paste	60 Torr Ne	$-4 \times 10^{-12}$ /day	75	

Significant variation in the ageing behavior was observed from clock to clock, but the best units demonstrated ageing at or below  $2 \times 10^{-12}$ /day.

### III. MEMS-BASED ATOMIC CLOCKS

#### A. Introduction

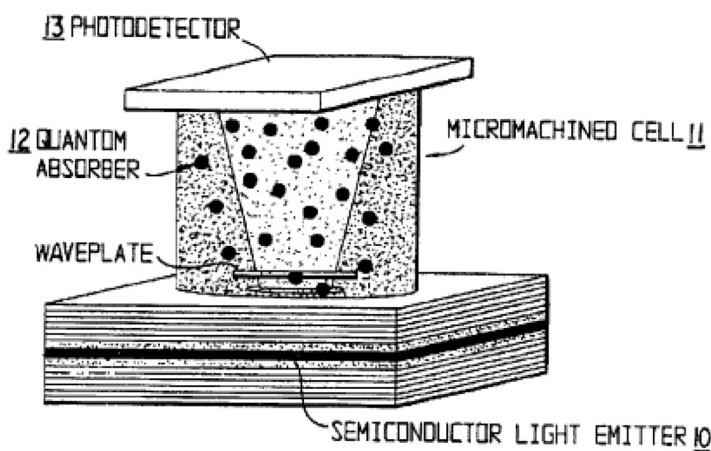
Throughout the 1990s, considerable effort was spent at companies around the world developing compact atomic clocks. This was driven largely by the cellular telephone industry, which was installing atomic clocks in cell-phone base stations to provide holdover timing in the event of a failure of the GPS timing system.<sup>48</sup> The baseline timing requirement for synchronization of cell-phone networks was an error of no more than  $10 \mu\text{s}$  over one day. Clocks were developed with a volume of  $\sim 100 \text{ cm}^3$  and operating on  $\sim 10 \text{ W}$  of power for this purpose. While these clocks served the cell phone industry needs well, they consumed too much power to allow them to be integrated into portable, battery-operated instruments.

With the proliferation of handheld consumer and military GPS receivers, it was realized that battery-powered atomic frequency references that could be integrated into such receivers could provide significant benefits to satellite-

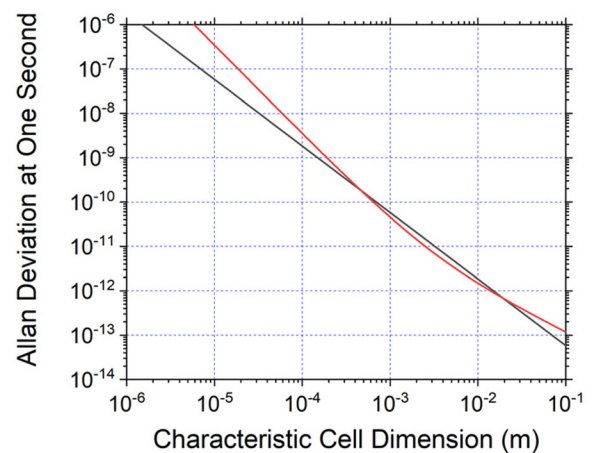
based navigation.<sup>162–164</sup> This, along with the potential application to secure wireless communications, was a strong motivation to begin the development of significantly lower power vapor cell clocks.

The use of VCSELs in atomic clocks was pioneered by a group at Westinghouse (now Northrup-Grumman) throughout the 1990s.<sup>85</sup> Their goal was to reduce the power consumption and size of a vapor cell clock using laser technology in place of the discharge lamp. Using miniature glass-blown vapor cells<sup>85,165</sup> in small microwave cavities, they achieved a clock short-term stability  $\sigma_y(\tau) < 2 \times 10^{-11}/\sqrt{\tau}$  and long-term drift of  $3 \times 10^{-12}$  at  $10^4 \text{ s}$  in a physics package with a volume of  $16 \text{ cm}^3$  running on a few hundred mW of electrical power.

This section deals with the development of atomic clocks incorporating silicon micromachined vapor cells as described above. The use of micromachining enabled the development of millimeter-scale physics packages that could be well thermally isolated from the environment and hence required very little power to heat. This, along with the use of VCSELs for the light source and the development of low-power RF synthesizers and control electronics, were the three key elements that enabled chip-scale atomic clock (CSAC) technology to succeed.



(a)



(b)

FIG. 21. (a) Conceptual design of a chip-scale atomic clock physics package. Reprinted with permission from L. Hollberg and J. Kitching, U.S. patent 6,806,784 B2 (2004). (b) Estimated stability as a function of cell size for a wall coating with  $N_B = 500$  (black line) and a  $\text{N}_2$  buffer gas at  $P = 76 \text{ Torr}$  (red line). Adapted from Appl. Phys. Lett. **81**, 553–555 (2002). Copyright 2002 AIP Publishing LLC.

## B. Design considerations

At the heart of any atomic frequency reference lies the physics package. This subsystem comprises at a minimum the alkali vapor cell, excitation and detection components, such as the light source and photodetector, and all the optical components. In large part, the physics package determines both the short- and long-term frequency instabilities of the clock. It also contributes directly to the size and power dissipation of the frequency reference. We discuss here several key considerations that impact the design of MEMS-based physics packages.

Some early suggestions of batch-fabricated atomic clocks centered on the idea of using etchable ceramics to form the gas cell and application-specific integrated circuit (ASIC) technology for the control electronics,<sup>165</sup> with the goal of producing a \$100 atomic clock that could hold 10 ns over 1 day. More specific designs for a chip-scale atomic clock and magnetometer physics package<sup>113</sup> envisioned an anodically bonded silicon/glass microfabricated alkali vapor cell coupled to a vertical-cavity surface-emitting laser in which the atoms were excited using coherent population trapping, as shown in Fig. 21(a).

Under some assumptions with respect to the signal amplitude and noise, it is possible to project the achievable Allan deviation as a function of cell size for a clock based on coherent population trapping,<sup>166</sup> as shown in Fig. 21(b). For cell sizes between 100  $\mu\text{m}$  and 1 mm, short-term frequency stabilities near  $10^{-10}$  at 1 s can, in principle, be achieved. The degradation of the frequency stability at small cell sizes arises for two main reasons. First, the transition linewidth increases, as shown in Fig. 2, due to increased collision rate with the cell walls and the buffer gas. Second, the cross-sectional area of the interrogating light field drops, leading to a smaller detected photon flux and hence a reduced signal to noise ratio. It is assumed here that the cell temperature is adjusted for constant optical absorption as a function of cell size and spin-exchange collisional broadening is ignored. The stability degrades as  $1/R^{3/2}$  under optimal buffer gas pressures and if the detection noise is limited by photon shot noise, as shown in Fig. 21(b).

The power required to run the physics package can be separated by component. Most commercially available VCSEL light sources require about 5 mW of power. However, it should be noted that VCSELs with threshold currents well below 1 mA have been reported and the use of such devices may therefore allow operation of a CSAC at considerably lower powers. The laser must also be temperature-stabilized to be able to lock the laser wavelength onto the atomic optical transition while avoiding large variations in output power. All viable CSAC designs produced so far have avoided the use of active cooling (with thermoelectric coolers, for example) in the thermal design, due to the inefficiency of this process. The laser is instead stabilized at a temperature above the maximum ambient temperature using only heating elements. Since the lifetime of a laser gets shorter as its operating temperature is increased, there is potentially a tradeoff between the lifetime of a chip-scale atomic clock and its operating temperature range. Accelerated lifetime testing<sup>89</sup> of VCSELs developed for

CSAC applications suggests that device lifetimes over 6 yr are reasonable for operating temperatures of 85 °C.

The cell must also be temperature stabilized to reduce temperature-dependent frequency shifts due to collisional processes within the cell. With temperature compensated buffer gas mixtures of a few hundred Torr, a temperature stability of  $\sim 0.1$  K is required to maintain a fractional frequency stability of  $10^{-12}$ . While the cell temperature must also be maintained above the maximum ambient temperature for the same reasons as the laser, an additional requirement is that the atom density in the cell be sufficient to produce a good CPT signal. For cells based on  $^{133}\text{Cs}$  or  $^{87}\text{Rb}$  of length 1 mm, a cell temperature in the range of 80 °C to 100 °C is optimal for conventional CPT interrogation. It is somewhat fortuitous that this temperature range fits well with the requirement related to the maximum ambient temperature.

The power radiated by a black body at temperature  $T_{\text{cell}}$  into an ambient temperature  $T_{\text{amb}}$  is given by the Stefan-Boltzmann law as

$$P_{\text{rad}} = \epsilon\sigma A [T_{\text{cell}}^4 - T_{\text{amb}}^4], \quad (19)$$

where  $\epsilon$  is the surface emissivity,  $\sigma$  is the Stefan-Boltzmann constant, and  $A$  is the surface area of the cell. For a cubic cell, this radiated power is plotted as a function of side length  $L$  for an emissivity of unity in Fig. 22. For a radiated power below 10 mW, the cell (or whatever parts of the physics package are hot) must be on the order of 1 mm in size. In addition, the cell must be sufficiently well thermally isolated that conduction and convection losses are small.

Because of the high operating temperatures of the cell and the laser, thermal isolation of both components is critical in achieving low power dissipation. In some designs,<sup>160</sup> the cell and laser are controlled independently, while in others,<sup>124</sup> they are controlled together at the same temperature. It should be noted that the thermal resistance cannot be made too high due to the presence of heat sources inside the physics package. The largest of these results from the DC current required to run the laser. The wall-plug efficiency of most VCSELs is in the range of 20%; most of the electrical power that drives the VCSEL therefore ends up as heat. If the thermal resistance

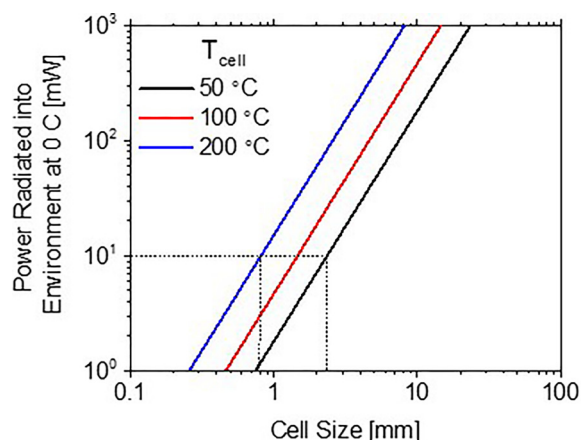


FIG. 22. Radiated power into a 0 °C ambient as a function of cell size for three different cell temperatures.

between the laser and package wall is too high, the physics package will overheat at high ambient temperatures simply due to this internal heat source. One way of solving this problem is to use a thermal link with a variable thermal resistance.<sup>167</sup> While such techniques have yet to be demonstrated in chip-scale atomic devices, they represent a compelling possibility for future design improvements.

A final key consideration is manufacturability and device cost. Because of the possibility for wafer-level processing and integration, micromachining techniques offer considerable advantage here if high device volumes are needed. Ideally, the physics package should have a simple design, such that either the entire physics package can be fabricated on a single wafer or the individual components can be fabricated and integrated in wafers. In either case, the result is that large numbers of physics packages can be fabricated with the same process sequence.

### C. Physics packages

The MEMS-based atomic clock physics package demonstrated in 2004 at NIST<sup>160,168</sup> is shown in Fig. 23. This device was vertically integrated, in the sense that the light beam propagated in a direction perpendicular to the substrate surface and components were integrated by stacking layers, one on top of the other. At the lower end of the device, a vertical-cavity surface-emitting laser was mounted onto a custom substrate of gold traces patterned on a rigid insulator (AlN, in this early design). A series of optics layers were positioned over the laser and held off the surface by a dual strip isolator. The optics included two neutral density filters, which attenuated the light beam to about  $10\ \mu\text{W}$ , a micro-lens, which collimated the beam to a diameter of about  $250\ \mu\text{m}$ , and a quarter-wave plate, which converted the light polarization from linear to circular.

The cell and heater assembly was mounted on top of the optics assembly. The cell heaters were pieces of thin glass with a thin layer of indium-tin oxide (ITO) deposited on the surface. ITO is a commonly used transparent, conductive material, and useful here since it allows light to pass through the windows of the cell while at the same time allowing for resistive heating via current flow along the window surface.

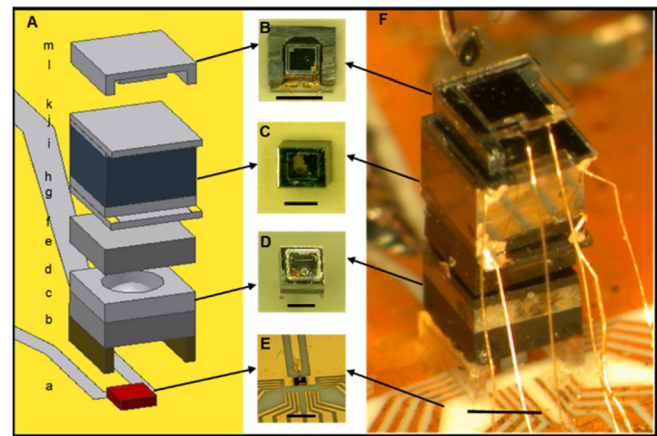


FIG. 23. A microfabricated atomic clock physics package. (A) Schematic of assembly. Layers from bottom to top: a, Glass ( $500\ \mu\text{m}$ ); b, Spacer ( $375\ \mu\text{m}$ ); c, ND filter ( $500\ \mu\text{m}$ ); d, Glass ( $125\ \mu\text{m}$ , not shown); e, Quartz ( $70\ \mu\text{m}$ , not shown); f, ND filter ( $500\ \mu\text{m}$ ); g, Glass/ITO ( $125\ \mu\text{m}/30\ \text{nm}$ ); h, Glass ( $200\ \mu\text{m}$ ); i, Si ( $1000\ \mu\text{m}$ ); j, Glass ( $200\ \mu\text{m}$ ); k, Glass/ITO ( $125\ \mu\text{m}/30\ \text{nm}$ ); l, Si ( $375\ \mu\text{m}$ ); and m, Glass ( $125\ \mu\text{m}$ ). Total height:  $4.5\ \text{mm}$ ; width and depth:  $1.5\ \text{mm}$ . Photographs (B) photodiode assembly, (C) cell assembly, (D) optics assembly, (E) laser assembly, and (F) the full atomic clock physics package realized as a microchip. The black lines in the photographs indicate  $1\ \text{mm}$ . Reprinted with permission from Appl. Phys. Lett. **85**, 1460–1462 (2004). Copyright 2004 AIP Publishing LLC.

The cell itself was fabricated with the *in-situ* MeCl/BaN<sub>6</sub> technique described above and had external dimensions of  $1.5\ \text{mm} \times 1.5\ \text{mm} \times 1.4\ \text{mm}$ . The heaters were wire-bonded to gold traces on the substrate with gold wires with a diameter of  $25\ \mu\text{m}$ . Finally, a photodetector was placed on the very top of the structure to monitor the light transmitted by the cell. The complete structure was  $4.2\ \text{mm}$  tall and had a square cross-section of  $1.5\ \text{mm}$ , leading to a total volume of less than  $10\ \text{mm}^3$ .

This first device, based on Cs atoms excited on their D2 line, had a resonance linewidth of  $7\ \text{kHz}$  and a measured short-term frequency instability of  $3 \times 10^{-10}/\sqrt{\tau}$ . The long-term frequency drift was quite large compared to larger vapor cell frequency references at  $1.6 \times 10^{-8}/\text{day}$ . The resonance linewidth, frequency as a function of time, and corresponding Allan deviation are shown in Fig. 24. The physics package operated on  $75\ \text{mW}$  of electrical power at an ambient temperature of  $46\ ^\circ\text{C}$ .

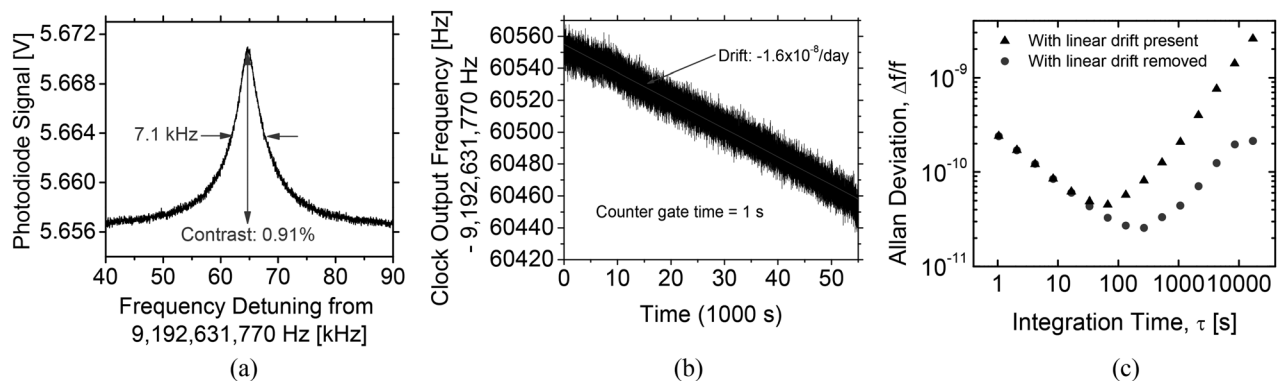
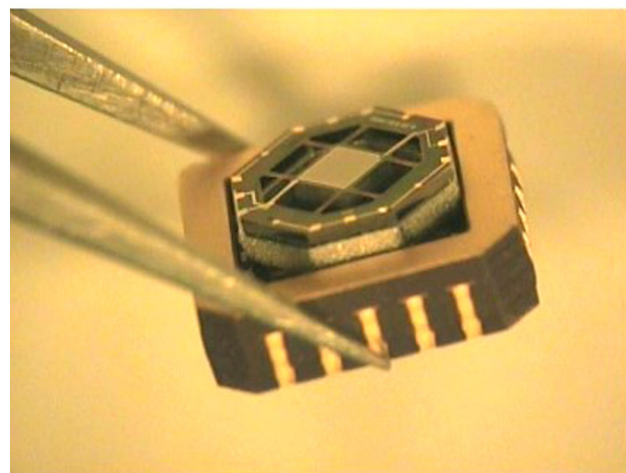
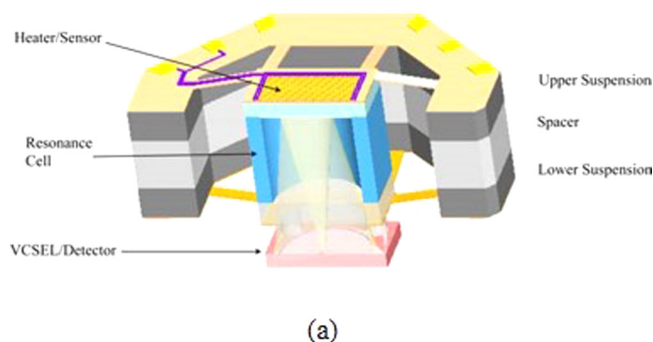


FIG. 24. Performance of an early chip-scale atomic clock physics package. (a) CPT resonance. The contrast here is defined as the ratio of the change in absorption due to the CPT effect to the total absorption. (b) Output frequency of a large-scale local oscillator locked to the CSAC physics package, as a function of time. (c) Allan deviation calculated from the data in (b). Reprinted with permission from Appl. Phys. Lett. **85**, 1460–1462 (2004). Copyright 2004 AIP Publishing LLC.



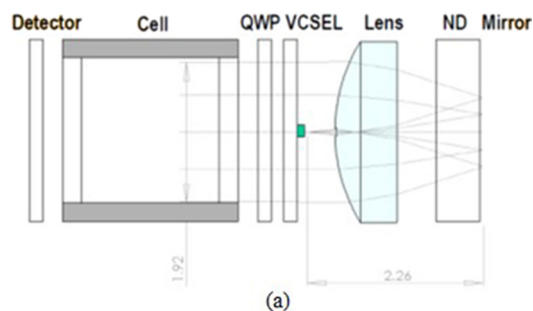
(b)

FIG. 25. A CSAC physics package design with a power dissipation below 10 mW. (a) Physics package design showing the physics package mounted on polyimide thermal isolation tethers and the folded optics design. (b) A photograph of completed physics packaged in polyimide suspension system. Reprinted with permission from R. Lutwak *et al.*, in *Proceeding of Precise Time and Time Interval (PTTI) Meeting* (2004), pp. 339–354.

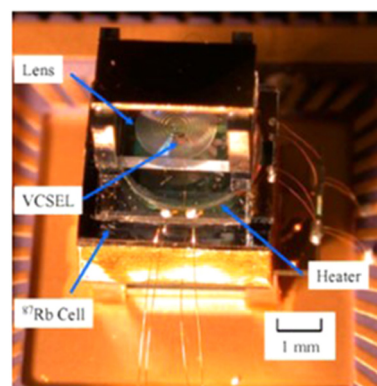
Several improvements to this device were demonstrated. First, the short-term frequency stability was improved by building a device that could be excited on the D1 line.<sup>169</sup> It is known that CPT resonances based on D1 excitation in vapor cells have considerably larger contrast and therefore result in better clock frequency stability.<sup>169–171</sup>

The large frequency drift in the CSAC physics package shown in Fig. 24 was most likely due to chemistry internal to the cell. The cell in this device was filled by depositing the CsCl/BaN<sub>6</sub> precursors into the cell itself and initiating the reaction to produce the Cs during the bonding process. As a result, the reactants remained in the cell after sealing. The drift was eliminated<sup>129</sup> at a level considerably below 10<sup>-10</sup>/day through the atomic beam deposition technique. Other cell-filling techniques have demonstrated even better long-term frequency stabilities.<sup>172–174</sup>

A major improvement in the power dissipation of CSAC physics packages was reported in Ref. 124. In this design, shown in Fig. 25, the physics package was suspended from thin polyimide tethers, on which metal traces were deposited to electrically connect the physics package with the control system. This suspension had a thermal conductance of only 0.14 mW/K, which allowed essentially radiation-limited



(a)



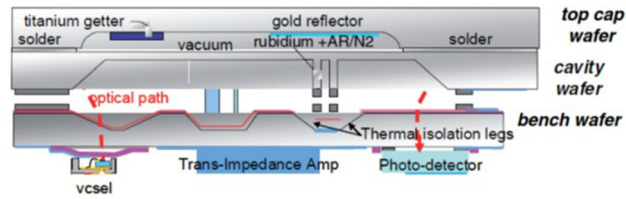
(b)

FIG. 26. A vertically integrated CSAC physics package. (a) Physics package design with folded geometry and (b) photograph of the assembled physics package, with shielding removed. Reprinted with permission from J. F. DeNatale *et al.*, in *Proceeding of IEEE Position Location and Navigation Symposium (PLANS)* (2008), pp. 67–70. Copyright 2008 IEEE.

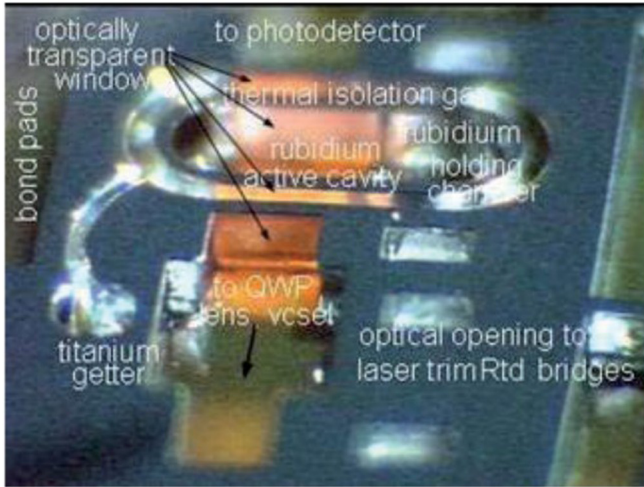
operation at a cell temperature approaching 100 °C when vacuum packaged. A physics package based on this design has demonstrated<sup>172</sup> a short-term fractional frequency instability of near  $2 \times 10^{-11}/\sqrt{\tau}$  while running on less than 10 mW at an ambient temperature of 25 °C. Similar thermal isolation solutions have been used in other designs to achieve comparably low power dissipation.<sup>173,174</sup> The CSAC design shown in Fig. 25 included several other novel features. The physics package was based on a folded optics geometry [see Fig. 25(a)], in which diverging light emitted by the laser passed through the cell was reflected off a mirror and passed back through the cell a second time before being detected with a photodetector in the same plane as the laser. This doubled the interaction length and increased the signal strength. A novel integrated laser/photodetector<sup>89</sup> was also developed for this design.

A second vertically integrated design is shown in Fig. 26. In this design, size is again reduced by allowing the laser beam to expand in a folded geometry. The laser is mounted such that it initially propagates away from the vapor cell. A dual focus optic combined with a mirror allows the transverse beam profile to expand such that it fills the vapor cell in a much smaller longitudinal distance that it would otherwise.

A physics package design that relies more heavily on advanced MEMS processing<sup>175</sup> is shown in Fig. 27. In this design, light from a VCSEL is redirected by a mirror etched in Si into the horizontal plane. The light then passes through



(a)



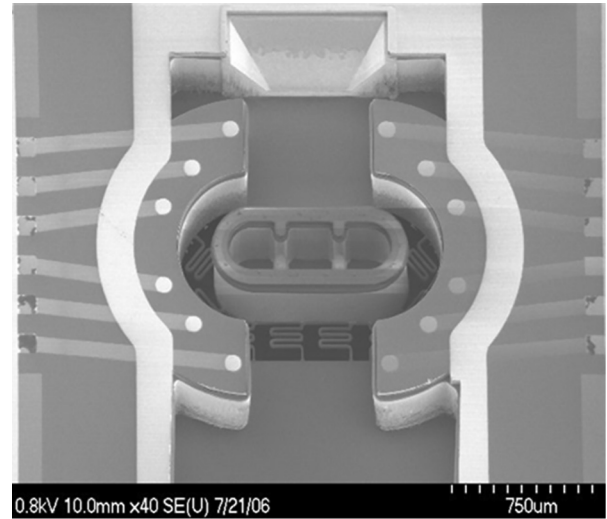
(b)

FIG. 27. Horizontally integrated design for a chip-scale atomic clock physics package. (a) Schematic of physics package and (b) photograph of vapor cell integrated into optical path. Reprinted with permission from D. W. Youngner *et al.*, in *Proceeding of IEEE Transducers* (2007), pp. 39–44. Copyright 2007 IEEE.

some optics and into a vapor cell suspended in vacuum by thin, thermally isolating bridges. The light is redirected toward the photodetector by a second angled mirror. The cell in this design is formed by deep reactive ion etching (DRIE) and is sealed after filling with a reflow solder. The advantage of this design is that essentially all components can be etched into only three wafers, which are then bonded together to assemble the physics package.

A second horizontally integrated design was proposed,<sup>176</sup> in which the top and bottom plates that confine the alkali metal in the cell are sealed by anodic bonding. This design uses conventional excitation of the atomic resonance by integrating a stripline waveguide onto the top of the cell assembly. A laser diode is proposed as the light source.

Thermal isolation in most chip-scale atomic devices is achieved by mounting the heated components in an evacuated package and suspending them on thin tethers, which limits the heat conduction to the package walls. The tethers have been fabricated from a polyimide,<sup>124</sup> shown in Fig. 25, or from glass, as shown in Fig. 28. The cells are heated with a current flowing in metallic traces patterned on the cell surface and the tethers. Heating can also be done by flowing current through etched, doped silicon, fabricated either as part of the cell<sup>177</sup> or mounted externally after cell fabrication.<sup>178</sup> In one considerably simpler design, shown in Fig. 29, a chip-scale physics package was mounted on a



87Rb cavity: front

FIG. 28. Alkali vapor cell suspended on glass tethers to thermally isolate the heated cell from the walls. Reprinted with permission from D. W. Youngner *et al.*, in *Proceeding of IEEE Transducers* (2007), pp. 39–44. Copyright 2007 IEEE.

polytetrafluoroethylene (PTFE) pillar for thermal isolation and packaged inside an evacuated container.<sup>179</sup> The physics package could be heated to 100 °C using 150 mW of electrical heating power.

#### D. Compact, low-power local oscillators

In a passive atomic frequency standard, the frequency stability of the local oscillator is important from several perspectives. First, the overall stability of the oscillator must be low enough that the servo system can lock the oscillator to the atomic transition. Sudden jumps in the (unlocked) oscillator frequency, for example, may be beyond the locking range of the servo loop and therefore bring the oscillator out of lock. Second, the phase noise of the oscillator at frequencies larger than the servo bandwidth must be consistent with the application for which the clock is intended. Finally, the phase noise of the oscillator at all even harmonics of the servo modulation frequency can create instability in the locked frequency over long integration times as a result of aliasing.<sup>180</sup> Usually, the noise at the second harmonic dominates, in which case, this last requirement can be simply stated for white frequency noise as

$$S_y(2f_m) < 4\tau\sigma_y(\tau)^2, \quad (20)$$

where  $S_y(2f_m)$  is the power spectral density of the fractional frequency fluctuations at twice the modulation frequency,  $\sigma_y(\tau)$  is the desired Allen deviation, and  $\tau$  is the integration time.

For chip-scale atomic clocks, the oscillator must satisfy several other conditions. First, it must be tunable to a subharmonic of the hyperfine frequency of the atom being interrogated. Usually the first subharmonic (4.596 GHz for <sup>133</sup>Cs and 3.405 GHz for <sup>87</sup>Rb) is a good compromise between convenience and performance. It must also be tunable with an

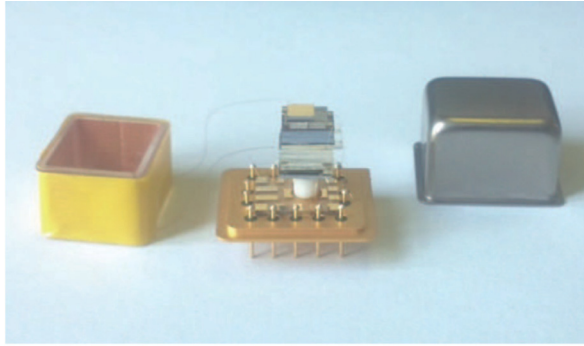


FIG. 29. Chip-scale atomic clock in which the physics package is mounted on a PTFE pillar for thermal isolation. Reprinted with permission from S. L. Li *et al.*, *Chin. Phys. B* **23**, 6 (2014). Copyright 2014 Institute of Physics, Chinese Academy of Sciences.

analog or digital control signal over a range large enough to compensate for all oscillator frequency variations caused by environment or aging. In addition, about 0.1 mW–1 mW of RF power is needed to drive the VCSEL and the oscillator must provide that or amplification must be used. Finally, most applications require a 5 MHz or 10 MHz clock output to interface with existing signal channels.

Traditionally, local oscillators for vapor cell atomic clocks have been based on a 5 MHz or 12.5 MHz quartz crystal oscillator, multiplied up to the alkali transition frequency (6.8 GHz) by a step recovery diode.<sup>17</sup> The oscillator is locked to the atomic resonance with a frequency-locked loop. However, step-recovery diodes require considerable input power to generate the high harmonics necessary to access the atomic resonance frequencies, making them largely impractical for low-power instruments.

Fractional-N dividers (or dual modulus prescalers) are a much lower-power alternative for bridging the frequency gap between the required 5 MHz output and the GHz-range atomic transition frequencies. With such a device, a high-frequency voltage-controlled oscillator (VCO) can be phase-locked to a 10 MHz quartz oscillator using only a few mW of power. Thus, fractional-N dividers have been widely used in chip-scale atomic clocks. The basic architecture of such a

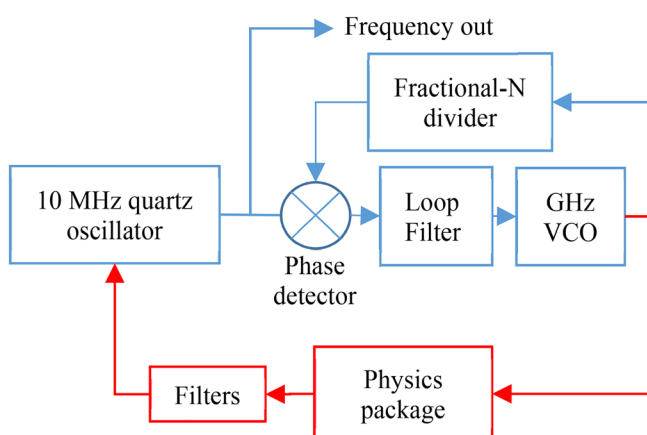


FIG. 30. Architecture of a phase-locked loop based on a fractional-N divider (in blue) and a frequency-locked loop that controls the oscillator frequency (in red).

phase-locking circuit, along with the frequency-locked loop that controls the oscillator frequency, is shown in Fig. 30.

Several types of novel oscillators were developed specifically for chip-scale atomic clocks. Coaxial waveguide resonators have been used,<sup>181,182</sup> with the gain provided by a bipolar junction transistor. The resonator had a small form factor (2 mm × 2 mm × 3.9 mm), low cost, moderately high Q-factor ( $\sim 100$ ), and a resonant frequency near 3.4 GHz. The oscillator produced 0.25 mW of RF power with only 2.1 mW of DC power at 1.2 V and the single sideband phase noise at 300 Hz was about  $-55$  dBc/Hz.

Oscillators based on thin-film bulk acoustic resonators (TFRs or FBARs)<sup>183,184</sup> were also developed. A Colpitts oscillator based on a TFR produced 0.25 mW of RF power at 4.6 GHz with 10 mW of DC power.<sup>185</sup> The phase noise at 300 Hz was  $-53$  dBc/Hz. A similar oscillator was developed by Yu *et al.* VCOs for chip-scale atomic clocks have been demonstrated using more conventional oscillator approaches,<sup>186</sup> but have yet to achieve low power operation.

In one novel low-power oscillator design,<sup>174</sup> a 569 MHz quartz crystal oscillator was used to directly injection lock a 3.4 GHz VCO. This eliminated the need for a phase-locked loop entirely, and the power required to run it. The phase noise at 3.4 GHz was measured to be  $-92$  dBc/Hz at 1 kHz offset and the oscillator required less than 7 mW to operate. However, the clock output frequency was 569 MHz and further division and corresponding power would be needed to reach a 5 MHz or 10 MHz output.

Application-specific integrated circuits (ASICs) have been developed to achieve good oscillator performance at even lower power. A PLL circuit was implemented<sup>187</sup> in 0.18  $\mu\text{m}$  CMOS and integrated on chip with a transimpedance amplifier and phase-sensitive detection element for the photodetector signal. This IC ran on 26 mW, including the RF power amplifier required to reach 1 mW of RF output power. The phase noise at 1 kHz offset was  $-86$  dBc/Hz at 3.4 GHz. When locked to an atomic physics package, this oscillator supported a short-term frequency stability of  $4 \times 10^{-10}/\sqrt{\tau}$ . An even lower power of 12 mW was achieved in another ASIC,<sup>188</sup> which also incorporated high-resolution frequency tuning of  $10^{-13}$ . The phase noise 1 kHz from the carrier was  $-83$  dBc/Hz and the active area of this chip was only 0.7 mm<sup>2</sup>. This chip supported a clock frequency stability of  $5 \times 10^{-11}$  at 1 s of integration. A schematic and photograph of this last chip is shown in Fig. 31.

## E. Control electronics

Electronics are required in any vapor cell atomic clock to power the entire instrument and implement several control loops that stabilize various instrument parameters. The primary control loop in a laser-pumped passive atomic standard is that which stabilizes the local oscillator frequency to the atomic microwave resonance. Since the quality of this control loop directly impacts the short- and long-term frequency stability of the frequency reference, it is the most critical element in the control system. Secondary control loops stabilize the temperature of the vapor cell and laser and lock the laser wavelength to the atomic optical transition.

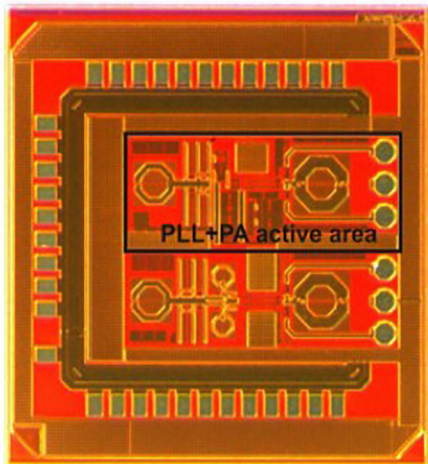
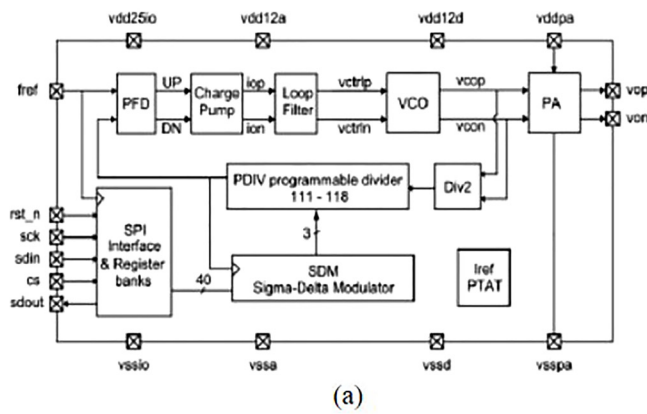


FIG. 31. Application-specific integrated circuit implementation of a local oscillator for a chip-scale atomic clock. (a) Chip architecture and (b) micrograph of chip. Reprinted with permission from Y. Z. Zhao *et al.*, IEEE Trans. Instrum. Meas. **64**, 263–270 (2015). Copyright 2015 IEEE.

As described above, the temperature of the vapor cell determines the signal size (via the alkali vapor density) and the magnitude of the alkali-buffer gas collision shift. The cell temperature is usually stabilized by monitoring the cell temperature with a temperature sensor (thermistor or Pt film) and then feeding an error signal generated from this measurement back into the cell heaters. Temperature stability of  $\sim 10$  mK is not difficult to achieve with this method.

The wavelength of the radiation emitted by the laser must also be tuned and locked to the optical resonance in the atoms in order to excite the CPT resonance. The wavelength of a VCSEL can be tuned by changing either the laser temperature or laser current. Thus, feedback to either temperature or current could be used to stabilize the laser wavelength. Usually, the laser temperature is measured with a temperature sensor located nearby and stabilized to a roughly constant value using a small heater. The laser current is then modulated at a frequency of a few kHz (thereby modulating the laser wavelength) and the photodetector signal demodulated synchronously to generate an error signal. This error signal is then used to adjust the laser current and stabilize the laser frequency to the peak of the optical absorption spectrum. This basic locking scheme, shown in Fig. 32(a), can be modified as described in detail below.

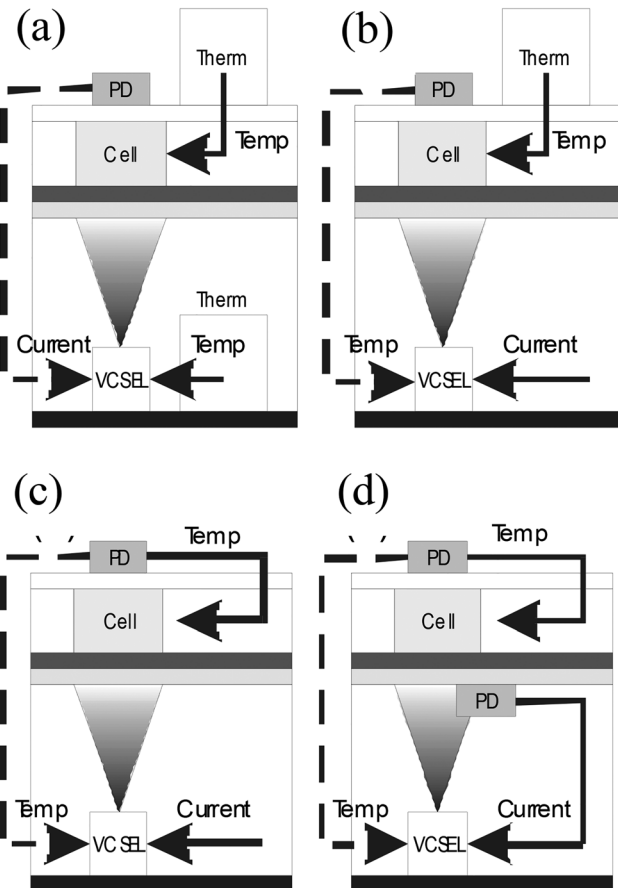


FIG. 32. Atom-based stabilization schemes. Reprinted with permission from V. Gerginov *et al.*, Opt. Lett. **31**, 1851 (2006). Copyright 2006 The Optical Society of America. (a) Conventional stabilization, in which the laser and cell temperatures are stabilized with thermistors, and the laser wavelength is stabilized using feedback to the laser injection current from the atomic absorption resonance. (b) The laser current is driven with a constant current source and the laser wavelength is stabilized with feedback from the atomic absorption resonance. (c) The cell temperature is now also stabilized with feedback from the atomic absorption resonance. (d) A photodiode before the cell monitors the output power of the laser.

There are also several tertiary control functions that can be implemented and that generally lead to improved long-term frequency stability. These include active stabilization of the laser output power, the RF power going into the laser, and the DC magnetic field applied to the vapor cell. Control systems for early atomic frequency references were implemented using analog electronic circuits. The recent development of low-power microprocessors and field programmable gate arrays (FPGAs) have allowed the control systems to be implemented instead as firmware with only a modest analog interface circuit.<sup>189–191</sup> This type of implementation not only reduces power consumption but also allows considerably more functionality to be included with only minor design changes to the hardware. Microprocessor-based control circuits have been demonstrated that run on less than 30 mW of electrical power, including power regulation.<sup>191</sup>

A control system was also developed at CSEM based on application-specific integrated circuit.<sup>187</sup> Like the design above, it was based on a low-power VCO phase-locked to a lower-frequency VCXO using a fractional-N divider. This chip ran on only 24 mW of electrical power, with the main sources of power consumption being the VCO and the output amplifier.

This chip successfully controlled a clock based on a glass vapor cell to a short-term stability<sup>192</sup> of  $4 \times 10^{-10}/\sqrt{\tau}$ .

The basic control architecture described above suffers from some minor limitations that result in long-term instability of the output frequency. One class of limitations involves temperature gradients between the cell and laser and their respective temperature sensors. Although the temperature sensors are typically located as close as possible to the element to be controlled, some spatial separation is unavoidable, which results in a finite thermal resistance between them. Even if the sensor temperature is perfectly stabilized, temperature fluctuations of the cell and laser can therefore still be present.

As mentioned above, temperature fluctuations of the laser cause changes in the laser output wavelength. The disadvantage of the basic scheme shown in Fig. 32(a) is that as the laser current is adjusted to maintain a constant wavelength under changing temperature conditions, the optical power also changes. Changes in optical power result in changes in the AC Stark shift and cause secondary fluctuations in the clock output frequency. An alternative, shown schematically in Fig. 32(b), is to drive the laser current with a constant current source and feed the laser wavelength error signal back into the laser heater, thereby eliminating the need for a thermistor near the laser.<sup>193</sup> The laser temperature is therefore stabilized directly using the parameter of interest (the wavelength), rather than indirectly using a thermistor.

The temperature of the cell can be controlled using a similar modification, in which the DC absorption of the alkali atoms is used as a measure of the cell temperature. Since the alkali vapor pressure depends strongly on temperature (factor of ten change in density for every  $\sim 30$  K change in temperature), the optical absorption of the light by the atoms changes by about 1%/K. The DC signal from the photodiode after the cell can therefore be compared to a predetermined voltage and the difference signal sent back to the cell heater [see Fig. 32(c)]. This again eliminates the need for a thermistor to monitor the cell temperature, which is instead stabilized based on the parameter of interest, the alkali density. A final possible control element is to monitor the light power level before the cell and feed an error signal based on this back to the laser current, as shown in Fig. 32(d). This control loop will correct for long-term changes in the laser intensity at constant temperature caused, for example, by laser aging.

A more sophisticated way of controlling the AC Stark shift is to use the fact that the sign of the shift depends on whether the wavelength of the excitation field is tuned above or below the optical resonance. The output of the modulated laser used in most CPT clocks generally has a spectrum of optical lines spaced by the modulation frequency and the spectral distribution can be controlled by adjusting the modulation index. In some cases, there exists a specific modulation index for which the spectral distribution is such that the light shift vanishes.<sup>194</sup> The operation of the clock at this modulation index results in reduced frequency instability due to power variations of the laser. The light shift can also be monitored continuously<sup>195</sup> by a modulation of the optical power transmitted through the cell accomplished with a

variable attenuator. The error signal is used to control the RF power that modulates the laser and stabilize it to the level at which the light shift is zero. This control loop is useful if, over time, the RF power or input impedance of the laser drifts causing a corresponding drift in the light modulation index. The RF power that modulates the laser can also be controlled through a variable RF attenuator placed between the local oscillator and the laser. The attenuation is modulated and the DC attenuation level set such that the effect of the modulation on the optical power transmitted through the cell is minimized.<sup>172</sup>

## F. CSAC prototypes

Fully integrated chip-scale atomic clocks, in which the physics package, local oscillator, and compact control electronics were assembled together in a single package, have been demonstrated by several groups to date.<sup>173,174,191</sup> Photographs of these clocks are shown in Fig. 33. One clock,<sup>172</sup> shown in Fig. 33(b), had a total volume of  $15 \text{ cm}^3$ , ran on 125 mW of power, and had a precisely calibrated output frequency of 10.0 MHz. The power budget is shown in Table II. This clock incorporated four main servo loops. The microwave frequency was stabilized to the CPT resonance by modulating the VCO frequency via the PLL and using lock-in detection; the laser frequency was stabilized to the optical transition in the atoms in a similar manner; the physics package temperature was stabilized by monitoring the DC optical power transmitted through the cell and comparing it to a setpoint voltage; and the RF power going into the VCSEL was stabilized by modulating this quantity using a microwave attenuator and setting the attenuator level such that the resulting modulation of transmitted optical power was a minimum. Ten of these units were fabricated and all had short-term instabilities at 1 s of integration under  $3 \times 10^{-10}$ . Aging below  $3 \times 10^{-12}/\text{day}$  (after burn-in) and retrace of about  $1 \times 10^{-10}$  was demonstrated. The long-term instability of this clock was below  $10^{-11}$  at 1 day. The short- and long-term stabilities of this clock are shown in Fig. 34.

A second clock, shown in Fig. 33(c), with a total volume of  $1.7 \text{ cm}^3$  and running on 57 mW of power, demonstrated similar stability levels.

Even smaller, lower-power instruments have been developed, although these contain design changes that make them difficult to use. The clock shown in Fig. 35(a), with a volume of only  $1 \text{ cm}^3$  and running on under 30 mW of power had an instability below  $10^{-11}$  at 1 h of integration.<sup>174</sup> To reach the low power consumption, the frequency synthesizer and 10 MHz quartz crystal oscillator were replaced with a 4.6 GHz VCO based on a thin film resonator. As a result, this clock had an output frequency of 4.6 GHz, making it difficult to use in most applications, which require a 10 MHz signal. This clock also did not have power conditioning or magnetic shielding. A second  $1 \text{ cm}^3$ , 30 mW clock,<sup>161</sup> shown in Fig. 35(b), achieved equivalent performance using direct injection locking of a 3.4 GHz oscillator with a 569 MHz voltage controlled crystal oscillator. This oscillator configuration consumed under 7 mW of power and the rest of the control electronics was brought below 9 mW by adjusting the

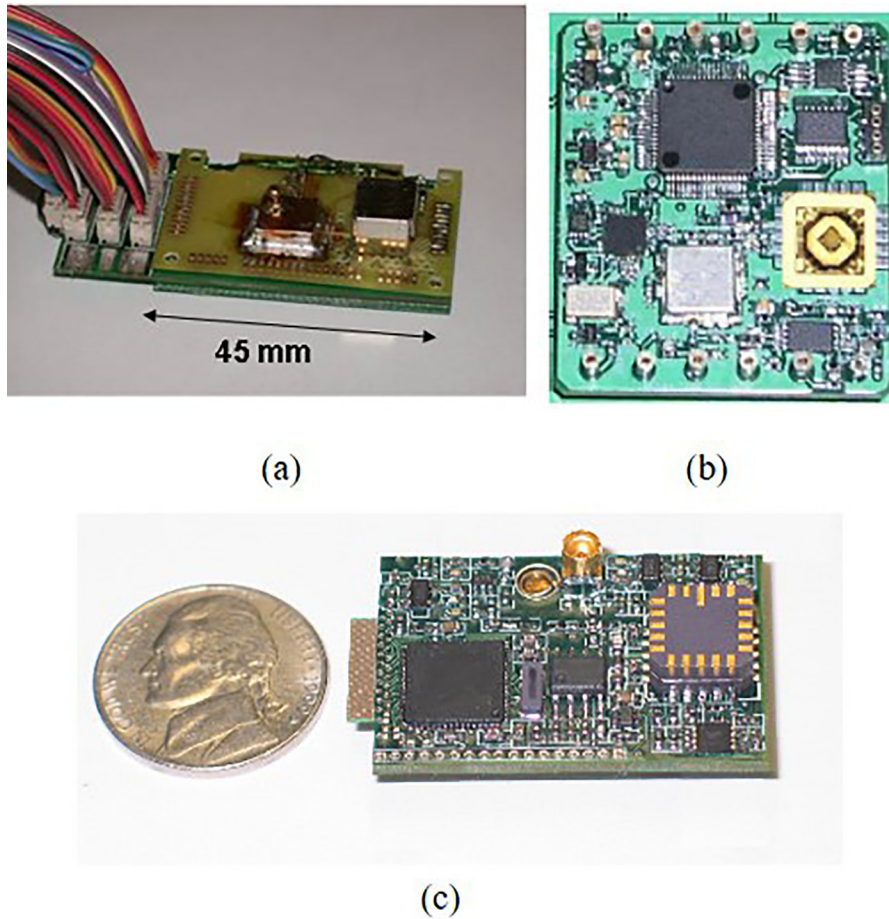


FIG. 33. Photographs of three fully integrated chip-scale atomic clocks. (a) A fully integrated chip-scale atomic clock built at NIST in 2006. (b) Chip-scale atomic clock prototype. Reprinted with permission from R. Lutwak *et al.*, in *Proceedings of IEEE International Frequency Control Symposiums and European Frequency and Time Forum* (2007), pp. 1327-1333. Copyright 2007 IEEE. (c) Chip-scale atomic clock prototype. Reprinted with permission from D. W. Youngner *et al.*, in *Proceeding of IEEE Transducers* (2007), pp. 39-44. Copyright 2007 IEEE.

TABLE II. Power budget for the clock shown in Fig. 33(b). Reprinted with permission from R. Lutwak *et al.*, in *Proceeding of Precise Time and Time Interval (PTTI) Meeting* (2007), pp. 269-290.

System	Component	Power (mW)
Signal processing	MicroController	20
	16-Bit DACs	13
	Analog	8
Physics	Heater power	7
	VCSEL power	3
	C-Field	1
Microwave/RF	4.6 GHz VCO	32
	PLL	20
	10 MHz TCXO	7
	Output buffer	1
Power regulation and passive losses		13
Total		125

control system clock speed. The physics package of this clock consumed under 15 mW, with most of the power used for heating the vapor cell.

### G. Performance and impact

Commercial chip-scale atomic clocks achieve quite significant advances in miniaturization and power consumption as compared with previous vapor cell clocks. The power consumption of a variety of commercial vapor cell atomic clocks as a function of the year they were released is shown in Fig. 36. Between 1970 and 2010, the power consumption of such clocks was reduced from about 40 W to 5 W. The commercial chip-scale atomic clock,<sup>196</sup> released in 2011 runs on only 120 mW, achieving a power consumption 30× lower than any previous vapor cell clock. As described above, this improvement is the result of two main design changes: the use of a vertical cavity surface-emitting laser as the light source and the use of a thermally isolated microfabricated alkali vapor cell that can be heated to its operating temperature with only 10 mW of power. The low power consumption of the instrument allows it to operate on battery power. The energy density of lithium ion batteries at present is roughly 500 W-h/l. A chip-scale atomic clock could therefore run on a battery of volume 10 cm<sup>3</sup> for almost 2 days.

The fractional frequency stability as a function of integration time for a commercial chip-scale atomic clock<sup>196</sup> is compared to other commercial atomic clocks in Fig. 37.

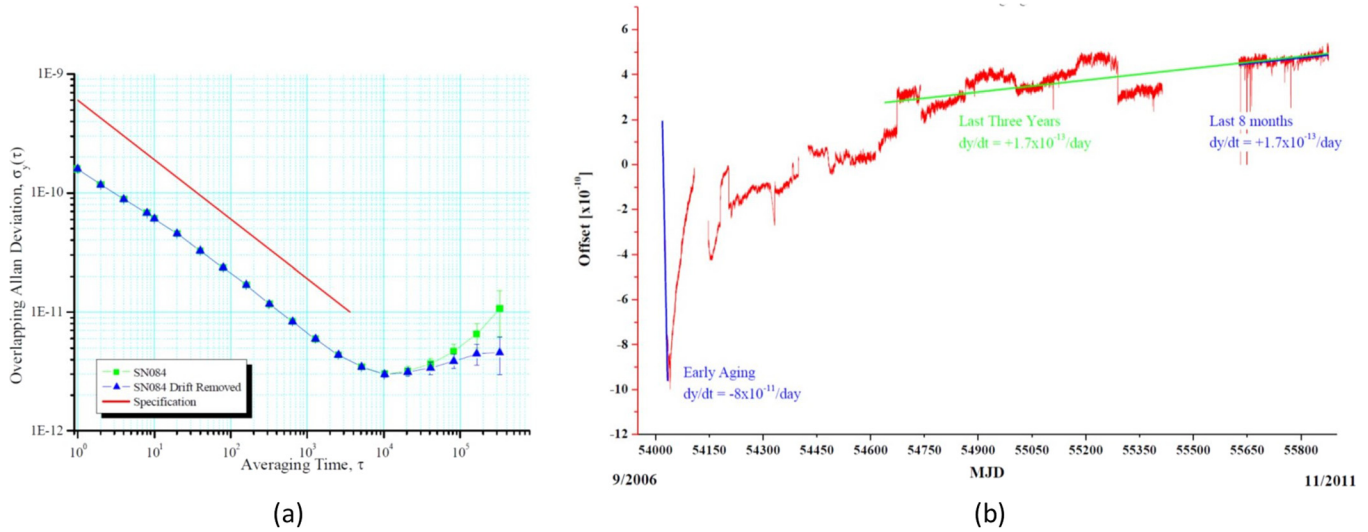


FIG. 34. (a) Short-term frequency stability and (b) long term drift of the clock shown in Fig. 33(b). Reprinted with permission from R. Lutwak *et al.*, in *Proceedings of IEEE International Frequency Control Symposiums and Proceeding of European Frequency and Time Forum* (2007), pp. 1327–1333. Copyright 2007 IEEE and from R. Lutwak, *Proc. Precise Time and Time Interval (PTTI) Meeting*, pp. 207–220 (2011).

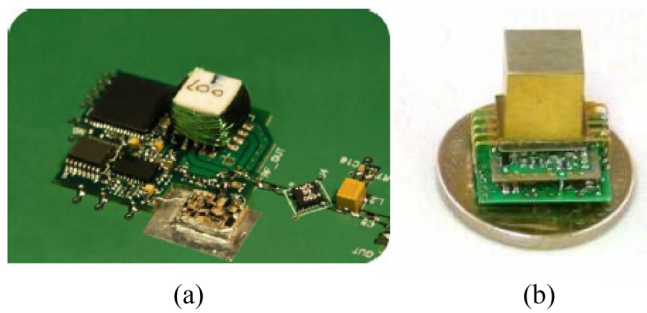


FIG. 35. Chip-scale atomic clocks with a volume below  $1 \text{ cm}^3$  and a power dissipation below 30 mW. (a) Reprinted with permission from R. Lutwak *et al.*, in *Proceeding of Precise Time and Time Interval (PTTI) Meeting* (2007), pp. 269–290. (b) Reprinted with permission from J. F. DeNatale *et al.*, in *Proceeding of IEEE Position Location and Navigation Symposium (PLANS)* (2008), pp. 67–70. Copyright 2008 IEEE.

Chip-scale atomic clocks have a short- and long-term frequency stability about one order of magnitude worse than other, larger vapor cell atomic clocks. However, the long-term stability at 1 day and beyond is over two orders of magnitude better than a low-power oven controlled quartz oscillator, running on comparable power.

The frequency stability shown in Fig. 37 can be combined with the environmental sensitivities to establish an overall timing error. This is shown in Fig. 38. A chip-scale clock can hold  $1 \mu\text{s}$  for about 1000 s and 1 ms for about 1 week. The timing error over 1 day is roughly  $100 \mu\text{s}$ .

There is an important expected trade-off between the size and power consumption of an instrument and its performance. This can ultimately be traced back to the transition linewidth and relaxation due to interactions with the environment. As the instrument dimensions become smaller, the interrogation time over which the atoms can be measured becomes smaller. The

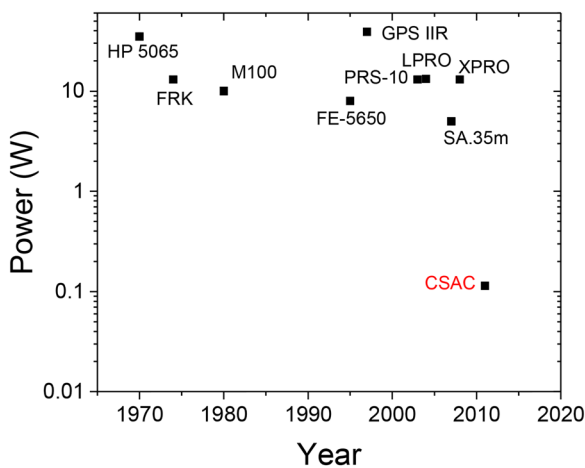


FIG. 36. Power consumption for a variety of commercial vapor cell atomic clocks as a function of their release year.

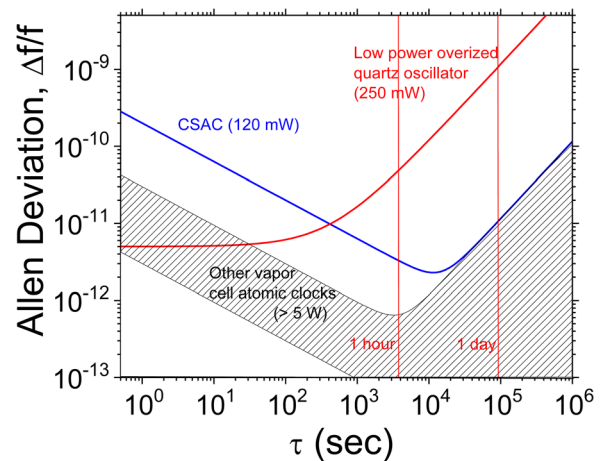


FIG. 37. Fractional frequency instability of a chip-scale atomic clock compared to other frequency references. Blue solid line: Commercial chip-scale atomic clock; red solid line: commercial low-power oven-controlled crystal oscillator (250 mW); hatched region: other compact commercial vapor cell atomic clocks developed for telecommunications applications.

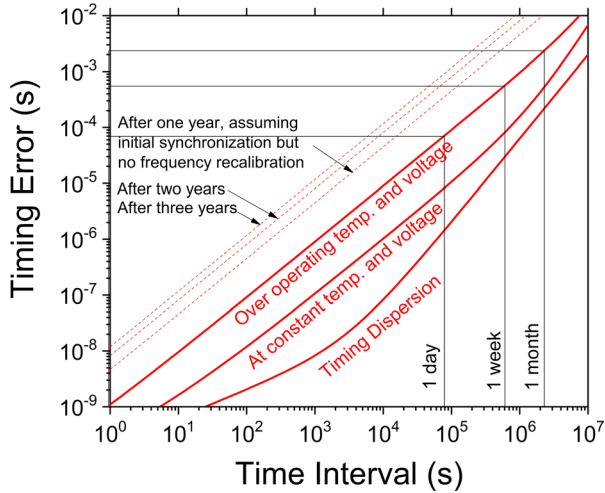


FIG. 38. Timing error for a commercial chip-scale atomic clock as a function of time interval being measured. Projections are made under a variety of environmental conditions. If calibrated, a CSAC can maintain about 100  $\mu$ s over 1 day.

timing error of several types of commercial frequency references over a broad range of technology approaches is shown in Fig. 39. It is interesting to note that many references lie on a monotonic curve, while microcontroller quartz crystal oscillators and chip-scale atomic clocks lie somewhat off the curve.

In Table III, the instrument size, power consumption, and performance are listed for four types of microwave atomic frequency references. As the size, power consumption, and cost drop, so does the frequency stability, retrace, and accuracy.

**H. Applications**

It has long been realized that the good medium-term and long-term stability of atomic clocks can be of value for satellite-based navigation if such a clock could serve as the time base for the global navigation satellite system (GNSS)

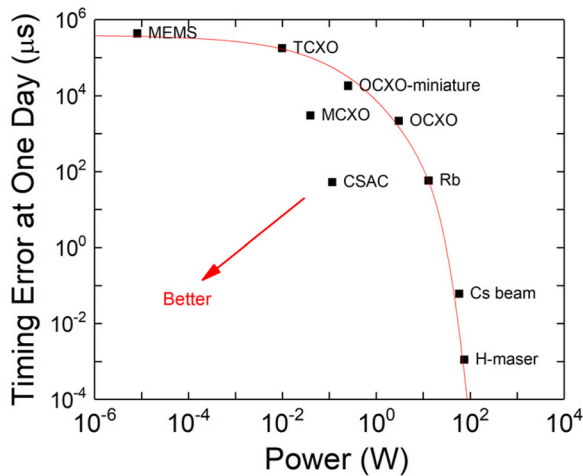


FIG. 39. Timing error at 1 day as a function of power consumption for a variety of commercial frequency references. Adapted from an original figure by R. M. Garvey. MEMS: silicon micromachined mechanical; TCXO: temperature compensated crystal oscillator; OCXO: oven-controlled crystal oscillator; MCXO: microprocessor-controlled crystal oscillator; Rb: vapor cell rubidium standard; Cs beam: cesium beam clock; H-maser: hydrogen maser; and CSAC: chip-scale atomic clock.

TABLE III. Comparison of performance of several commercial frequency references.

	Hydrogen maser	Beam clock	Telecom-grade vapor cell clock	CSAC
Volume [cm <sup>3</sup> ]	$4 \times 10^5$	30 000	124	16
Power [W]	75	50	15	0.12
Stability at 1 s.	$2 \times 10^{-13}$	$1.2 \times 10^{-11}$	$3 \times 10^{-11}$	$3 \times 10^{-10}$
Drift [/day]	$2 \times 10^{-16}$	$3 \times 10^{-14}$	$10^{-11}$	$1 \times 10^{-11}$
Drift [/mo.]	$3 \times 10^{-15}$		$5 \times 10^{-11}$	$3 \times 10^{-10}$
Retrace	$10^{-13}$	$10^{-13}$	$2 \times 10^{-11}$	$5 \times 10^{-11}$
Frequency uncertainty after 5 years		$10^{-12}$	$>10^{-9}$	$>10^{-9}$

receiver.<sup>162–164</sup> One area in which the performance can be improved for a military GNSS receiver is in the sensitivity to jamming. Since the military P(Y) code is encoded at a higher frequency than the civilian (C/A) code, 10 MHz chipping rate for the former compared to 1 MHz for the latter, the military code is more difficult to jam. However, the military code is a pseudo-random code that repeats itself only every week. Thus, to acquire the military code via a cross-correlation measurement without some knowledge of the time requires considerable computing power: the correlator must search through  $> 10^{12}$  bit sequences as illustrated schematically in Fig. 40. Most military GNSS receivers therefore first acquire the civilian code (which repeats itself every millisecond and hence is very easy to acquire), establish the time from this process, and then use this knowledge of the time to narrow the search window for the military code. Fruehauf *et al.*<sup>164</sup> found that roughly 1 ms timing accuracy is required for fast direct acquisition of the P(Y) code. Because of its better medium and long-term frequency stability, an atomic clock can maintain this 1 ms requirement for several days after synchronization considerably longer than can the quartz oscillator usually found in GPS receivers.

Commercial chip-scale atomic clocks have been shown experimentally to operate successfully as the time base of a GPS receiver.<sup>197</sup> In addition, a time base with good medium-term and long-term stability can help considerably in satellite navigation where only two or three satellites are visible,<sup>198</sup> for example, in urban canyons. Four or more satellites are

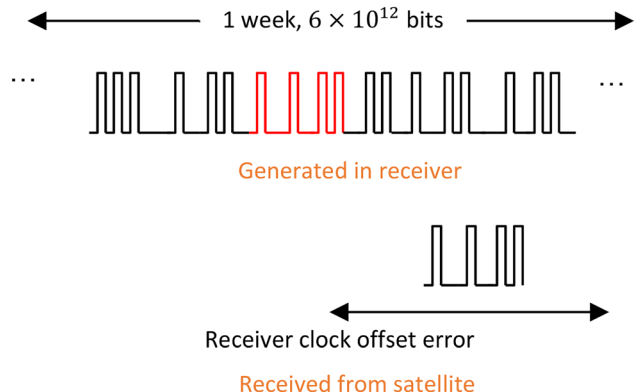


FIG. 40. Illustration of how the acquisition time for the military P(Y) code depends on the receiver clock offset. The larger the clock offset uncertainty, the more correlations need to be calculated to lock on to the signal.

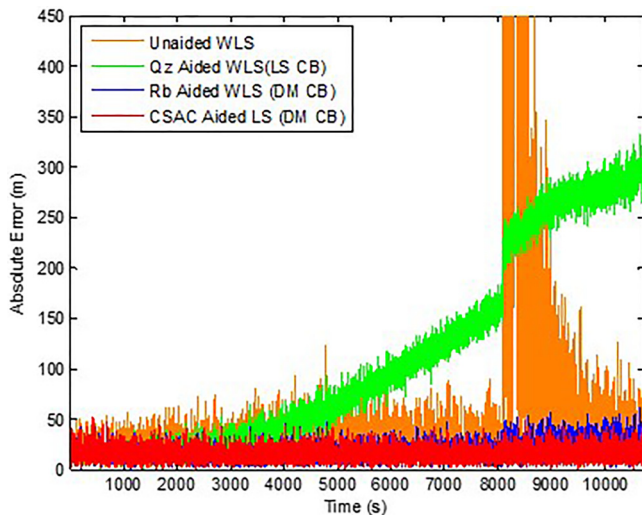


FIG. 41. Calculated positioning error for four time bases. Reprinted with permission from R. Ramlall *et al.*, in *Proceeding of International Technical Meeting of the Satellite Division of the Institute of Navigation* (2011), pp. 2937-2945.

usually needed for a complete navigation solution ( $x, y, z, t$ ) when the receiver time is unknown. A receiver time base with a sufficiently low instability can therefore reduce the required number of satellites to three. Ramlall *et al.*<sup>199</sup> simulated the use of a CSAC for this application and found that the absolute position error after 3 h of navigation using only two satellites could be improved from  $\sim 300$  m for a quartz oscillator time base to less than 50 m for a CSAC time base, as shown in Fig. 41. Improvements in the vertical and horizontal dilution of precision were also found. Similar results were presented in other work.<sup>200</sup>

Precise timing at low power consumption is also of value for seismic measurements on the ocean floor related to earthquake detection, acoustic sensing, and oil exploration. Gardner *et al.*<sup>201</sup> describe the deployment of 13 commercial chip-scale atomic clocks for 6 months in ocean-bottom seismographs for microearthquake monitoring, for which timing accuracies of  $\sim 1$  ms are required. They reported that under these conditions, most of the CSACs operated as expected, with one showing evidence of a leak in the physical package vacuum packaging and two others showing higher than expected drift.

Chip-scale atomic clocks are also being developed for use in low-earth orbit space applications. With appropriate packaging, commercial chip-scale clock physics packages have been able to withstand ionizing radiation doses of up to<sup>202</sup> 43 krad (Si) TID, although the TCXO failed considerably below that. This dose is approximately equal to that accumulated over 1 yr in low-earth orbit. Chip-scale atomic clocks were also flown on the international space station<sup>203</sup> in 2011 but failed to operate.

## IV. CHIP-SCALE ATOMIC MAGNETOMETERS

### A. Device design, fabrication, and performance

The similarities in both underlying physics and instrument design between atomic clocks and atomic

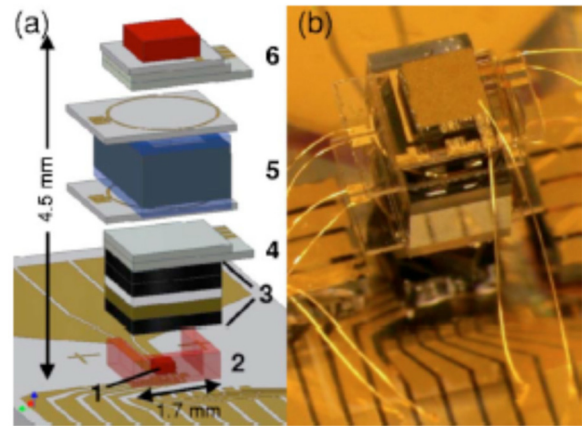


FIG. 42. A chip-scale Mx atomic magnetometer. The coils used to drive the Larmor precession are shown. Reprinted with permission from Appl. Phys. Lett. 90, 081102 (2007). Copyright 2007 AIP Publishing LLC.

magnetometers (see Figs. 3 and 5) generally allow advances in one area to be transferred and applied to the other quite easily. Miniaturization of these instruments is no exception; very soon after the first chip-scale atomic clock was developed,<sup>160</sup> a chip-scale atomic magnetometer was also demonstrated.<sup>204</sup> This magnetometer was based on CPT spectroscopy of magnetically sensitive transitions in alkali atoms between levels with  $m_F \neq 0$  and hence operation could be achieved simply by detuning the frequency of the local oscillator from the clock transition by an amount roughly equal to the Larmor frequency. It achieved a sensitivity of  $50 \text{ pT}/\sqrt{\text{Hz}}$  at 10 Hz and a bandwidth of approximately 100 Hz, as shown in Fig. 43, Trace A.

A more conventional Mx magnetometer (see Fig. 5) based on microfabricated alkali vapor cells<sup>205</sup> is shown in Fig. 42. This magnetometer incorporated a pair of lithographically defined coils placed on either side of the vapor cell. An oscillating current through the coils created a time-varying magnetic field, which drove the atomic spin precession. To avoid magnetic fields from the  $\sim 10$  mA current needed to heat the cell, the ITO heaters used to heat the cell

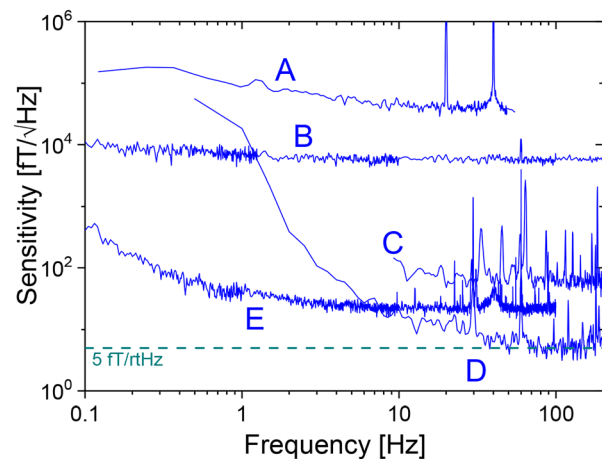


FIG. 43. Magnetic sensitivity of chip-scale atomic magnetometers. A: CPT magnetometer;<sup>204</sup> B: Mx magnetometer,<sup>205</sup> see Fig. 42; C: Single-beam SERF magnetometer,<sup>206</sup> D: best sensitivity achieved in a micromachined vapor cell;<sup>207</sup> and E: Fiber-optically coupled SERF magnetometer.<sup>210</sup>

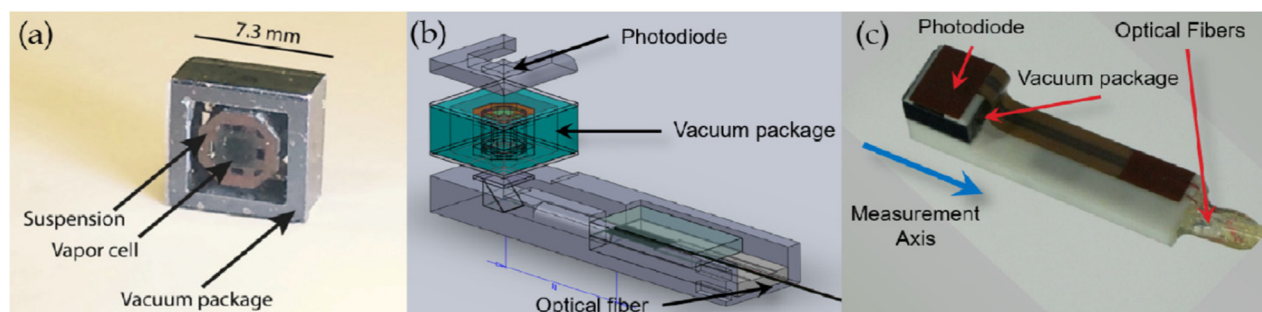


FIG. 44. A fiber-optically coupled chip-scale atomic magnetometer. (a) The vacuum assembly housing the vapor cell. (b) A schematic of the optical bench. (c) A photograph of the final package. Reprinted with permission from O. Alem *et al.*, *Opt. Express* **25**, 7849–7858 (2017). Copyright 2017 the Optical Society of America.

were laser-patterned and two layers of current were used such that the current path doubled back on itself in two different ways. An AC current was also used to move the heating current frequency outside the sensitive range of the magnetometer. This device achieved a sensitivity of  $5 \text{ pT}/\sqrt{\text{Hz}}$  throughout most of the band from 1 Hz to 100 Hz, as shown in Fig. 43, Trace B.

Zero-field chip-scale magnetometers have also been developed that take advantage of the suppression of spin-exchange collisions at high alkali densities, as described in Sec. ID above. A considerable enhancement of the sensitivity is achieved through the combination of larger signal and reduced transition linewidth afforded by the zero-field technique. While most SERF magnetometers use two orthogonally propagating beams to pump and probe the atoms, it is also possible to use a single laser beam to do both functions. Initial results in table-top experiments using microfabricated vapor cells showed a field sensitivity of  $70 \text{ fT}/\sqrt{\text{Hz}}$  in this single beam mode,<sup>206</sup> which was improved to  $5 \text{ fT}/\sqrt{\text{Hz}}$  with separate pump and probe beams.<sup>207</sup> At this level of sensitivity, the thermal noise of electrons in electrical conducting elements near the atomic vapor can be an important contribution to the overall field noise.<sup>208</sup> Flux concentrators can also be used around the cell to increase the signal at the cost of increased temperature sensitivity and increased noise at low frequencies due to thermal magnetization noise.<sup>209</sup>

Light narrowing was demonstrated in a magnetometer based on a microfabricated Rb vapor cell.<sup>211</sup> Considerably more laser power was required to achieve the high atomic polarization needed for light narrowing but the sensitivity was improved from  $1.5 \text{ pT}/\sqrt{\text{Hz}}$  without light narrowing to  $42 \text{ fT}/\sqrt{\text{Hz}}$ . This sensitivity was achieved at a field of  $5 \mu\text{T}$  showing that femtoTesla sensitivity can be achieved in a microfabricated vapor cell in a high-field environment.

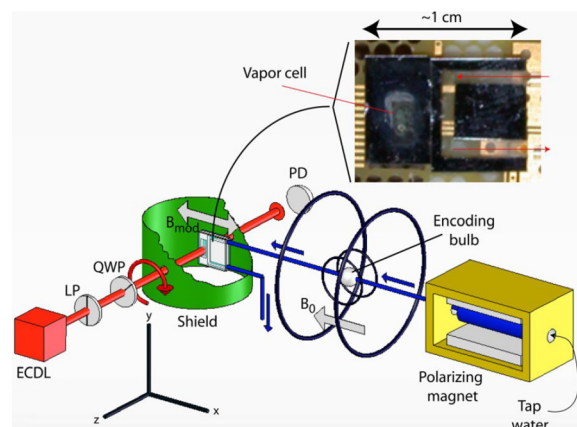
Implementing two orthogonally propagating optical fields can improve significantly the noise performance, but this optical configuration is challenging in a conventional micromachined alkali vapor cell because only two sides of the cell have transparent windows. As described above, there are several fabrication methods developed to enable the generation of orthogonally propagating fields. However, most chip-scale atomic magnetometers still use a single laser beam. In one novel magnetometer design,<sup>212</sup> non-colinear light propagation vectors were achieved using the natural

diffractive beam divergence of a laser output. In this design, spins precessing about the nominal optical axis created differential absorption in different parts of the beam. By using a quadrant detector to detect the light, some common-mode noise sources, such as laser intensity noise, could be suppressed. A simple 3-axis magnetometer was also demonstrated using microfabricated hemispherical bubble cells,<sup>146</sup> although no sensitivity measurements were reported.

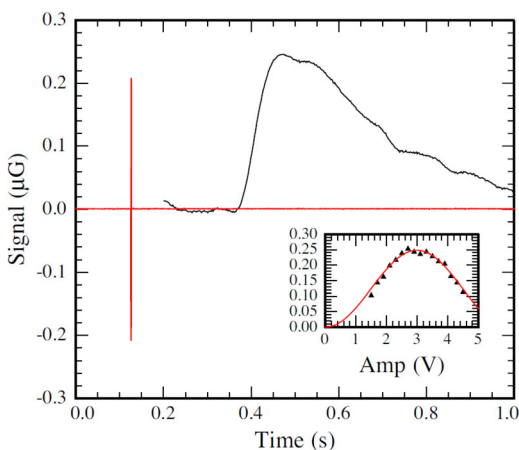
For magnetometers with a sensitivity in the fT range, one concern is the proximity of the electrically active elements, such as resistive cell heaters and the injection current of the laser, to the vapor cell. Such elements can generate magnetic fields that can interfere with, or simply add to, the fields to be measured. It can therefore be advantageous to situate the vapor cell away from the laser and other electronics and couple the light with the cell using fiber optics<sup>213</sup> or even over free space.<sup>214</sup> Drive coils can also be avoided by exciting the spin precession with an optical field modulated at the Larmor frequency.<sup>215</sup> Similar sensitivities can be achieved with this method, as compared to conventional coil-based excitation.<sup>216</sup>

Fiber-optically coupled chip-scale atomic magnetometers have been developed,<sup>210,217–220</sup> which incorporated a novel method for heating the vapor cell. The cell was mounted into a thermally isolated package and small pieces of colored glass were glued to each of the cell windows. The glass was chosen to be transparent at the probe laser wavelength (795 nm) but absorbing at a different wavelength (typically  $1.5 \mu\text{m}$ ). Light from a heating laser at this latter wavelength was then transmitted to the vapor cell running alongside the probe fiber and was absorbed by the colored glass, thereby heating the cell. Magnetometers based on this technique have achieved a sensitivity below  $20 \text{ fT}/\sqrt{\text{Hz}}$  at frequencies above 15 Hz and can run on 150 mW of optical power.<sup>210</sup>

Advances in sensor design and engineering now make it possible to fabricate moderate numbers of chip-scale magnetic sensors with a high degree of uniformity from sensor to sensor in terms of operating power and sensitivity.<sup>221,222</sup> An example of such a sensor is shown in Fig. 44. In all, 33 of these sensors were fabricated, with 30 of these operating with a power consumption below 100 mW and 26 having sensitivities under  $30 \text{ fT}/\sqrt{\text{Hz}}$ . Simple localization of a magnetic dipole was demonstrated by mounting the sensors on a spherical support structure 20 cm in diameter.<sup>221</sup>



(a)



(b)

FIG. 45. Chip-scale detection of nuclear polarization of water with a microfabricated alkali vapor cell used as a magnetometer. (a) Experimental setup, in which tap water is sent through a polarizing magnet and into a microfluidic channel positioned near the vapor cell. (b) Change in magnetic field observed when the water magnetization is reoriented using the encoding bulb shown in (a). Reprinted with permission from M. P. Ledbetter *et al.*, Proc. Natl. Acad. Sci. U. S. A. **105**, 2286–2290 (2008). Copyright 2008 National Academy of Sciences.

A very simple packaging approach based on precisely placing components into etched silicon wafers was developed<sup>223</sup> and an Mz magnetometer was demonstrated with this approach.

## B. Chip-scale nuclear magnetic resonance

The generation of electronic or nuclear spin polarized samples in microfabricated alkali vapor cells also has application to problems in nuclear magnetic resonance. Unlike the pickup coils usually used for detecting NMR signals, atomic magnetometers are sensitive at DC, making them particularly well-suited for detecting NMR signals at low magnetic fields. It is possible, for example, to detect the DC magnetic field produced by a polarized water sample with a magnetometer based on a microfabricated alkali vapor cell coupled to a microfluidic channel through which the water flows.<sup>224</sup> Such an experiment is shown in Fig. 45(a), with the magnetic signal produced by the polarized water shown in

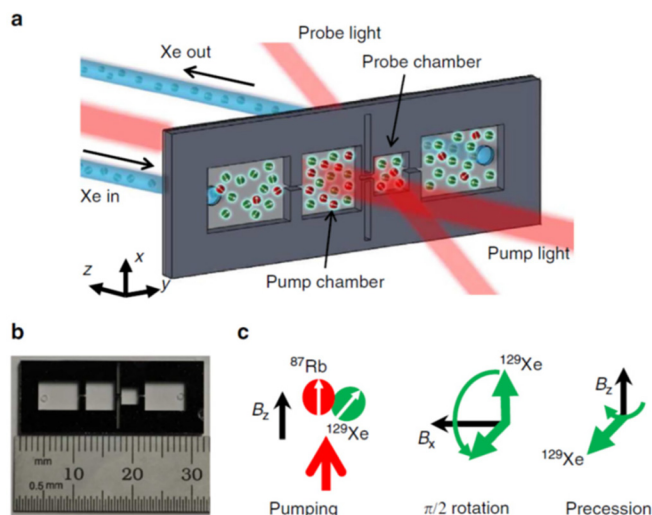


FIG. 46. A chip-scale source of hyperpolarized Xe atoms, based on micro-machined silicon and a fabrication method similar to the MEMS vapor cells described above. Xe gas enters the chip from a tube connected to one chamber, flows through a small micromachined channel into the pump chamber, in which it is optically pumped via spin-exchange collisions with a polarized Rb vapor. The polarized Xe then flows into a probe chamber, where the magnetization is measured with an *in-situ* Rb magnetometer. Reprinted with permission from R. Jiménez-Martínez *et al.*, Nat. Commun. **5**, 3908 (2014). Copyright 2014 Nature Publishing Group.

Fig. 45(b). This may be useful for remote detection of NMR signals.<sup>225–227</sup>

This type of chip-based detection can also be useful for magnetic resonance experiments. At low magnetic fields, chemical shifts are typically too small to be observed, but J-coupling resonances<sup>228</sup> can exist in heteronuclear molecules, and are typically at frequencies within the bandwidth of chip-scale atomic magnetometers. These can be detected, potentially on-chip, and can give information about molecular structure in a manner similar to the chemical shift.<sup>229,230</sup>

The ability to detect NMR signals at low frequencies removes the need for high-field magnets to produce the high resonance frequencies required for coil-based detection. However, most NMR experiments and instruments still require a high field for the initial polarization of the nuclei. Spin-exchange optical pumping<sup>61</sup> can circumvent this difficulty, since the nuclear spins are polarized through collisions with polarized electrons in alkali atoms. A chip-scale source of hyperpolarized Xe atoms<sup>231</sup> is shown in Fig. 46. With this  $\sim 1 \text{ cm} \times 2 \text{ cm}$  chip, a Xe polarization fraction of 0.5% was demonstrated at flow rates of  $5 \mu\text{l/s}$ . Subsequent improvements in the device such as over-pressuring the input channel have led to improvements such as polarization fractions of 7% and a device lifetime of over 2 weeks.<sup>232</sup> This latter device had a spin transfer efficiency of 0.005 and a production rate of  $3 \text{ ml/h/W}$  at an optical power of 10 mW.

## C. Biomagnetics with chip-scale atomic magnetometers

With the advances in sensitivity for atomic magnetometers made over the last 20 years, it has become possible to measure magnetic fields emanating from biological sources with these instruments. The human heart and brain produce

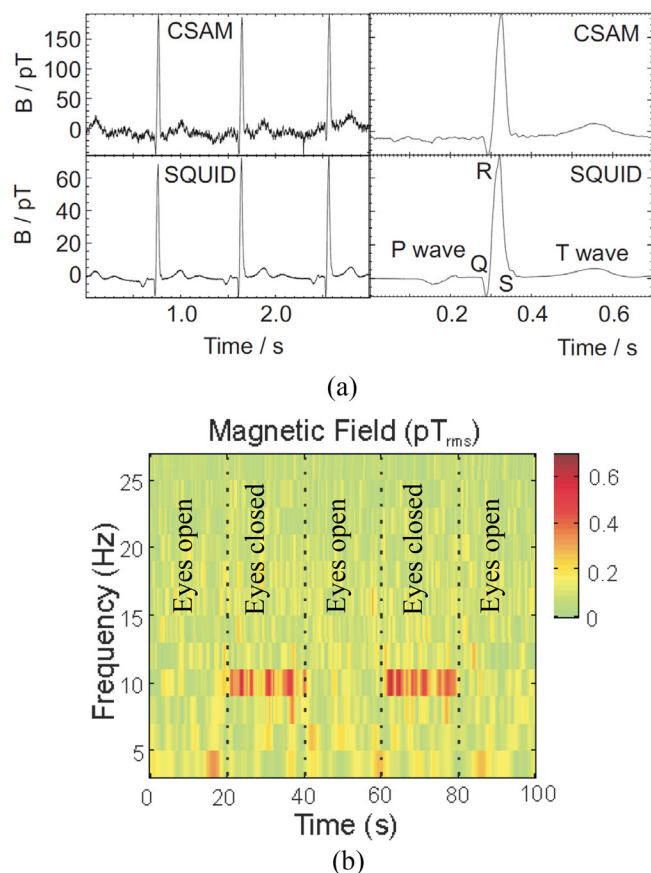


FIG. 47. Measurements of biomagnetic signals with chip-scale atomic magnetometers. (a) The magnetic field produced by a human heart measured outside the subject's chest. Reprinted with permission from Appl. Phys. Lett. **97**, 133703 (2010). Copyright 2010 AIP Publishing LLC. (b) Measurements of brain magnetic fields with a chip-scale atomic magnetometer processed with a wavelet transform. The alpha-rhythm at 10 Hz is clearly visible in the intervals when the subject's eyes are closed. Reprinted with permission from T. H. Sander *et al.*, Biomed. Opt. Express **3**, 981–990 (2012). Copyright 2012 the Optical Society of America.

magnetic fields on the order of 100 pT and 1 pT respectively, when measured outside the body. Magnetic sensors based on superconducting quantum interference devices (SQUIDs) have been able to detect these signals since the 1970s and such measurements are now used commercially in magneto-cardiography (MCG) and magnetoencephalography (MEG) systems for clinical applications such as the diagnosis and treatment of epilepsy.

An early demonstration of the detection of biomagnetic signals with atomic magnetometers<sup>233</sup> has been improved on considerably using new sensitivity-enhancing techniques such as the suppression of spin-exchange collisions. High-resolution measurements of both heart<sup>234–236</sup> and brain<sup>237</sup> magnetic fields have been demonstrated over the last 20 years and atomic magnetometers are gaining acceptance within the biomagnetics community as a noteworthy alternative to cryogenically cooled SQUIDs.<sup>238,239</sup>

Measurements of magnetic fields produced by the heart have been carried out with chip-scale atomic magnetometers<sup>217,240</sup> and have been confirmed with near-simultaneous SQUID-based measurements. The somewhat

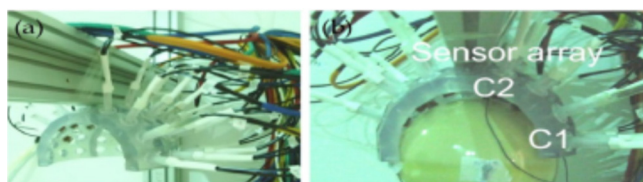


FIG. 48. An array of chip-scale atomic magnetometers arranged on a plastic helmet for imaging of brain magnetic signals. Reprinted with permission from O. Alem *et al.*, Opt. Express **25**, 7849–7858 (2017). Copyright 2017 the Optical Society of America.

worse sensitivity of these early chip-scale atomic magnetometers was partially offset by an increase in the detected signal due to the proximity of the chip-scale magnetometers to the sources, as compared with the SQUIDS, which require considerable thermal shielding to function in a room-temperature environment. Representative signals from the detection of a human heartbeat measured near the subject's chest for both SQUIDS and atomic magnetometers are shown in Fig. 47(a). While the noise is larger due to worse sensitivity of the chip-scale atomic magnetometer, the signal is several times larger due to the closer proximity of the sensor head to the source. Improvements in the device sensitivity<sup>210</sup> led to the ability to measure brain magnetic fields,<sup>241</sup> and chip-scale atomic magnetometers have demonstrated detection of both alpha rhythms and evoked responses. The alpha-rhythm is a well-known signal in electro- and magneto-encephalography and appears as a small peak in the broadband detected signal spectrum at 10 Hz. The alpha-rhythm is known to increase when the subject closes his/her eyes and can therefore serve as a confirmation that actual brain signals are being measured rather than some other type of noise. Alpha-rhythms detected by a chip-scale atomic magnetometer<sup>241</sup> are shown in Fig. 47(b).

The main clinical application of MEG at present is the diagnosis and treatment of epilepsy. The ability to measure epileptic discharges is therefore an important demonstration for any new magnetometer technology and such measurements were carried out in mice.<sup>242</sup> The development of flexible, reconfigurable chip-scale atomic magnetometer arrays<sup>222</sup> has enabled the detection of fetal magnetocardiographic signals with reduced interference from the heartbeat of the mother.<sup>222</sup> A photograph of the array used for MEG imaging is shown in Fig. 48.

#### D. Chip-scale atomic magnetometers for space

Chip-scale atomic magnetometers are also under development for applications in space,<sup>243,244</sup> primarily for planetary science missions. These instruments are based on Mx or Mz mode detection and incorporate a novel Silicon-on-Sapphire (SOS) CMOS heater chip. The SOS-COMS chip has several desirable features: the use of sapphire to efficiently spread heat generated in electrical heater traces at the chip edge to the center of the cell window; very narrow heater traces ( $\sim 1 \mu\text{m}$ ) to allow for high electrical resistance and very close proximity of neighboring opposing current flow to reduce magnetic fields; and temperature-sensing diodes coupled to on-chip signal conditioning circuits. Control electronics based

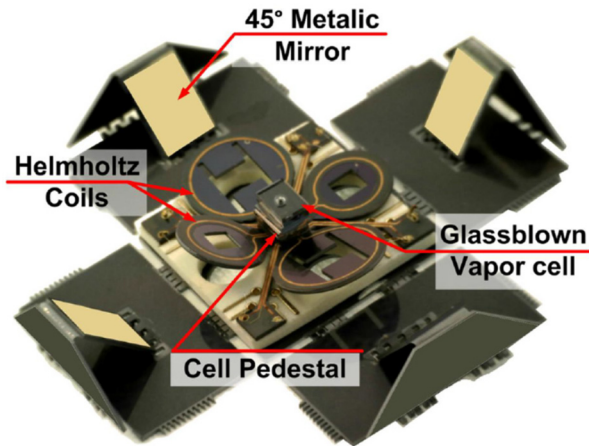


FIG. 49. Implementation of a NMR gyroscope using a folded MEMS design. Components are fabricated on a single silicon backplane and folded to achieve the appropriate optical geometry. Reprinted, with permission, from R. M. Noor *et al.*, in *Proceeding of 2017 IEEE International Symposium on Inertial Sensors and Systems (INERTIAL)* (2017), pp. 156-159. Copyright 2017 IEEE.

on field-programmable gate arrays (FPGAs) were developed to process the magnetometer physics package output signals and an overall sensitivity of  $15 \text{ pT}/\sqrt{\text{Hz}}$  was demonstrated.

## V. CHIP-SCALE ATOMIC GYROSCOPES

### A. Nuclear magnetic resonance gyroscopes

Throughout the 1970s and early 1980s, there was considerable activity to develop gyroscopes based on the precession of nuclear spins in a magnetic field. The core ideas are described above in Sec. IE. With the advent of the ring-laser gyro and the fiber-optic gyro in the mid-1980s, the development of NMR gyroscopes was largely halted. A resurgence in activity occurred starting in the mid-2000s and was precipitated by three main factors: the availability of new electronic parts capable, for example, of carrying out efficient division of frequencies; the development of new, low-power light sources such as vertical-cavity surface-emitting lasers; and the development of microfabricated alkali vapor cells, as described above. Each of these developments brought new

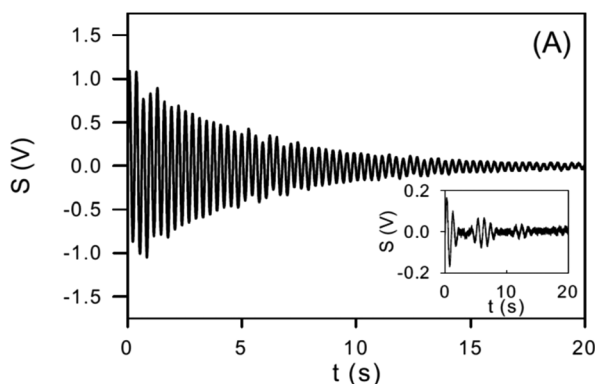


FIG. 50. Decay of the polarization of Xe gas of natural abundance confined with alkali atoms in a microfabricated vapor cell. Reprinted with permission from E. A. Donley *et al.*, *Phys. Rev. A* **79**, 013420 (2009). Copyright 2009 American Physical Society.

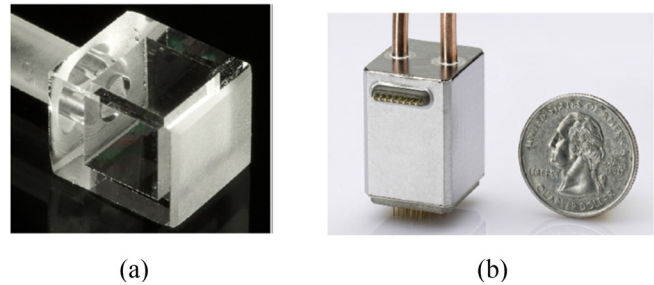


FIG. 51. (a) Compact glass vapor cell and (b) compact NMR gyroscope physics package with a total volume of  $1 \text{ cm}^3$ . From Walker and Larsen, *Advances in Atomic, Molecular, and Optical Physics*. Copyright 2016 Elsevier. Reprinted with permission from Elsevier.

possibilities for the development of more compact and low-power instruments.

### B. Device design, fabrication, and performance

Some early ideas for miniaturized NMR gyroscopes using MEMS technology<sup>245</sup> proposed the use of out-of-plane microfabricated optical elements such as mirrors, fresnel lenses, grating polarizers, and waveplates to route light around the surface of the chip. The proposed cell design was a small spherical cell, through which perpendicular beams could be passed to enable optical pumping and probing along perpendicular axes. More sophisticated approaches have been developed<sup>246</sup> using origami-like folding of planar micromachined silicon structures, as shown in Fig. 49.

Spin-exchange optical pumping of  $^{129}\text{Xe}$  and  $^{131}\text{Xe}$  atoms was demonstrated<sup>247</sup> in a cubic microfabricated vapor cell of volume  $1 \text{ mm}^3$  at  $145^\circ\text{C}$ , with a spin-polarization lifetime of 5 s, as shown in Fig. 50. A large nuclear quadrupole splitting for  $^{131}\text{Xe}$  was observed in these cells of about 200 mHz, attributed to the fact that the walls of the cell were made of different materials (silicon and glass). Even longer spin lifetimes, above 20 s, have been observed in some compact cells.<sup>248</sup>

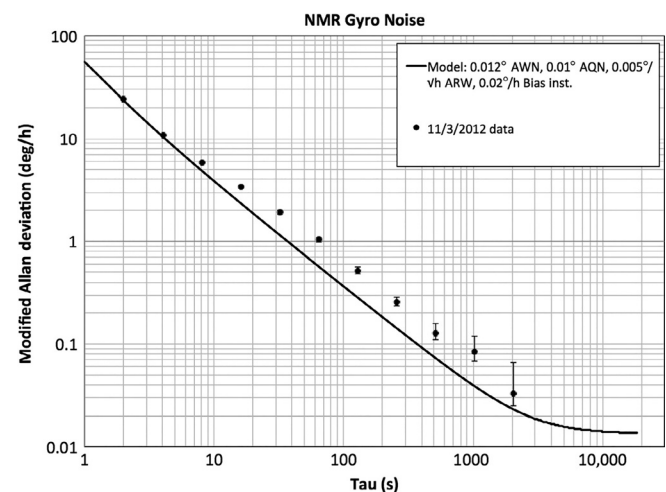


FIG. 52. Stability of the NMR gyro shown in Fig. 51. From Walker and Larsen, *Advances in Atomic, Molecular, and Optical Physics*. Copyright 2016 Elsevier. Reprinted with permission from Elsevier.

A compact NMR gyroscope physics package<sup>63,248</sup> with a total volume of  $10\text{ cm}^3$  is shown in Fig. 51. The gyroscope was based on millimeter-scale alkali/noble gas vapor cells filled using conventional glass-blowing techniques.<sup>63</sup> An angle-random walk of  $0.005\text{ deg}/\sqrt{\text{h}}$ , a bias instability of  $0.02\text{ deg}/\text{h}$ , shown in Fig. 52, and a scale factor stability of about 4 ppm were reported.

High-performance, compact magnetic shields have been developed to satisfy the stringent shielding requirements of NMR gyro technology.<sup>249</sup> A five-layer set of nested shields with volumes ranging from  $2.5\text{ cm}^3$  to  $0.01\text{ cm}^3$  were demonstrated. The shielding factor for the three outer-most layers was measured to be  $6 \times 10^6$ , and the shielding factor for all five layers together was calculated to be possibly as high as  $10^{11}$ . This high shielding factor is a result of the very strong scaling with shield dimension for multi-layer shields under the condition that the shield thickness remains constant.<sup>250</sup>

## VI. OTHER INSTRUMENTS AND TECHNOLOGIES

### A. Integration of atoms and photonics

The devices and instruments described above, while compact and low-power, are still based on the propagation of light as a free-space beam. Increased manufacturability, and much lower size and power, could potentially be achieved by connecting the light source to the cell using single-mode photonic waveguides. If atomic vapor cells could be integrated with optical fibers or into silicon or silicon nitride photonic circuits, the complexity and functionality of chip-scale atomic devices could be increased considerably. Thermal atomic vapors can be loaded around tapered fibers<sup>251</sup> or into hollow-core optical fibers<sup>110,252–258</sup> or hollow waveguides on a chip.<sup>111,259</sup> This allows for long interaction lengths, while maintaining strong transverse confinement, which can be useful for low-power non-linear optics. Laser-cooled atoms have also been coupled to tapered optical fibers,<sup>260,261</sup> photonic crystals,<sup>262,263</sup> or photonic optical resonators<sup>264</sup> for experiments in quantum optics and cavity quantum electrodynamics.

Optical frequency references based on acetylene-filled hollow core optical fibers<sup>109</sup> have achieved frequency uncertainties in the range of  $10\text{ kHz}$  near  $1.5\ \mu\text{m}$ .<sup>265</sup>

On-chip approaches using thermal vapors offers simplicity and the potential for high design complexity. For example, the waveguide can be directly exposed to an atomic vapor, such that the evanescent field around the waveguide interacts with the atoms. Chip-based “atomic cladding” coupling,

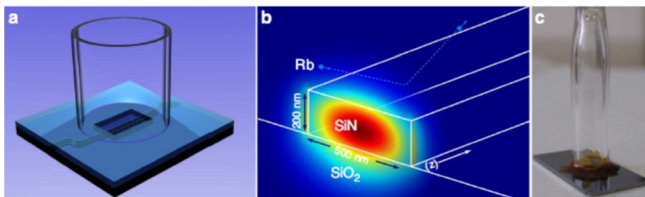


FIG. 53. Atomic cladding waveguide. (a) Schematic showing the exposed SiN waveguides inside a glass cell. (b) Calculated mode profile of the optical field in the waveguide. (c) Photograph of final chip with the alkali vapor cell attached. Reprinted with permission from L. Stern *et al.*, Nat. Commun. 4, 1548 (2012). Copyright 2012 Nature Publishing Group.

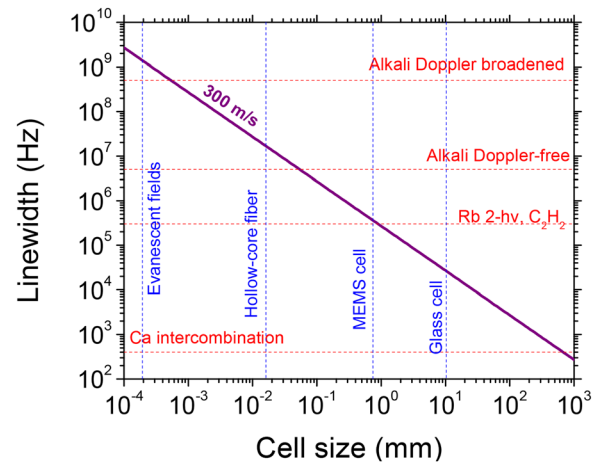


FIG. 54. Transit time broadening as a function of beam size for an atom moving at  $300\text{ m/s}$ .<sup>308</sup> Reprinted with permission from J. Kitching *et al.*, J. Phys.: Conf. Ser. 723, 012056 (2016). Copyright 2016 Institute of Physics.

shown in Fig. 53, has been demonstrated in SiN waveguides and Rb vapor.<sup>114,266–270</sup> This approach has the potential for high manufacturability, particularly for low-power nonlinear optics. Despite large transit-time broadening ( $\sim 100\text{ MHz}$ ) and light shifts, the high degree of integration may allow for extremely small wavelength references. This evanescent field approach has also been used in the development of photonically integrated molecular sensors in Si using ring resonators,<sup>271</sup> photonic crystals<sup>272</sup> or long, serpentine waveguides to increase absorption.<sup>273</sup>

The transit-time broadening and light shifts in small-dimension photonic systems can be reduced by expanding the transverse dimensions of the light beam. The transit time broadening of an atom or molecule with a transverse thermal velocity of  $300\text{ m/s}$  is shown as a function of the beam size in Fig. 54. Several cell/confinement geometries (vertical) and optical transition linewidths (horizontal) are also shown. The transit-time broadening in microfabricated vapor cells with dimensions between  $100\ \mu\text{m}$  and  $1\text{ mm}$  is consistent with the natural linewidth of single and two-photon transitions in alkali atoms and transitions between rotational-vibrational states in molecules. On the other hand, evanescent field interrogation is more appropriate for Doppler-broadened transitions, since the transit time is typically too short to resolve more narrow features.

A wavelength reference at  $780\text{ nm}$  based on this approach was recently demonstrated<sup>274</sup> with a stability of  $10^{-11}$  at integration times beyond  $10\text{ s}$ . In this design, transit-time broadening was reduced using grating output couplers<sup>275</sup> and a photonic extreme mode converter that generated a  $\sim 50\ \mu\text{m}$  output beam from a sub-micron mode in the waveguide.

### B. Field imaging

It is also possible to carry out spatially resolved measurements of hyperfine or electron spin polarizations in microfabricated alkali vapor cells. From such measurements, imaging of RF and magnetic fields that perturb the polarization can be done. Spatially resolved measurements of both

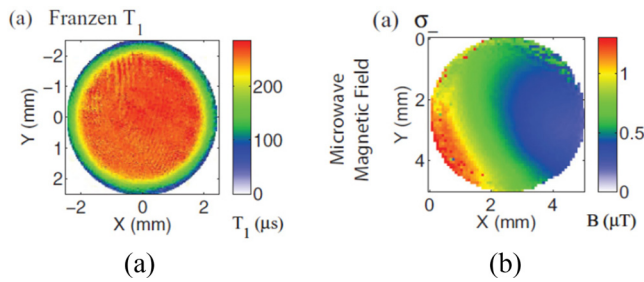


FIG. 55. Imaging of (a) the  $T_1$  relaxation time and (b) the amplitude of a microwave field inside a microwave cavity using a microfabricated alkali vapor cell. Reprinted with permission from A. Horsley *et al.*, Phys. Rev. A **88**, 063407 (2013). Copyright 2013 American Physical Society.

transverse and longitudinal polarization in a microfabricated cell inside a microwave cavity were carried out.<sup>276</sup> In these pulsed measurements, the atoms are first optically pumped into a single hyperfine level and the population of the depumped level is measured some time later using a probe pulse. A spatially resolved measurement of this level population as a function of time results in a transverse image of the relaxation time throughout the cell, as shown in Fig. 55(a). If instead a microwave field is injected into the cavity during the period between the pumping and population measurement pulses, a spatially resolved image of the microwave field amplitude can be deduced from Rabi flopping rate, as shown in Fig. 55(b).

Microfabricated cells with thin sidewalls can allow the alkali vapor to be very close to RF-emitting components, for example those in the surfaces of chips. This can allow imaging of the RF magnetic field above a coplanar waveguide carrying a microwave field resonant with the alkali hyperfine transition, for example.<sup>277</sup> A sensitivity of  $1.4 \mu\text{T}/\sqrt{\text{Hz}}$  at microwave frequencies with a spatial resolution of  $50 \mu\text{m}$  by  $50 \mu\text{m} \times 140 \mu\text{m}$  was obtained. Microwave field frequencies between 2.3 GHz and 26.4 GHz could be measured by tuning the DC field applied to the atoms.

### C. Other optical/atomic devices

Several other devices have been developed based on microfabricated alkali vapor cells. Doppler-free saturated absorption lines were obtained in a compact saturated absorption spectrometer,<sup>278</sup> and the microfabricated alkali vapor cells were used to implement a modulation-free dichroic atomic vapor laser lock.<sup>279,280</sup> VCSELs have been stabilized to optical transitions in a Cs MEMS cell<sup>281</sup> and a stability below  $10^{-8}$  was obtained at integration times from 1 s to  $10^4$  s. Microfabricated vapor cells were also used in a compact optical isolator.<sup>282</sup>

Laser cooling of atoms, developed in the late 1970s and 1980s, has led to substantial improvements in the performance of atomic clocks and underlies most primary frequency standards in leading national metrology labs. By cooling atoms to microkelvin temperatures using optical fields, the mean velocity of neutral atoms can be reduced to  $\sim 1$  cm/s or below. This implies that the atoms can be interrogated for much longer than in a room-temperature vapor without interaction with surfaces or other atoms. Current fountain atomic

clocks achieve interrogation times of  $\sim 1$  s, limited by the acceleration due to gravity and the size of the vacuum system that contains the atoms. With quality factors for alkali atom microwave transitions therefore approaching  $10^{10}$ , fractional frequency uncertainties near  $10^{-16}$  can be achieved. Laser cooling is also an important tool in atom interferometry, with the longer interrogation times leading to improved performance in, for example, gravimeters and gravity gradiometers.

The miniaturization of such instruments, while still in its infancy, has been investigated by several groups<sup>283–291</sup> for both defense and space applications. The dependence of the number of laser-cooled atoms, and hence the instrument signal-to-noise ratio, was investigated as a function of the cooling beam size.<sup>292</sup> This work suggested that the use of cell dimensions below 1 mm would make it difficult to achieve the signal-to-noise ratios needed for many clock applications. Progress has been made in the development of compact UHV chambers, convenient laser cooling approaches using single laser beams, and miniaturized laser and optical systems. While most existing clocks based on laser cooled atoms use large vacuum systems to allow long freefall times, it has been shown<sup>293</sup> that a frequency instability of  $3 \times 10^{-13}$  can be achieved with atoms falling only 1.6 mm during the interrogation period of 18 ms. Novel microfabricated structures, such as pyramidal<sup>294–298</sup> and grating-based reflectors,<sup>299–301</sup> have also been used to trap and cool atoms in simple, compact optical geometries. Atom chips<sup>302</sup> remain a compelling approach to manipulating laser-cooled atoms at the micro-scale and the compact systems<sup>303</sup> are beginning to be developed as clocks.<sup>304–306</sup> A proposal for a chip-based cold atom system was described in Ref. 307 and the reduction of helium permeation into microfabricated cells using appropriate materials has been demonstrated.<sup>118</sup> While much remains to be done in this area, the prospect of a microfabricated platform for the creation and manipulation of laser-cooled atoms is a compelling research direction that could lead to several miniaturized and highly precise instruments for timing and inertial sensing.

## VII. OUTLOOK

The concept of the chip-scale atomic clock grew out of several key developments in atomic physics, microengineering, and laser science that have occurred over the last 50 years. Coherent population trapping, integral to many of the CSAC efforts, has created a unique opportunity for miniaturized frequency standards. By avoiding the need for direct microwave excitation of hyperfine resonances in atoms, limitations to miniaturization related to the wavelength of the microwave transition can be avoided. The processes of microelectromechanical systems enable highly miniaturized alkali vapor cells, which, when integrated with vertical cavity surface-emitting lasers enable millimeter-scale structures running on tens of milliwatts of power, which achieve long term frequency stabilities comparable to their much larger counterparts.

Growing out of important research and ideas developed in 1990s, work began in earnest on the development of chip-scale atomic clocks in 2001. The first microfabricated alkali

vapor cells were demonstrated in 2003 and the first physics packages in 2004. A commercial product was released in 2011. Commercial devices are now being evaluated for use in several application areas including satellite-based navigation and underwater timing.

Microfabricated alkali vapor cells are finding increased use in other devices and instruments. Magnetometers have been demonstrated with sensitivity at the fT level that are now being used in applications ranging from biomagnetics to nuclear magnetic resonance. It appears possible that high performance, possibly approaching navigation grade, can be obtained from gyroscopes based on the precession of atoms in such cells. Higher levels of integration of atoms with optical systems are also being developed, in which free-space beams are being replaced with integrated photonics to increase manufacturability and reduce device size. It therefore appears that there are many more things to be done in this interesting and growing field of research.

## ACKNOWLEDGMENTS

This work is a contribution of NIST, an agency of the U.S. Government, and is not subject to copyright in the United States. We thank E. A. Donley, R. Lutwak, V. Maurice, G. Mileti, J. Moreland, and C. Oates for their thoughtful comments on the manuscript.

- <sup>1</sup>S. W. Thomson and P. G. Tait, *Elements of Natural Philosophy* (Cambridge University Press, 1879).
- <sup>2</sup>A. Kastler, *J. Phys. Radium* **11**, 255–265 (1950).
- <sup>3</sup>W. Happer, *Rev. Mod. Phys.* **44**, 169–249 (1972).
- <sup>4</sup>C. W. Chou *et al.*, *Phys. Rev. Lett.* **106**, 160801 (2011).
- <sup>5</sup>A. D. Ludlow *et al.*, *Rev. Mod. Phys.* **87**, 637–701 (2015).
- <sup>6</sup>M. Arditi, in *Proceeding of IEEE International Frequency Control Symposiums* (1958), pp. 606–622.
- <sup>7</sup>J. Vanier *et al.*, *Phys. Rev. A* **9**, 1031–1040 (1974).
- <sup>8</sup>A. Clairon *et al.*, *Europhys. Lett.* **16**, 165–170 (1991).
- <sup>9</sup>T. Kovachy *et al.*, *Nature* **528**, 530–533 (2015).
- <sup>10</sup>M. V. Balabas *et al.*, *Phys. Rev. Lett.* **105**, 070801 (2010).
- <sup>11</sup>T. R. Gentile *et al.*, *Rev. Mod. Phys.* **89**, 045004 (2017).
- <sup>12</sup>C. Gemmel *et al.*, *Eur. Phys. J. D* **57**, 303–320 (2010).
- <sup>13</sup>K. Szymaniec *et al.*, in *Proceeding of 8th Symposium on Frequency Standards and Metrology* (2016), p. 012003.
- <sup>14</sup>T. P. Heavner *et al.*, *Metrologia* **51**, 174–182 (2014).
- <sup>15</sup>R. H. Dicke, *Phys. Rev.* **89**, 472–473 (1953).
- <sup>16</sup>M. Arditi and T. R. Carver, *Phys. Rev.* **124**, 800–809 (1961).
- <sup>17</sup>J. Vanier and C. Audoin, *The Quantum Physics of Atomic Frequency Standards* (Adam Hilger, Bristol, 1992).
- <sup>18</sup>H. Margenau *et al.*, *Phys. Rev.* **115**, 87–92 (1959).
- <sup>19</sup>These constants are tabulated in, for example, Ref. 17.
- <sup>20</sup>M. A. Bouchiat *et al.*, *Phys. Rev. Lett.* **5**, 373–375 (1960).
- <sup>21</sup>H. Goldenberg *et al.*, *Phys. Rev.* **123**, 530–537 (1961).
- <sup>22</sup>D. Budker *et al.*, *Phys. Rev. A* **71**, 012903 (2005).
- <sup>23</sup>H. G. Robinson and C. E. Johnson, *Appl. Phys. Lett.* **40**, 771–773 (1982).
- <sup>24</sup>W. Happer and B. S. Mathur, *Phys. Rev.* **163**, 12 (1967).
- <sup>25</sup>S. Seltzer, Ph.D. thesis, Department of Physics, Princeton University, 2008.
- <sup>26</sup>T. R. Carver, in *Proceeding of IEEE International Frequency Control Symposiums* (1957), pp. 307–317.
- <sup>27</sup>M. Arditi and T. R. Carver, *Phys. Rev.* **109**, 1012–1013 (1958).
- <sup>28</sup>P. L. Bender *et al.*, *Phys. Rev. Lett.* **1**, 311–313 (1958).
- <sup>29</sup>E. Arimondo and G. Orriols, *Lett. Nuovo Cimento* **17**, 333–338 (1976).
- <sup>30</sup>E. Arimondo, *Prog. Opt.* **35**, 257–354 (1996).
- <sup>31</sup>J. E. Thomas *et al.*, *Phys. Rev. Lett.* **48**, 867–870 (1982).
- <sup>32</sup>S. Ezekiel *et al.*, *Phys. Rev. Lett.* **50**, 549–549 (1983).
- <sup>33</sup>P. R. Hemmer *et al.*, *Opt. Lett.* **8**, 440–442 (1983).
- <sup>34</sup>P. R. Hemmer *et al.*, *J. Opt. Soc. Am. B* **1**, 528–528 (1984).
- <sup>35</sup>P. R. Hemmer *et al.*, *Proc. 39th Annual Symposium on Frequency Control*, pp. 88–90 (1985).
- <sup>36</sup>N. Cyr *et al.*, *IEEE Trans. Instrum. Meas.* **42**, 640–649 (1993).
- <sup>37</sup>F. Levi *et al.*, in *Proceeding of European Frequency and Time Forum* (1997), pp. 216–220.
- <sup>38</sup>J. Vanier *et al.*, *Phys. Rev. A* **58**, 2345–2358 (1998).
- <sup>39</sup>A. Godone *et al.*, *IEEE Trans. Instrum. Meas.* **48**, 504–507 (1999).
- <sup>40</sup>A. Godone *et al.*, *Phys. Rev. A* **59**, R12–R15 (1999).
- <sup>41</sup>F. Levi *et al.*, *IEEE Trans. Ultrason. Ferroelectr. Freq. Control* **46**, 609–615 (1999).
- <sup>42</sup>M. Violetti *et al.*, *IEEE Sens.* **14**, 3193–3200 (2014).
- <sup>43</sup>V. Shah and J. Kitching, in *Advances in Atomic, Molecular, and Optical Physics*, edited by E. Arimondo, P. Berman, and C. Chin (Elsevier, 2010), Vol. 59, pp. 21–74.
- <sup>44</sup>C. H. Henry, *IEEE J. Quantum Electron.* **18**, 259–264 (1982).
- <sup>45</sup>A. B. Post *et al.*, *Phys. Rev. A* **72**, 033417 (2005).
- <sup>46</sup>V. Venkatraman *et al.*, in *Proceedings of IEEE International Frequency Control Symposiums and European Frequency and Time Forum* (2011), pp. 804–807.
- <sup>47</sup>V. Venkatraman *et al.*, *Appl. Phys. Lett.* **104**, 054104 (2014).
- <sup>48</sup>J. A. Kusters and C. A. Adams, RF Design (May 1999), pp. 28–38.
- <sup>49</sup>S. Micalizio *et al.*, *Metrologia* **49**, 425–436 (2012).
- <sup>50</sup>D. Budker and M. Romalis, *Nat. Phys.* **3**, 227–234 (2007).
- <sup>51</sup>E. B. Alexandrov, *Phys. Scr.* **T105**, 27–30 (2003).
- <sup>52</sup>J. Dupont-Roc *et al.*, *Phys. Lett. A* **28**, 638 (1969).
- <sup>53</sup>W. Happer and H. Tang, *Phys. Rev. Lett.* **31**, 273–276 (1973).
- <sup>54</sup>W. Happer and A. C. Tam, *Phys. Rev. A* **16**, 1877–1891 (1977).
- <sup>55</sup>J. C. Allred *et al.*, *Phys. Rev. Lett.* **89**, 130801 (2002).
- <sup>56</sup>I. K. Kominis *et al.*, *Nature* **422**, 596–599 (2003).
- <sup>57</sup>S. Appelt *et al.*, *Phys. Rev. A* **59**, 2078–2084 (1999).
- <sup>58</sup>B. D. Leete, U.S. patent 2,720,625 (11 October 1955).
- <sup>59</sup>E. Kanegsberg, *Proc. SPIE* **157**, 73–80 (1978).
- <sup>60</sup>B. C. Grover *et al.*, U.S. patent 4,157,495 (1979).
- <sup>61</sup>T. G. Walker and W. Happer, *Rev. Mod. Phys.* **69**, 629–642 (1997).
- <sup>62</sup>F. A. Karwacki, *J. Inst. Navig.* **27**, 72–78 (1980).
- <sup>63</sup>T. G. Walker and M. S. Larsen, in *Advances in Atomic, Molecular, and Optical Physics*, edited by E. Arimondo, C. C. Lin, and S. F. Yelin (Elsevier, 2016), Vol. 65, pp. 373–401.
- <sup>64</sup>D. Meyer and M. Larsen, *Gyroscopy Navig.* **5**, 75–82 (2014).
- <sup>65</sup>E. A. Donley, in *Proceeding of IEEE Sensor Conference* (2010), pp. 17–22.
- <sup>66</sup>J. Kitching *et al.*, *IEEE Sens.* **11**, 1749–1758 (2011).
- <sup>67</sup>E. A. Donley and J. Kitching, in *Optical Magnetometry*, edited by D. Budker and D. J. Kimball (Cambridge University Press, 2013), pp. 369–386.
- <sup>68</sup>S. K. Lamoreaux *et al.*, *Phys. Rev. Lett.* **57**, 3125–3128 (1986).
- <sup>69</sup>M. E. Limes *et al.*, *Phys. Rev. Lett.* **120**, 033401 (2018).
- <sup>70</sup>T. W. Kornack *et al.*, *Phys. Rev. Lett.* **95**, 230801 (2005).
- <sup>71</sup>M. Arditi and J. L. Picque, *J. Phys. Lett.* **41**, 379–381 (1980).
- <sup>72</sup>M. Arditi, *Metrologia* **18**, 59–66 (1982).
- <sup>73</sup>M. Feldman *et al.*, in *Proceeding of IEEE International Frequency Control Symposiums* (1981), pp. 625–636.
- <sup>74</sup>M. Hashimoto and M. Ohtsu, *IEEE J. Quantum Electron.* **23**, 446–451 (1987).
- <sup>75</sup>J. H. Shirley *et al.*, *Metrologia* **38**, 427 (2001).
- <sup>76</sup>R. Lutwak *et al.*, in *Proceeding of Precise Time and Time Interval (PTTI) Meeting* (2001), pp. 19–32.
- <sup>77</sup>T. Sakaguchi *et al.*, *Electron. Lett.* **24**, 928–929 (1988).
- <sup>78</sup>F. Koyama *et al.*, *Appl. Phys. Lett.* **55**, 221–222 (1989).
- <sup>79</sup>J. L. Jewell *et al.*, *IEEE J. Quantum Electron.* **27**, 1332–1346 (1991).
- <sup>80</sup>H. Soda *et al.*, *Jpn. J. Appl. Phys.* **18**, 2329 (1979).
- <sup>81</sup>N. Jikutani *et al.*, in *Proceeding of Vertical-Cavity Surface-Emitting Lasers* (2016), Vol. XX, pp. 976601–976605.
- <sup>82</sup>D. G. Deppe *et al.*, *IEEE J. Sel. Top. Quantum Electron.* **3**, 893–904 (1997).
- <sup>83</sup>H. P. Zappe, in *Proceeding of Precise Time and Time Interval (PTTI) Meeting* (1999), pp. 589–596.
- <sup>84</sup>C. Affolderbach *et al.*, *Appl. Phys. B* **70**, 407–413 (2000).
- <sup>85</sup>P. J. Chantry *et al.*, in *Proceedings of IEEE International Frequency Control Symposiums* (1996), pp. 1002–1010.
- <sup>86</sup>N. Gavva *et al.*, *Appl. Phys. Lett.* **92**, 221113 (2008).
- <sup>87</sup>J. Kitching *et al.*, *J. Opt. Soc. Am. B* **18**, 1676–1683 (2001).
- <sup>88</sup>J. Kitching *et al.*, *IEEE Trans. Instrum. Meas.* **49**, 1313–1317 (2000).
- <sup>89</sup>D. K. Serkland *et al.*, *Proc. SPIE* **6484**, 648406 (2007).

- <sup>90</sup>R. Lutwak *et al.*, in *Proceeding of Precise Time and Time Interval (PTTI) Meeting* (2003), pp. 467–478.
- <sup>91</sup>J. W. Zhang *et al.*, *Opt. Express* **23**, 14763–14773 (2015).
- <sup>92</sup>J. Zhang *et al.*, *Laser Phys. Lett.* **10**, 045802 (2013).
- <sup>93</sup>M. Ellmeier *et al.*, *Appl. Phys. B* **124**, 18 (2018).
- <sup>94</sup>F. A. Camargo *et al.*, *IEEE Photonics Technol. Lett.* **24**, 1218–1220 (2012).
- <sup>95</sup>F. A. Camargo *et al.*, in *Proceeding of Vertical External Cavity Surface Emitting Lasers (VECSELs)* (2013), Vol. III.
- <sup>96</sup>D. K. Serkland *et al.*, *Proc. SPIE* **7952**, 79520L (2011).
- <sup>97</sup>W. Espe, *Materials of High Vacuum Technology* (Pergamon Press, Oxford, New York, 1966).
- <sup>98</sup>H. A. Liebhafsky and A. F. Winslow, *J. Appl. Phys.* **18**, 1128–1132 (1947).
- <sup>99</sup>D. G. Lovering, *Molten Salt Technology* (Springer Science+Business Media, LLC, 1982).
- <sup>100</sup>L. Nieradko *et al.*, *J. Micro/Nanolithogr. MEMS MOEMS* **7**, 033013 (2008).
- <sup>101</sup>K. Tsujimoto *et al.*, in *Proceeding of IEEE International Conference on Micro Electro Mechanical Systems* (2011), pp. 368–371.
- <sup>102</sup>L.-A. Liew *et al.*, in *Proceeding of Eurosensors* (2006).
- <sup>103</sup>M. Hirashima and M. Asano, in *Advances in Electronics and Electron Physics*, edited by J. D. McGee, D. McMullan, and E. Kahan (Elsevier, 1966), Vol. 22A, p. 643.
- <sup>104</sup>R. C. Burt, thesis, California Institute of Technology, 1926.
- <sup>105</sup>P. P. Kumar and S. Yashonath, *J. Chem. Sci.* **118**, 135–154 (2006).
- <sup>106</sup>J. J. Bernstein *et al.*, *Solid State Ionics* **198**, 47–49 (2011).
- <sup>107</sup>S. Kang *et al.*, *Appl. Phys. Lett.* **110**, 244101 (2017).
- <sup>108</sup>S. Knappe *et al.*, *Rev. Sci. Instrum.* **74**, 3142–3145 (2003).
- <sup>109</sup>R. Thapa *et al.*, *Opt. Lett.* **31**, 2489–2491 (2006).
- <sup>110</sup>S. Ghosh *et al.*, *Phys. Rev. Lett.* **97**, 023603 (2006).
- <sup>111</sup>W. G. Yang *et al.*, *Nat. Photonics* **1**, 331 (2007).
- <sup>112</sup>M. V. Balabas *et al.*, *J. Opt. Soc. Am. B* **23**, 1001–1006 (2006).
- <sup>113</sup>L. Hollberg and J. Kitching, U.S. patent 6,806,784 B2 (2004).
- <sup>114</sup>L. Stern *et al.*, *Nat. Commun.* **4**, 1548 (2013).
- <sup>115</sup>R. Daschner *et al.*, *Appl. Phys. Lett.* **105**, 041107 (2014).
- <sup>116</sup>J. F. Hulbert *et al.*, *J. Vac. Sci. Technol. A* **31**, 033001 (2013).
- <sup>117</sup>G. Wallis and D. I. Pomerantz, *J. Appl. Phys.* **40**, 3946–3949 (1969).
- <sup>118</sup>A. T. Dellis *et al.*, *Opt. Lett.* **41**, 2775–2778 (2016).
- <sup>119</sup>F. J. Norton, *J. Am. Ceram. Soc.* **36**, 90–96 (1953).
- <sup>120</sup>M. Zhu *et al.*, in *Proceedings of IEEE International Frequency Control Symposiums and IEEE Transactions Ultrasonics, Ferroelectrics, and Frequency Control* (2004), pp. 100–103.
- <sup>121</sup>M. Hasegawa *et al.*, *Sens. Actuators A* **167**, 594–601 (2011).
- <sup>122</sup>L. A. Liew *et al.*, *Appl. Phys. Lett.* **84**, 2694–2696 (2004).
- <sup>123</sup>M. H. Kwakernaak *et al.*, in *Proceeding of Precise Time and Time Interval (PTTI) Meeting* (2004), pp. 355–368.
- <sup>124</sup>R. Lutwak *et al.*, in *Proceeding of Precise Time and Time Interval (PTTI) Meeting* (2004), pp. 339–354.
- <sup>125</sup>F. Vecchio *et al.*, *Sens. Actuators A* **172**, 330–335 (2011).
- <sup>126</sup>R. Lutwak, in *Proceeding of Precise Time and Time Interval (PTTI) Meeting* (2011), pp. 207–220.
- <sup>127</sup>C.-H. Lee *et al.*, in *Proceeding of Hilton Head Solid-State Sensor, Actuator and Microsystems Workshop* (2004).
- <sup>128</sup>S. Radhakrishnan and A. Lal, in *Proceeding of Hilton Head Solid-State Sensor, Actuator and Microsystems Workshop* (2005), pp. 23–26.
- <sup>129</sup>S. Knappe *et al.*, *Opt. Lett.* **30**, 2351–2353 (2005).
- <sup>130</sup>A. Douahi *et al.*, *Electron. Lett.* **43**, 279–280 (2007).
- <sup>131</sup>Pills of this form are sold by SAES Getters. The use of product names is for technical clarity only and does not imply endorsement by NIST.
- <sup>132</sup>D. Miletic *et al.*, *Electron. Lett.* **46**, 1069–1070 (2010).
- <sup>133</sup>E. Kroemer *et al.*, *Opt. Express* **23**, 18373–18380 (2015).
- <sup>134</sup>V. Maurice *et al.*, *Appl. Phys. Lett.* **110**, 164103 (2017).
- <sup>135</sup>S. V. Ermak *et al.*, *St. Petersburg Polytechnical Univ. J.: Phys. Math.* **1**, 37–41 (2015).
- <sup>136</sup>J. D. Francesco *et al.*, in *Proceeding of Semiconductor Lasers and Laser Dynamics* (2010), Vol. IV, pp. 77201T–77209T.
- <sup>137</sup>F. Gong *et al.*, *Rev. Sci. Instrum.* **77**, 076101 (2006).
- <sup>138</sup>L.-A. Liew *et al.*, *Appl. Phys. Lett.* **90**, 114106–114103 (2007).
- <sup>139</sup>S. Woetzel *et al.*, *Rev. Sci. Instrum.* **82**, 033111 (2011).
- <sup>140</sup>K. Tsujimoto *et al.*, *J. Micromech. Microeng.* **23**, 115003 (2013).
- <sup>141</sup>K. Ban *et al.*, *J. Vac. Sci. Technol. A* **34**, 061601 (2016).
- <sup>142</sup>S. Woetzel *et al.*, *Surf. Coat. Technol.* **221**, 158–162 (2013).
- <sup>143</sup>S. Karlen *et al.*, *Opt. Express* **25**, 2187–2194 (2017).
- <sup>144</sup>S. Abdullah *et al.*, *Appl. Phys. Lett.* **106**, 163505 (2015).
- <sup>145</sup>E. J. Eklund *et al.*, *Sens. Actuators A* **143**, 175–180 (2008).
- <sup>146</sup>Y. Ji *et al.*, in *Proceeding of IEEE Electrical and Computer Technology Conference* (2015), pp. 946–949.
- <sup>147</sup>M. A. Perez *et al.*, *Sens. Actuators A* **154**, 295–303 (2009).
- <sup>148</sup>M. A. Perez *et al.*, *Sens. Actuators A* **155**, 23–32 (2009).
- <sup>149</sup>R. Chutani *et al.*, *Sci. Rep.* **5**, 14001 (2015).
- <sup>150</sup>Y. Petremand *et al.*, *J. Micromech. Microeng.* **22**, 025013 (2012).
- <sup>151</sup>N. Dural and M. V. Romalis, *APL Mater.* **2**, 086101 (2014).
- <sup>152</sup>R. Daschner *et al.*, *Opt. Lett.* **37**, 2271–2273 (2012).
- <sup>153</sup>R. Ijsselsteijn *et al.*, *Rev. Sci. Instrum.* **83**, 113106 (2012).
- <sup>154</sup>T. Baluksian *et al.*, *Opt. Lett.* **35**, 1950–1952 (2010).
- <sup>155</sup>R. Straessle *et al.*, *Appl. Phys. Lett.* **105**, 043502 (2014).
- <sup>156</sup>S. J. Seltzer and M. V. Romalis, *J. Appl. Phys.* **106**, 114905 (2009).
- <sup>157</sup>S. Woetzel *et al.*, *J. Micromech. Microeng.* **24**, 095001 (2014).
- <sup>158</sup>S. Karlen *et al.*, in *Proceedings of 2017 Joint Conference of the European Frequency and Time Forum and IEEE International Frequency Control Symposium (EFTF/IFCS)* (2017), pp. 625–627.
- <sup>159</sup>A. T. Gardner *et al.*, *A Second Look at Chip Scale Atomic Clocks for Long Term Precision Timing Four Years in the Field* (IEEE, New York, 2016).
- <sup>160</sup>S. Knappe *et al.*, *Appl. Phys. Lett.* **85**, 1460–1462 (2004).
- <sup>161</sup>R. Lutwak *et al.*, in *Proceeding of Precise Time and Time Interval (PTTI) Meeting* (2007), pp. 269–290.
- <sup>162</sup>J. R. Vig, *IEEE Trans. Ultrason. Ferroelectr. Freq. Control* **40**, 522–527 (1993).
- <sup>163</sup>R. Filler and J. Vig, in *Proceeding of Institute of Navigation Annual Meeting* (1995).
- <sup>164</sup>H. Fruehauf, in *Proceeding of Precise Time and Time Interval (PTTI) Meeting* (2001), pp. 359–369.
- <sup>165</sup>H. C. Nathanson *et al.*, in *Proceeding of IEEE International Conference on Micro Electro Mechanical Systems* (1995), pp. 72–76.
- <sup>166</sup>J. Kitching *et al.*, *Appl. Phys. Lett.* **81**, 553–555 (2002).
- <sup>167</sup>K. Hyeun-Su *et al.*, in *Proceeding of IEEE International Conference on Micro Electro Mechanical Systems* (2007), pp. 852–855.
- <sup>168</sup>S. Knappe *et al.*, in *Proceeding of IEEE International Ultrasonics, Ferroelectrics, and Frequency Control, 50th Anniversary Joint Conference* (2004), pp. 87–91.
- <sup>169</sup>S. Knappe *et al.*, *Opt. Express* **13**, 1249–1253 (2005).
- <sup>170</sup>M. Stahler *et al.*, *Opt. Lett.* **27**, 1472–1474 (2002).
- <sup>171</sup>M. Zhu, U.S. patent 6,359,916 (2002).
- <sup>172</sup>R. Lutwak *et al.*, in *Proceedings of IEEE International Frequency Control Symposiums and European Frequency and Time Forum* (2007), pp. 1327–1333.
- <sup>173</sup>D. W. Youngner *et al.*, in *Proceeding of IEEE Transducers* (2007), pp. 39–44.
- <sup>174</sup>J. F. DeNatale *et al.*, in *Proceeding of IEEE Position Location and Navigation Symposium (PLANS)* (2008), pp. 67–70.
- <sup>175</sup>D. W. Youngner *et al.*, U.S. patent 6,900,702 (2005).
- <sup>176</sup>H. C. Nathanson and I. Liberman, U.S. patent 6,570,459 (2003).
- <sup>177</sup>L.-A. Liew *et al.*, in *Proceeding of Eurosensors* (2007).
- <sup>178</sup>L. Wu *et al.*, in *Proceeding of International Conference on Electronic Packaging Technology* (2015).
- <sup>179</sup>S. L. Li *et al.*, *Chin. Phys. B* **23**, 074302 (2014).
- <sup>180</sup>C. Audoin *et al.*, *IEEE Trans. Instrum. Meas.* **40**, 121–125 (1991).
- <sup>181</sup>A. Brannon *et al.*, in *Proceeding of IEEE Microwave Theory and Techniques Society Symposium* (2005).
- <sup>182</sup>A. Brannon *et al.*, in *Proceeding of IEEE International Frequency Control Symposiums* (2006), pp. 443–447.
- <sup>183</sup>K. M. Lakin and J. S. Wang, *Appl. Phys. Lett.* **38**, 125–127 (1981).
- <sup>184</sup>H. Yu *et al.*, in *Proceeding of IEEE Transactions on Ultrasonics, Ferroelectrics, and Frequency Control* (2009).
- <sup>185</sup>S. Romisch and R. Lutwak, in *Proceeding of IEEE International Frequency Control Symposiums* (2006), pp. 448–451.
- <sup>186</sup>J. Lei *et al.*, *Int. J. Mod. Phys. B* **31**, 1741010 (2017).
- <sup>187</sup>D. Ruffieux *et al.*, in *Proceeding of IEEE International Solid-State Circuits Conference* (2011), pp. 48–50.
- <sup>188</sup>Y. Z. Zhao *et al.*, *IEEE Trans. Instrum. Meas.* **64**, 263–270 (2015).
- <sup>189</sup>J. Vanier *et al.*, in *Proceedings of IEEE International Frequency Control Symposiums and IEEE Transactions Ultrasonics, Ferroelectrics, and Frequency Control* (2004), pp. 92–99.
- <sup>190</sup>J. Vanier *et al.*, *IEEE Trans. Instrum. Meas.* **54**, 2531–2539 (2005).
- <sup>191</sup>R. Lutwak *et al.*, in *Proceedings of IEEE International Frequency Control Symposium and Precise Time and Time Interval (PTTI) Meeting* (2005), pp. 752–757.

- <sup>192</sup>J. Haesler *et al.*, in *Proceedings of IEEE International Frequency Control Symposiums and European Frequency and Time Forum* (2011), pp. 225–229.
- <sup>193</sup>V. Gerginov *et al.*, *Opt. Lett.* **31**, 1851–1853 (2006).
- <sup>194</sup>M. Zhu and L. S. Cutler, in *Proceeding of Precise Time and Time Interval (PTTI) Meeting* (2000), pp. 311–324.
- <sup>195</sup>V. Shah *et al.*, *Appl. Phys. Lett.* **89**, 151124 (2006).
- <sup>196</sup>Microsemi (2011).
- <sup>197</sup>A. Ucar *et al.*, *J. Navig.* **66**, 449–464 (2013).
- <sup>198</sup>M. A. Sturza, *Navigation* **2**, 146–156 (1984).
- <sup>199</sup>R. Ramlall *et al.*, in *Proceeding of International Technical Meeting of the Satellite Division of the Institute of Navigation* (2011), pp. 2937–2945.
- <sup>200</sup>T. Krawinkel and S. Schön, in *Proceeding of ION GNSS* (2015), pp. 2867–2874.
- <sup>201</sup>A. T. Gardner and J. A. Collins, in *Proceeding of Oceans* (2012), pp. 1–8.
- <sup>202</sup>M. Stanczyk *et al.*, in *Proceeding of Precise Time and Time Interval Systems and Applications Meeting* (2013), pp. 81–86.
- <sup>203</sup>See <https://phys.org/news/2012-03-darpa-chip-scale-atomic-clocks-aboard.html> for and [http://ssl.mit.edu/spheres/issdb/reports/SPHERES\\_ISS\\_TS031\\_Report.pdf](http://ssl.mit.edu/spheres/issdb/reports/SPHERES_ISS_TS031_Report.pdf) for information on chip-scale atomic clocks on board the International Space Station.
- <sup>204</sup>P. D. D. Schwindt *et al.*, *Appl. Phys. Lett.* **85**, 6409–6411 (2004).
- <sup>205</sup>P. D. D. Schwindt *et al.*, *Appl. Phys. Lett.* **90**, 081102 (2007).
- <sup>206</sup>V. Shah *et al.*, *Nat. Photonics* **1**, 649–652 (2007).
- <sup>207</sup>W. C. Griffith *et al.*, *Opt. Express* **18**, 27167–27172 (2010).
- <sup>208</sup>S. K. Lee and M. V. Romalis, *J. Appl. Phys.* **103**, 084904 (2008).
- <sup>209</sup>W. C. Griffith *et al.*, *Appl. Phys. Lett.* **94**, 023502 (2009).
- <sup>210</sup>R. Mhaskar *et al.*, *Appl. Phys. Lett.* **101**, 241105 (2012).
- <sup>211</sup>T. Scholtes *et al.*, *Phys. Rev. A* **84**, 043416 (2011).
- <sup>212</sup>E. Hodby *et al.*, *Appl. Phys. Lett.* **91**, 011109 (2007).
- <sup>213</sup>J. Belfi *et al.*, *J. Opt. Soc. Am. B* **24**, 1482–1489 (2007).
- <sup>214</sup>B. Patton *et al.*, *Appl. Phys. Lett.* **101**, 083502 (2012).
- <sup>215</sup>W. E. Bell and A. L. Bloom, *Phys. Rev. Lett.* **6**, 280–281 (1961).
- <sup>216</sup>R. Jimenez-Martinez *et al.*, *IEEE Trans. Instrum. Meas.* **59**, 372–378 (2010).
- <sup>217</sup>S. Knappe *et al.*, *Appl. Phys. Lett.* **97**, 133703 (2010).
- <sup>218</sup>J. Preusser *et al.*, in *Proceedings of IEEE International Frequency Control Symposiums and European Frequency and Time Forum* (2009), pp. 1180–1182.
- <sup>219</sup>J. Preusser *et al.*, in *Proceeding of IEEE Sensors Conference* (2008), pp. 344–346.
- <sup>220</sup>R. R. Mhaskar *et al.*, in *Proceeding of IEEE International Frequency Control Symposiums* (2010), pp. 376–379.
- <sup>221</sup>O. Alem *et al.*, *Opt. Express* **25**, 7849–7858 (2017).
- <sup>222</sup>O. Alem *et al.*, *Phys. Med. Biol.* **60**, 4797–4811 (2015).
- <sup>223</sup>Q. Gan *et al.*, in *International Conference on Electronic Packaging Technology* (2015), pp. 947–950.
- <sup>224</sup>M. P. Ledbetter *et al.*, *Proc. Natl. Acad. Sci. U. S. A.* **105**, 2286–2290 (2008).
- <sup>225</sup>A. J. Moule *et al.*, *Proc. Natl. Acad. Sci. U. S. A.* **100**, 9122–9127 (2003).
- <sup>226</sup>J. Granwehr *et al.*, *Phys. Rev. Lett.* **95**, 075503 (2005).
- <sup>227</sup>C. Hilty *et al.*, *Proc. Natl. Acad. Sci. U. S. A.* **102**, 14960–14963 (2005).
- <sup>228</sup>A. Abragam, *Principles of Nuclear Magnetism* (Oxford University Press, Oxford, 1961).
- <sup>229</sup>M. P. Ledbetter *et al.*, *J. Magn. Reson.* **199**, 25–29 (2009).
- <sup>230</sup>T. Theis *et al.*, *Nat. Phys.* **7**, 571–575 (2011).
- <sup>231</sup>R. Jiménez-Martínez *et al.*, *Nat. Commun.* **5**, 3908 (2014).
- <sup>232</sup>D. J. Kennedy *et al.*, *Sci. Rep.* **7**, 43994 (2017).
- <sup>233</sup>M. N. Livanov *et al.*, *Adv. Cardiol.* **28**, 78–80 (1981).
- <sup>234</sup>G. Bison *et al.*, *Opt. Express* **11**, 904–909 (2003).
- <sup>235</sup>G. Bison *et al.*, *Appl. Phys. B* **76**, 325–328 (2003).
- <sup>236</sup>G. Bison *et al.*, *J. Opt. Soc. Am. B* **22**, 77–87 (2005).
- <sup>237</sup>H. Xia *et al.*, *Appl. Phys. Lett.* **89**, 211104 (2006).
- <sup>238</sup>R. T. Wakai, in *Proceeding of XIII Mexican Symposium on Medical Physics* (2014), pp. 46–54.
- <sup>239</sup>E. Boto *et al.*, *Neuroimage* **149**, 404–414 (2017).
- <sup>240</sup>B. Lindseth *et al.*, in *Proceeding of Computers in Cardiology* (2007), pp. 443–446.
- <sup>241</sup>T. H. Sander *et al.*, *Biomed. Opt. Express* **3**, 981–990 (2012).
- <sup>242</sup>O. Alem *et al.*, *J. Neurosci.* **34**, 14324–14327 (2014).
- <sup>243</sup>H. Korth *et al.*, *Johns Hopkins APL Tech. Dig.* **28**, 248–249 (2010), see <http://www.jhuapl.edu/techdigest/TD/td2803/38KorthChip.pdf>.
- <sup>244</sup>H. Korth *et al.*, *J. Geophys. Res.: Space Phys.* **121**, 7870–7880, <https://doi.org/10.1002/2016JA022389> (2016).
- <sup>245</sup>M. S. Holston, M.Sc. thesis, Department of Chemical and Materials Physics, The University of California, Irvine, 2004.
- <sup>246</sup>R. M. Noor *et al.*, in *Proceeding of 2017 IEEE International Symposium on Inertial Sensors and Systems (INERTIAL)* (2017), pp. 156–159.
- <sup>247</sup>E. A. Donley *et al.*, *Phys. Rev. A* **79**, 013420 (2009).
- <sup>248</sup>M. Larsen and M. Bulatowicz, in *Proceeding of IEEE International Frequency Control Symposiums* (2012), pp. 597–601.
- <sup>249</sup>E. A. Donley *et al.*, *Rev. Sci. Instrum.* **78**, 083102 (2007).
- <sup>250</sup>A. J. Mager, *IEEE Trans. Magn.* **6**, 67–75 (1970).
- <sup>251</sup>S. M. Hendrickson *et al.*, *Phys. Rev. Lett.* **105**, 173602 (2010).
- <sup>252</sup>M. J. Renn *et al.*, *Phys. Rev. A* **53**, R648–R651 (1996).
- <sup>253</sup>A. D. Slepikov *et al.*, *Opt. Express* **16**, 18976–18983 (2008).
- <sup>254</sup>A. D. Slepikov *et al.*, *Phys. Rev. A* **81**, 053825 (2010).
- <sup>255</sup>P. Londero *et al.*, *Phys. Rev. Lett.* **103**, 043602 (2009).
- <sup>256</sup>A. Lurie *et al.*, *Opt. Lett.* **36**, 4776–4778 (2011).
- <sup>257</sup>C. Perrella *et al.*, *Phys. Rev. A* **85**, 012518 (2012).
- <sup>258</sup>A. M. Jones *et al.*, *Opt. Express* **19**, 2309–2316 (2011).
- <sup>259</sup>H. Schmidt and A. R. Hawkins, *Appl. Phys. Lett.* **86**, 032106 (2005).
- <sup>260</sup>G. Sague *et al.*, *Phys. Rev. Lett.* **99**, 163602 (2007).
- <sup>261</sup>E. Vetsch *et al.*, *Phys. Rev. Lett.* **104**, 203603 (2010).
- <sup>262</sup>S. P. Yu *et al.*, *Appl. Phys. Lett.* **104**, 111103 (2014).
- <sup>263</sup>A. Goban *et al.*, *Nat. Commun.* **5**, 3808 (2014).
- <sup>264</sup>T. Aoki *et al.*, *Nature* **443**, 671–674 (2006).
- <sup>265</sup>K. Knabe *et al.*, *Opt. Express* **17**, 16017–16026 (2009).
- <sup>266</sup>L. Stern and U. Levy, *Opt. Express* **20**, 28082 (2012).
- <sup>267</sup>L. Stern *et al.*, *Nat. Commun.* **5**, 4865 (2014).
- <sup>268</sup>A. Szapiro *et al.*, e-print [arXiv:1501.04218](https://arxiv.org/abs/1501.04218) (2015).
- <sup>269</sup>R. Ritter *et al.*, *Appl. Phys. Lett.* **107**, 041101 (2015).
- <sup>270</sup>R. Ritter *et al.*, *New J. Phys.* **18**, 103031 (2016).
- <sup>271</sup>A. Nitkowski *et al.*, *Opt. Express* **16**, 11930–11936 (2008).
- <sup>272</sup>W.-C. Lai *et al.*, *Opt. Lett.* **36**, 984–986 (2011).
- <sup>273</sup>L. Tombez *et al.*, *Optica* **4**, 1322–1325 (2017).
- <sup>274</sup>M. Hummon *et al.*, *Optica* **5**, 443–449 (2018).
- <sup>275</sup>M. L. Dakss *et al.*, *Appl. Phys. Lett.* **16**, 523 (1970).
- <sup>276</sup>A. Horsley *et al.*, *Phys. Rev. A* **88**, 063407 (2013).
- <sup>277</sup>A. Horsley *et al.*, *New J. Phys.* **17**(11), 112002 (2015).
- <sup>278</sup>S. A. Knappe *et al.*, *Opt. Express* **15**, 6293–6299 (2007).
- <sup>279</sup>C. Lee *et al.*, *Rev. Sci. Instrum.* **82**, 043107 (2011).
- <sup>280</sup>S. Pustelny *et al.*, private communication (2016).
- <sup>281</sup>F. Gruet *et al.*, *Opt. Laser Eng.* **51**, 1023–1027 (2013).
- <sup>282</sup>L. Weller *et al.*, *Opt. Lett.* **37**, 3405–3407 (2012).
- <sup>283</sup>V. Shah *et al.*, in *Proceeding of Precise Time and Time Interval (PTTI) Meeting* (2011), pp. 221–230.
- <sup>284</sup>D. R. Scherer *et al.*, in *Proceeding of 46th Annual Precise Time and Time Interval Systems and Applications Meeting* (2014), pp. 154–163.
- <sup>285</sup>V. Shah *et al.*, in *Proceeding of IEEE International Frequency Control Symposiums* (2012), pp. 700–705.
- <sup>286</sup>K. Nelson *et al.*, in *Proceeding of IEEE/ION Position Location and Navigation Symposium* (2012), pp. 1094–1098.
- <sup>287</sup>K. Salit *et al.*, in *Proceedings of IEEE International Frequency Control Symposiums* (2012), pp. 706–709.
- <sup>288</sup>J. Sebby-Strabley *et al.*, in *Proceeding of Precise Time and Time Interval (PTTI) Meeting* (2011), pp. 231–238.
- <sup>289</sup>T. Muller *et al.*, *Phys. Rev. A* **76**, 063611 (2007).
- <sup>290</sup>T. Müller *et al.*, *Eur. Phys. J. D* **53**, 273–281 (2009).
- <sup>291</sup>F. Sorrentino *et al.*, *Microgravity Sci. Technol.* **22**, 551–561 (2010).
- <sup>292</sup>G. W. Hoth *et al.*, *Opt. Lett.* **38**, 661–663 (2013).
- <sup>293</sup>X. Liu *et al.*, *Phys. Rev. Appl.* **8**, 054001 (2017).
- <sup>294</sup>M. Trupke *et al.*, *Appl. Phys. Lett.* **88**, 071116 (2006).
- <sup>295</sup>G. N. Lewis *et al.*, *J. Micro Electro Mech. Syst.* **18**, 347–353 (2009).
- <sup>296</sup>S. Pollock *et al.*, *Opt. Express* **17**, 14109–14114 (2009).
- <sup>297</sup>S. Pollock *et al.*, *New J. Phys.* **13**, 043029 (2011).
- <sup>298</sup>Q. Bodart *et al.*, *Appl. Phys. Lett.* **96**, 134101 (2010).
- <sup>299</sup>C. C. Nshii *et al.*, *Nat. Nanotechnol.* **8**, 321–324 (2013).
- <sup>300</sup>J. P. McGilligan *et al.*, *Opt. Express* **23**, 8948–8959 (2015).
- <sup>301</sup>J. P. McGilligan *et al.*, *Sci. Rep.* **7**, 384 (2017).
- <sup>302</sup>J. Reichel, *Appl. Phys. B* **74**, 469–487 (2002).
- <sup>303</sup>E. A. Salim *et al.*, *Quantum Inf. Process.* **10**, 975–994 (2011).
- <sup>304</sup>D. M. Farkas *et al.*, *Appl. Phys. B* **101**, 705–721 (2010).
- <sup>305</sup>P. Rosenbusch, *Appl. Phys. B* **95**, 227–235 (2009).
- <sup>306</sup>F. Ramírez-Martínez *et al.*, *Adv. Space Res.* **47**, 247–252 (2011).
- <sup>307</sup>J. A. Rushton *et al.*, *Rev. Sci. Instrum.* **85**, 121501 (2014).
- <sup>308</sup>J. Kitching *et al.*, *J. Phys.: Conf. Ser.* **723**, 012056 (2016).